Interactions between Metal-Organic Frameworks and Chemical Warfare Agents

by

Jonathan P. Ruffley

B.S. Chemical Engineering, The Ohio State University, 2015

Submitted to the Graduate Faculty of the

Swanson School of Engineering in partial fulfillment

of the requirements for the degree of

Doctor of Philosophy

University of Pittsburgh

2021

UNIVERSITY OF PITTSBURGH

SWANSON SCHOOL OF ENGINEERING

This dissertation was presented

by

Jonathan P. Ruffley

It was defended on

December 11, 2020

and approved by

Giannis Mpourmpakis, PhD, Associate Professor, Department of Chemical and Petroleum Engineering

Nathaniel L. Rosi, PhD, Professor, Department of Chemistry

Christopher E. Wilmer, PhD, Associate Professor, Department of Chemical and Petroleum Engineering

Dissertation Director: J. Karl Johnson, PhD, Professor, Department of Chemical and Petroleum Engineering

Interactions between Metal-Organic Frameworks and Chemical Warfare Agents

Jonathan P. Ruffley, PhD

University of Pittsburgh, 2021

Continued use of chemical warfare agents has motivated interest in new materials providing enhanced capture, detection, and destruction of such agents. Metal-organic frameworks (MOFs), and specifically the UiO family of MOFs have been extensively studied for adsorption and degradation of chemical warfare agents (CWAs) and their simulants. We have used density functional theory (DFT) to design functionalized MOFs having a range of binding energies for the nerve agent simulant dimethyl methylphosphonate, the blister agent HD and its simulant molecule 2-chloroethyl ethylsulfide, and the nerve agents GB, VX, and A-234. We find that the order of predicted binding energies of DMMP from simulations agrees with data from temperature programmed desorption experiments. Moreover, the values of the binding energies are also in good agreement. This serves as a proof-of-concept that ab initio calculations can guide experiments in designing MOFs that exhibit higher affinity for CWAs and their simulants. We then use these MOFs in additional calculations to determine the capability of 2-CEES at predicting the binding interactions of HD and evaluate their performance in binding the nerve agents. We find that 2-CEES provides reasonable qualitative predictions of HD behavior, and the nerve agents bound with varying degrees of strength. We identify a series of MOFs: UiO-67-NH_2, UiO-67-OH, and UiO-67 that exhibit a strong gradient in binding strength for A-234.

Table of Contents

List of Tables

List of Figures

Preface

Computations were performed at the University of Pittsburgh's Center for Research Computing, the Pittsburgh Supercomputer Center through a grant from the Extreme Science and Engineering Discovery Environment (XSEDE), which is supported by National Science Foundation grant number ACI-1548562, under allocation No. TG-DMR110091, and the U.S. Army Engineer Research and Development Center DoD Supercomputer Resource Center. This project received support from the Defense Threat Reduction Agency (DTRA) (Grant no. HDTRA1-16-1-0044).

Experimental work discussed in Chapter 1 was completed by the research groups of Prof. Nathaniel L. Rosi at the University of Pittsburgh and Prof. Eric Borguet at Temple University. Please see 10.1021/acs.jpcc.9b05574 for details on their contributions to the work described in Chapter 1.

Experimental work discussed in Chapter 2 was completed by the research groups of Prof. Nathaniel L. Rosi at the University of Pittsburgh and Prof. Eric Borguet at Temple University. Please see 10.1021/acs.jpcc.0c07040 for details on their contributions to the work described in Chapter 2.

1.0 Design, Synthesis, and Characterization of Metal-Organic Frameworks for Enhanced Sorption of Chemical Warfare Agent Simulants [1]

1.1 Introduction

Chemical warfare agents (CWAs) are a persistent and evolving threat. Therefore, continued development of mitigation and defense technologies is necessary. Currently, a combination of high-efficiency particulate air (HEPA) media and activated carbon impregnated with materials capable of reacting with volatile species is used in respirators to protect against exposure to CWAs.[2-4] While highly effective in capturing a variety of deadly species, microporous carbon-based materials suffer from limited selectivity to CWAs due to their ill-defined pore sizes, shapes, and pore chemistry.[5] In addition, the lack of catalytic activity in purely carbonaceous sorbents (e.g., activated carbon) results in the potential re-emission of CWAs.[6-7]

Key features of an ideal reactive sorbent material for CWA removal include high capacity and selectivity towards CWAs, the ability to convert CWAs into benign products, stability under a variety of conditions for a long period of time, and the ability to regenerate the sorbent and catalyst. To this end, metal-organic frameworks (MOFs) have many advantages. Compared to porous carbons, many MOFs have not only larger surface areas for high adsorption capacity, but also well-defined pores required for high selectivity.[8-9] Further, MOF pore dimensions and chemistry can be systematically modified by adjusting the size and functional groups of organic linkers, which can significantly affect MOF-adsorbate interactions and potentially lead to enhanced selectivity for specific adsorbates.[10-11]

A variety of MOFs have been examined for CWA simulant adsorption and destruction.[12-17] Computational and experimental methods demonstrate that MOFs degrade CWAs and less hazardous CWA simulant molecules in acidic/basic/neutral solutions,[12-13,18-21] under ambient conditions,[22-23] catalytically,[12-13, 18-21, 23-25] non-catalytically,[22] when impregnated into other materials such as textiles,[21, 25-26] and when doped or impregnated with other materials, such as Lewis bases.[20, 24]

In this work we focus on the UiO family of MOFs.[27] These MOFs consist of $Zr_6O_4(OH)_4(COO)_{12}$ secondary building units (SBUs) interconnected by linear dicarboxylate ligands and are known for their exceptional thermal, mechanical, and chemical stability.[27-29] By introducing functional groups to the ligands pre-synthesis, a variety of variations of these MOFs have been synthesized while maintaining excellent stability properties.[30-33]

Recently, Wang et al. reported that dimethyl methylphosphonate (DMMP), an adsorption simulant for sarin, can be adsorbed by non-functionalized Zr-based MOFs via both reversible physisorption and irreversible chemisorption.[22] However, there have been relatively few studies of the interactions of CWAs or CWA simulants with functionalized MOFs.[34] Our hypothesis is that different functional groups incorporated into MOF linkers can be used to tune the adsorption strength of CWAs. At the outset, it is not obvious that CWA or simulant adsorption strengths can be controlled through modifying the linker with different functional groups because these molecules typically interact strongly with the SBU rather than the linker.[22, 35] However, the strong guest-SBU interactions are typically due to the presence of defects, such as missing linkers;[22, 35-36] we assume that in relatively defect-free MOFs the sorbent-sorbate interactions can be tuned by introducing functional groups on the linker.

This work examines the adsorption of DMMP in functionalized UiO-67 with the goal of identifying functional groups that impart enhanced MOF-DMMP binding. We use a variety of computational methods to probe three functionalized UiO-67 MOFs and compare results with our experimental colleagues, determining the nature of their interactions with DMMP. The studies and conclusions presented herein will inform our design of stratified MOFs[37] containing specific domains that selectively concentrate CWAs and others that reject undesired background molecules and/or enhance the removal of CWA degradation products.

1.2 Experimental and Theoretical Methodology

1.2.1 Functional Group Identification

We selected UiO-67 as the platform MOF for our studies because its pore windows are sufficiently large to permit facile diffusion of CWAs and their simulants.[22] We note, however, that stability of the UiO MOFs generally decreases with increasing ligand size;[28, 38] UiO-67 is an appropriate selection to balance stability and pore size concerns. It has been shown that UiO-67 is not stable in the presence of water vapor;[39] however, the synthesis procedure used[40] is different than that used here, and reactivity with water may depend on the synthesis used, assuming the reactivity is defect driven.

We confined our search for functional groups to a subset of those that have already been incorporated within UiO-6x MOFs.[30, 41-43] Specifically, we considered the ligands shown in Figure 1, derivatized from 1,1'-biphenyl-4,4'-dicarboxylate (BPDC) with different substituents at the 2-

position, including -H, -CH_3, -SH, -NH_2, -N_3, -NO_2, -Br, and -Cl. We denote the corresponding UiO-67 analogue MOFs as UiO-67-X, where X represents the functional moiety.

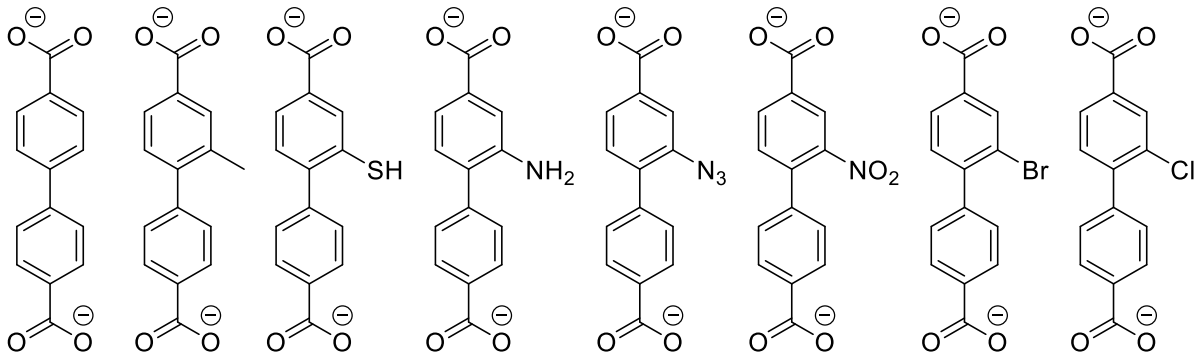

Figure 1. Ligands computationally screened to create a UiO-67 family MOF (from left to right: BPDC, CH3-BPDC, SH-BPDC, NH2-BPDC, N3-BPDC, NO2-BPDC, Br-BPDC, Cl-BPDC).

As an initial screening of the binding of DMMP with the functionalized MOFs, benzene was used to represent the BPDC linker. Binding energies of DMMP with functionalized benzene was considered as a surrogate for the binding energies of DMMP in the UiO-67-X MOFs. The ABCluster[44-45] program was used to generate 20 random configurations of DMMP around the functionalized benzene rings in order to identify the ground state binding configurations. These configurations were then optimized using density functional theory (DFT) as implemented in Orca.[46] Convergence criteria are reported in Appendix Table A1 of Appendix A. The Perdew-Burke-Ernzerhof (PBE) functional[47] was used with the Def2-TZVP basis set[48-49] and the D3BJ dispersion correction.[50-51] The resulting energies were checked for basis set superposition error via

the Boys-Bernardi counterpoise correction[52] as implemented in Gaussian 09,[53] shown in Appendix Figure A2.

The level of theory was verified to give appropriate results for the systems of interest by comparing the DFT results with delocalized pair natural orbital coupled-cluster singles doubles perturbational triples (DLPNO-CCSD(T))[54] calculations, shown in Appendix Figure A1. A single DMMP molecule as well as each of the functionalized benzene molecules were relaxed following this same procedure. The resulting energies were then used to calculate binding energies via eq (1-1).

$$\Delta E_{\text{bind}} = E_{AB} - E_A - E_B \tag{1-1}$$

Note that ΔE_{bind} is negative if binding is favorable. The functionalized linkers were incorporated into perfect UiO-67 primitive cells. The atom positions, using lattice parameters of relaxed UiO-67 ($a = b = c$ = 19.1 Å, $\alpha = \beta = \gamma = 60°$) were then relaxed using DFT as implemented in CP2K.[55-57] The lattice parameters of each MOF were not relaxed because it has been shown that there is minimal difference between the parameters of functionalized ligand MOFs.[58] The PBE functional[47] was used in conjunction with the Goedecker-Teter-Hutter pseudopotentials[59] and the DZVP-MOLOPT-SR basis set,[60] and Grimme's dispersion correction[50] was applied. The cutoff and relative cutoff were 400 Ry and 50 Ry, respectively. Convergence information is included in Appendix Figure A2 and Appendix Figure A3. The DIIS orbital transformation minimizer[57] and LBFGS optimizer[61] were used. These settings were used for all other CP2K calculations in this work. A single gas phase DMMP molecule was also relaxed using this procedure to compute binding energies.

The ground state of a single DMMP molecule in the various UiO-67-X MOFs was estimated using the following procedure: A single DMMP molecule was randomly placed into the octahedral pore of each primitive cell. Ab initio molecular dynamics (AIMD) simulations in the canonical ensemble were carried out on the periodic system at a temperature of 1000 K using the GLE thermostat.[62-63] The AIMD simulations were run for 7.5 ps, using a timestep of 0.5 fs. The coordinates of the AIMD simulations were saved every 100 timesteps and the sampled geometries were relaxed in CP2K to their local minima. The lowest energy structure identified was used in eq (1-1) to compute the binding energy for each functionalized MOF. Strongest binding energy structures for each MOF were then retested by substituting functional groups for all other MOFs into these structures as additional configurations to test.

1.2.2 DMMP Force Field

Existing classical force fields for DMMP have been reported in the literature.[64-65] However, we chose to develop a fully flexible force field with intramolecular potential parameters for DMMP generated by the QuickFF formalism.[66] Our force field is based on model 2 from Vishnyakov and Neimark,[65] with corrected charges. Details of the procedure are given in Appendix A. We chose this approach to facilitate rapid generation of force fields for other simulants and CWAs to be used in molecular dynamics simulations.

A Lennard-Jones and Coulomb model was used for non-bonded interactions. Electrostatic parameters were corrected to achieve charge neutrality while producing a physically reasonable dipole moment for DMMP[67] Lennard-Jones parameters were adjusted to reproduce the liquid density of DMMP at 298 K and 1 atm. Ewald summation[68] was used to calculate electrostatic interactions. Lorentz-Berthelot combining rules were used for unlike interactions. Intramolecular

interactions involving atoms separated by less than four bonds were excluded. Molecular dynamics simulations were performed using LAMMPS[69] in the isothermal-isobaric ensemble.[70] These results were compared to isothermal-isobaric Monte Carlo simulations performed in RASPA[71] in order to validate the potential. Initial configurations for LAMMPS simulations were created with Packmol.[72] Additional details of these simulations are reported in Appendix Table A3 and Appendix Table A4. DMMP force field parameters are given in Appendix Table A5 through Appendix Table A8.

1.2.3 Simulated Isotherms

Simulated surface areas were calculated for each MOF using a Lennard-Jones 12-6 argon model[73] following an accessible surface area procedure.[74] Brunauer-Emmett-Teller (BET)[75] surface areas were calculated from nitrogen isotherms measured at 77 K.[1] Excess adsorption isotherms of nitrogen at 77 K using a potential taken from the literature[76] and absolute adsorption isotherms of DMMP at 298 K were simulated in the three UiO-67-X MOFs from GCMC simulations using the RASPA[71] software package. Density Derived Electrostatic and Chemical (DDEC) charges for the atoms in each MOF were computed using the DDEC6[77-80] formalism based on DFT derived electron density calculations. Ewald summation[68] was used to calculate all electrostatic interactions. The Lennard-Jones parameters for the MOF atoms were taken from DREIDING,[81] except zirconium, which was sourced from UFF,[82] as has been done previously.[83] The potential was truncated at a cutoff of 14.0 Å and standard tail corrections were applied.[84] Lorentz-Berthelot combining rules were used for unlike interactions. Helium void fractions were calculated for each MOF (Appendix Table A9), and the ideal gas Rosenbluth weight of DMMP

was calculated to be 0.00556.[71] A supercell containing eight primitive cells with fixed MOF atoms was used for all GCMC simulations. One cycle was defined as *N* steps, where *N* was the number of adsorbates in the system at the beginning of the cycle. Each state was run for 5×10^4 equilibration cycles and 2×10^5 production cycles.

1.3 Results and Discussion

1.3.1 Functional Group Selection

Binding energies for DMMP on periodic crystal models of UiO-67-X for X = H (unfunctionalized), CH_3, SH, NH_2, N_3, NO_2, Br, and Cl are shown in Figure 2a. The strongest binding energy for each pair is plotted. A parity plot of binding energies computed from crystal and cluster models in given in Appendix Figure A4; trends in binding energies do not agree for the crystal and cluster calculations. The order from weakest to strongest binding for the crystal model is H < SH < Cl ~ NO_2 < N_3 < CH_3 < Br < NH_2. The cluster binding energies are ordered from weakest to strongest as H < Cl < Br < N_3 < CH_3 < NO_2 < SH < NH_2. Both models agree that H is the weakest, NH_2 is the strongest and CH_3 is intermediate. We therefore chose these three systems for experimental study. UiO-67-CH_3 has not been previously reported in the literature, although UiO-66-CH_3 has been synthesized.[32] The geometries of the most favorable binding configurations for these three systems are also shown in Figure 2.

Examination of the energy local minima of DMMP and the crystal MOF model reveals that DMMP interacts with the confluence of linkers around the SBU of the MOF in each case (Figure 2 and Appendix Figure A5 through Appendix Figure A12). This demonstrates that while

functionalization of the ligand indeed appears to impact the binding energy of the MOF, the cluster model is not appropriate for making binding strength predictions; even if it produced substantially better agreement with the crystal model than that observed here, it is not an accurate physical representation of the interaction of interest; that of DMMP in an environment with several linkers. It is important to note that the DMMP does not interact directly with the SBU in the absence of missing linker defects, as can be seen from the closest pairwise interactions between DMMP and the framework coming from O atoms on DMMP interacting with H atoms on the linkers (Figure 2). It is also instructive to note that DMMP does not directly interact with the CH_3 functional group in UiO-67-CH_3, as can be seen from Figure 2c. We surmise that the CH_3 group provides steric and van der Waals interactions that increase the binding energy of DMMP relative to some other functional groups. The energy trend compares quite favorably with the desorption energies determined via temperature programmed desorption (TPD, done by experimental colleagues), with DFT predicting weaker binding than the experiments by around 10 kJ/mol.

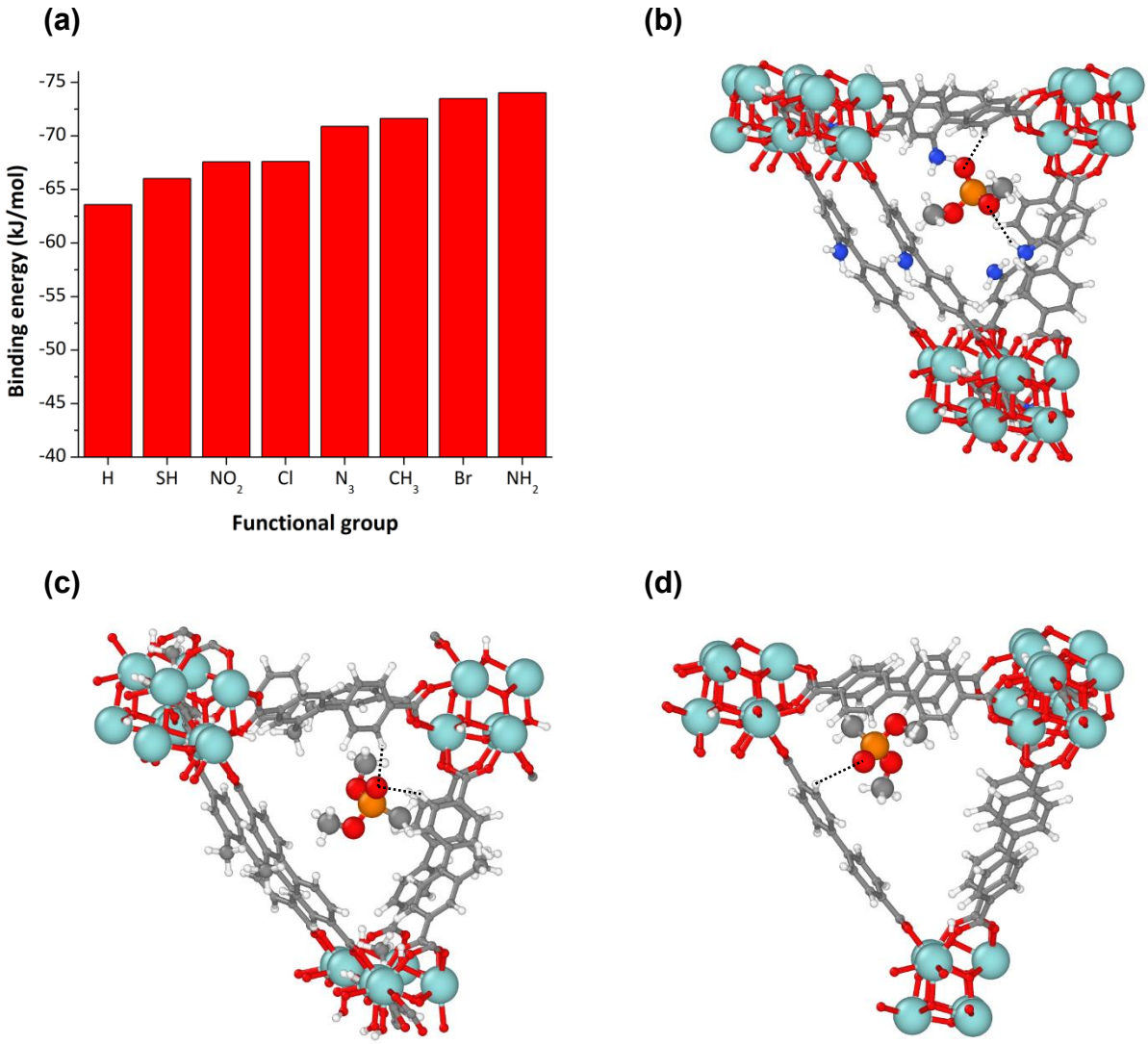

Figure 2. (a) Crystal binding energies computed from CP2K DFT calculations. (b) Optimal binding geometry of DMMP with UiO-67-NH_2. Dashed lines indicate hydrogen bonds of 2.34 Å (top) and 2.45 Å (bottom). (c) Optimal binding geometry of DMMP with UiO-67-CH_3. Dashed lines indicate hydrogen bonds of 2.28 Å (vertical) and 2.40 Å (horizontal). (d) Optimal binding geometry of DMMP with UiO-67. Dashed line indicates hydrogen bond of 2.76 Å. For panels (b), (c), and (d), Zr shown in light blue, oxygen shown in red, carbon shown in gray, nitrogen shown in blue, hydrogen shown in white. Visualizations created with OVITO.[85]

Table 1. Kinetic parameters extracted from desorption profiles following 1000 L DMMP on UiO-67-X, along with DFT predictions of the negative of the binding energies.

MOF	$^{*}T_{des}$ (K)	E_{des} (kJ/mol)	E_{DFT} (kJ/mol)
UiO-67-NH_2	334	87 ± 2.0	74
UiO-67-CH_3	307	81 ± 0.5	71
UiO-67	260	76 ± 2.0	64

$^{*}T_{des}$ shown for single TPD spectra at 1000 L DMMP exposure with a heating rate of 2.2 K/s.

1.3.2 Simulated DMMP Adsorption Isotherms

We simulated adsorption isotherms of DMMP in the three MOFs at 298 K using the GCMC method. Our simulated isotherms are shown in Figure 3. At low pressures, the amount adsorbed follows the binding energy trends predicted by DFT calculations. This is reasonable because the adsorbate-adsorbent interactions are expected to be dominated by the most attractive binding sites at low coverage. At higher loading, surface area is the dominating factor in adsorption, following the trend predicted by BET analysis and surface area calculations (Appendix Figure A13 and Appendix Figure A14 respectively). A logistic 3P function was fit to each isotherm, and statistical analysis was conducted. The results of this analysis, tabulated in Appendix Table A10 and Appendix Table A14, indicate that the differences in isotherms for the MOFs are statistically significant.

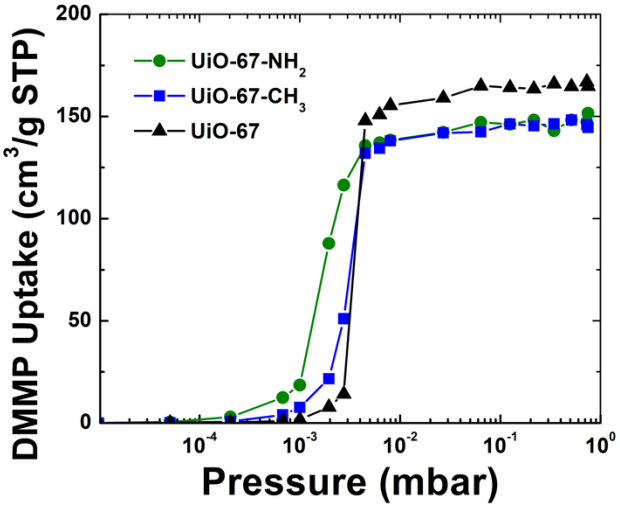

Figure 3. Absolute adsorption isotherms computed from GCMC simulations for DMMP at 298 K in UiO-67-NH_2, UiO-67-CH_3, and UiO-67.

1.4 Conclusions

Density functional theory has been used to predict ligand functionalizations that yield differential uptake of DMMP in a UiO-67 family MOFs. Three functionalized MOFs were synthesized based on DFT predictions of differential binding energies. TPD experiments showed that the functionalized MOFs indeed exhibit the same order of adsorption affinities for DMMP predicted from DFT calculations and classical GCMC simulations. These results demonstrate that functionalized MOF domains with differential affinity for CWAs can be fabricated, providing a foundation on which stratified MOFs for CWA capture may be based. Our calculations and experiments predict that a stratified MOF consisting of UiO-67-NH_2⊂UiO-67-CH_3⊂UiO-67 will show an equilibrium concentration gradient of DMMP induced by the differential binding of DMMP.

2.0 Modeling of Diffusion of Acetone in UiO-66 (accepted)

2.1 A Note on Chapter 2

All diffusion calculations described in this chapter were conducted by undergraduate students under my joint supervision with Prof. J. Karl Johnson. These calculations used scripts I developed to allow for direct insertion of molecules into MOF pores, run simulations, and collect and process data. I also wrote the backbone script used in running the molecular dynamics simulations. Additional intellectual contributions include measurement of distances between ligands of pore windows during molecule transits to assess the importance of framework flexibility on diffusion.

2.2 Introduction

Metal-organic frameworks (MOFs) are porous materials comprised of metal oxyhydroxide secondary building units (SBUs) connected by organic ligands (linkers). MOFs have applications in a variety of fields,[86-87] with substantial efforts focused on the use of MOFs for gas separations[88-91] and adsorption.[1, 92-95] MOFs have also been used for chemical warfare agent (CWA) capture and degradation. Specifically, UiO-66 and its derivatives have been widely studied for this purpose.[1, 96-100] Effective use of these materials requires an understanding of mass transport limitations because agents must rapidly adsorb and diffuse into the interior of the MOF, where they are

temporarily captured (through physisorption) and can react at active sites (through chemisorption at open metal sites) within the MOF.

UiO-66 has a formula unit containing one SBU constructed of 6 Zr atoms with 4 μ_3-O atoms and 4 μ_3-OH groups, coordinated by 12 benzene dicarboxylate (BDC) moieties [$Zr_6(\mu_3\text{-}O)_4(\mu_3\text{-}OH)_4](C_8H_4O_4)_6$]. The μ_3-OH groups may form hydrogen bonds with some CWAs and CWA simulants, which could significantly impact adsorption and diffusion. We note that it has been reported that UiO-66 may be reversibly dehydroxylated by heating to high temperature in vacuum,[29, 101] which eliminates the μ_3-OH groups. We do not consider the dehydroxylated form in this work because under practical conditions UiO-66 would be in its hydroxylated state. The SBUs of UiO-66 are 12 coordinated by BDC linkers, with each linker shared between two SBUs, making all the Zr atoms in the SBU fully coordinated in pristine UiO-66. CWAs are typically too large to diffuse at appreciable rates in pristine UiO-66.[102] In practice it is defective UiO-66 that is of interest. However, we first seek to understand baseline interactions, adsorption, and diffusion in pristine UiO-66.

Ramsahye and Maurin provide an excellent overview of the calculation of diffusion in MOFs from molecular simulation.[103] Simulation based methods have been used to study diffusion in MOFs, almost exclusively through the use of classical molecular dynamics.[104-116] However, there is at least one study using density functional theory calculations,[117] but time scales for these simulations are three orders of magnitude smaller (10s of ps rather than 10s of ns) than classical potential simulations.

Diffusivities of a variety of molecules in MOFs are reported in the literature, including: hydrogen,[106-108, 115, 117-119] noble gasses,[105, 115, 120] CO_2,[110, 113, 115] N_2,[110, 115] alkanes,[107, 110-111, 113-115] acetylene,[109] terephthalic acid,[112] benzene,[116] and mixtures.[107-108, 110, 121-122]

An important consideration in simulation studies of diffusion in MOFs is whether to model the framework as rigid or flexible. Many previous simulation studies of diffusion approximated the MOFs framework as being rigid.[104-115] The use of rigid frameworks makes the simulations more computationally efficient and greatly simplifies the construction of the potentials used for simulating the MOFs. Simulations of diffusion using flexible frameworks have also been performed.[105, 113, 116-117] Simulations report self-diffusivities,[105-117, 120] as well as corrected and transport diffusivities.[113, 115, 120] We note that these three types of diffusivities are equivalent in the limit of low loading.[123] In this work we report self-diffusion, as calculated from the Einstein relation given by

$$D_S = \frac{1}{2td}\langle \sum |r_i(t) - r_i(0)|^2 \rangle \qquad \textbf{(2-1)}$$

Where t is the time, d is the dimensionality of the system, the sum is over all atoms of diffusing molecules in the system, and the angle brackets denote an ensemble average.

The transport diffusion of benzene, toluene and xylene through UiO-66 via isothermal diffusion experiments has been studied with in situ infrared (IR) spectroscopy. The pore window was found to limit diffusion, and diffusion rates decreased with increasing molecular size.[124] Diffusion coefficients were on the order of 10^{-10} m^2/s to 10^{-16} m^2/s and although the guest molecules are nonpolar, IR spectroscopy indicated hydrogen bonding interactions with the framework μ_3-OH groups. Sharp et al. considered the transport of n-butane using in situ IR in UiO-66 and reported diffusion coefficients on the order of 10^{-10} $cm^2\ s^{-1}$.[125]

In this work we seek to elucidate the impact of framework flexibility and hydrogen bonding on adsorption and diffusion of polar molecules in UiO-66. As a first step, we have chosen to study adsorption and diffusion of acetone in pristine UiO-66, reasoning that one should first understand the pristine material before including the impact of missing linker defects, since these defects are difficult to fully characterize. We chose acetone for this study because it is small enough to be expected to diffuse rapidly through the small windows of UiO-66 and also because it is a strongly polar hydrogen bond acceptor but does not self-hydrogen bond. Thus, any hydrogen bonding observed experimentally must be due to acetone-μ_3-OH interactions. We present a combined experimental and theoretical approach to investigate acetone-UiO-66 interactions. We have synthesized and characterized low-defect UiO-66 samples. We have measured μ_3-OH hydrogen bonding in UiO-66 dosed with acetone with FT-IR under ultra-high vacuum (UHV) conditions as a function of temperature. We have used molecular simulations to study adsorption and diffusion of acetone in pristine UiO-66.

2.3 Computational Methods

Molecular dynamics calculations were carried out with Large-scale Atomic/Molecular Massively Parallel Simulator (LAMMPS).[69] Simulations were conducted at zero loading up to and somewhat beyond saturation. Zero loading simulations were conducted by turning off interactions between the acetone molecules, thus rigorously excluding any adsorbate-adsorbate interactions. This allowed for simulation of the low loading limit, while obtaining better statistics than simulations having a single molecule in the simulation cell.

A UiO-66 supercell was created that contained 32 formula units (primitive cells). One formula unit contains two tetrahedral pores and one octahedral pore. We used two different flexible force fields for UiO-66, the UFF force field parameters described by Boyd et al.[126] and the Rogge et al. potential.[127] We used atom centered charges computed from analysis of our density DFT electron density calculations with the DDEC6 and Chargemol programs[77, 79-80, 128] calculations for both of these potentials. The TraPPE model was used for acetone.[129] A Lennard-Jones model was used for neon.[130] LAMMPS input files containing all the necessary parameters are provided in the Supporting Information. Periodic boundary conditions were applied, and the cutoff was 12.5 Å. A timestep of 0.5 fs was used for all simulations. Each run was equilibrated for 50 ps in the canonical (*NVT*) ensemble using the Nosé-Hoover thermostat.[131-132] Data were collected over 25 ns in the microcanonical (*NVE*) ensemble to avoid artifacts due to the thermostat on the dynamics of the system. Multiple time origins and multiple independent simulations (from 10 to 50) were used to improve statistics.

Acetone in flexible UiO-66 was studied at three temperatures: 325 K, 350 K, and 425 K. Each simulation involved 100 non-interacting (i.e., zero loading) acetone molecules inserted into the MOF. Additional simulations were conducted at finite loading using 32, 64, 128, 160, and 224 acetone molecules per simulation cell to model the effect of loading up to saturation. These simulations correspond to 1, 2, 3, 5, and 7 molecules per formula unit, respectively. Saturation loading at 298 K was determined to be about 6 molecules per formula unit from an adsorption isotherm of acetone using a methodology we have reported previously.[90, 133] Hence, a loading of 7 molecules per formula unit corresponds to an external pressure of acetone beyond the saturation pressure. Acetone in rigid UiO-66 was simulated at 325 K. 100 molecules were inserted, and 50 independent runs were used at zero loading.

Simulations of neon in flexible and rigid UiO-66 were conducted at 325 K and contained 500 non-interacting (zero loading) neon atoms. 50 runs were taken for both rigid and flexible models. The mean-squared displacement (MSD) for all molecular dynamics runs was calculated every 100 timesteps for each run using the center-of-mass formalism. Runs were block averaged using 5 blocks. The data was processed as 250 evenly spaced multiple time origins, and diffusion coefficients were calculated using the Einstein relation, eq (2-1).

2.4 Prediction of Binding Energies from Density Functional Theory

The primitive cell of pristine UiO-66 has three distinct pores: a tetrahedral pore containing 4 μ_3-OH groups, a tetrahedral pore containing 4 μ_3-O groups, and the octahedral pore. The lowest energy configurations of an acetone molecule in the three different pores of pristine UiO-66 was estimated from density functional theory (DFT) as implemented within CP2K 5.1.[55-57] Minimum energy structures were identified using a modified basin hopping technique described in our previous paper.[1] The PBE functional[47] Goedecker-Teter-Hutter pseudopotentials[59] were used with the DZVP-MOLOPT-SR basis set,[60] and Grimme's D3 dispersion correction[50] was applied. The cutoff and relative cutoff values were 400 Ry and 50 Ry, respectively. Convergence of these parameters has been verified previously[1] for UiO-67, which is expected to be transferable to UiO-66. The conjugate gradient orbital transformation minimizer[134] and LBFGS optimizer[61] were used. Relaxation calculations were performed on the periodic UiO-66 primitive cell ($a = b = c = 14.83$ Å, $\alpha = \beta = \gamma = 60°$). The energy of acetone was calculated by relaxing an isolated molecule of acetone in a cubic box 19 Å on a side. All three pristine pore environments were studied

independently. A single acetone molecule was placed into each of the three pores: the μ_3-OH tetrahedral pore, the μ_3-O containing pore, and the octahedral pore.

Ab initio molecular dynamics (AIMD) simulations in the canonical ensemble were carried out on each of the three periodic systems at a temperature of 1000 K using the GLE thermostat.[62-63] The AIMD simulations were run for 5 ps, using a time step of 0.5 fs. The coordinates of the AIMD simulations were saved every 100 timesteps and the sampled geometries were relaxed to their local minima. The resulting energies were then used to calculate binding energies defined as

$$\Delta E_{\text{bind}} = E_{\text{MOF}/A} - E_{\text{MOF}} - E_A \quad \textbf{(2-2)}$$

where $E_{\text{MOF}/A}$ is the energy of the MOF + acetone system, and E_{MOF}, E_A are energies of the empty MOF and acetone in the gas phase, respectively.

2.5 Results and Discussion

Plots of the MSD divided by time (MSD/t) as a function of time for acetone in flexible and rigid UiO-66 using the Boyd et al. potential[126] are shown in Figure 4. Fickian diffusion, described by eq (2-1), will result in MSD/t being a constant at long times, and this is what is seen for the flexible UiO-66 potential in Figure 4a. In contrast, MSD/t for the rigid model continually and dramatically decreases with time (note the log scale in Figure 4b), indicating that acetone does not diffuse in the rigid model over the time scales of the simulation. We have computed diffusion coefficients for acetone at zero loading as a function of temperature in UiO-66 using three flexible MOF potentials: the Boyd et al. potential,[126] the Rogge et al. potential,[127] and our modification to the

Rogge et al. potential, referred to as TraPPE/Rogge et al., which we describe below. The diffusion coefficients are reported in Table 2 and plotted in Figure 5. The data were fit to an Arrhenius equation of the form $D = D_0 \exp(-E_A/RT)$ to calculate the activation energies of diffusion for these potentials, which are E_A = 15.8, 16.5, and 27.2 kJ/mol for the Boyd et al., Rogge et al., and TraPPE/Rogge et al. potentials, respectively.

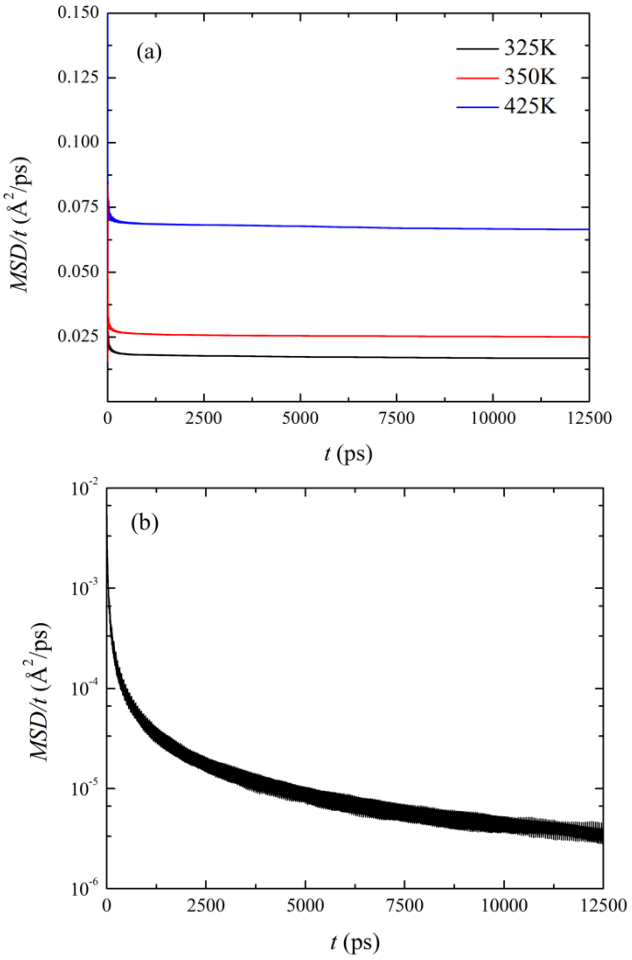

Figure 4. Mean-squared displacement divided by time of acetone in UiO-66 using the (a) flexible or (b) rigid framework model of Boyd et al.[126] at 325 K. Note the semi-log scale in (b), required to show exponential decrease in MSD/*t* with time.

Table 2. Diffusion constants of acetone at zero loading in a) Boyd et al. flexible UiO-66;[126] b) Rogge et al flexible UiO-66;[127] c) TraPPE modified Rogge et al. UiO-66. Uncertainties in the least significant digits, given by two standard deviations of the mean, are given in parentheses, e.g., 2.80(30) × 10^{-11} means 2.8 × 10^{-11} ± 3.0 × 10^{-12}, and 4.88(150) × 10^{-12} means 4.88 × 10^{-12} ± 1.5 × 10^{-12}.

T (K)	a) D_s (m^2/s)	b) D_s (m^2/s)	c) D_s (m^2/s)
325	2.80(30) × 10^{-11}	4.02(48) × 10^{-11}	4.88(150) × 10^{-12}
350	4.17(44) × 10^{-11}	6.12(150) × 10^{-11}	9.15(360) × 10^{-12}
425	1.11(62) × 10^{-10}	1.69(30) × 10^{-10}	5.14(140) × 10^{-11}

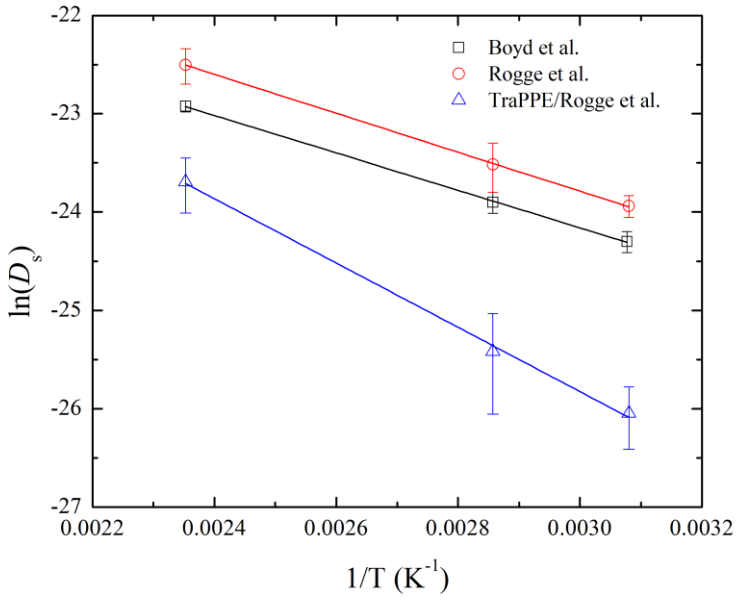

Figure 5. Arrhenius fit of diffusion coefficients for acetone in flexible UiO-66 for three different UiO-66 potentials.

To determine whether reasonable diffusion coefficients could be obtained for any molecule using the rigid UiO-66 model, we considered Ne, which has a kinetic diameter of 0.275 nm,[135] compared with the approximate window size of UiO-66 of about 0.6 nm.[27] One would not expect flexibility to play a measurable role when the diffusing species is significantly smaller than the window size. Surprisingly, we found that Ne diffuses 30% faster in the flexible MOF compared with the rigid model and that this difference is statistically significant. Diffusivities are given in Table 3. Hence, flexibility has an impact on diffusion, even when the window size is much larger than the kinetic diameter of the diffusing species for UiO-66. This indicates that simulation of diffusion in UiO-66 should use a flexible MOF model to obtain reliable results, especially when the size of the diffusing molecule is close to the size of the pore window. This is in contrast to MOFs such as NU-1000, where a rigid model has produced reasonable diffusion coefficients due to large pore size and channels present in the MOF.[114] The diffusion mechanism of light alkanes has been reported as intercage jumps in UiO-66,[113, 136] and that behavior is expected for this system as well. These results, taken together, indicate that ligand flexibility plays a significant role in the movement of molecules through pore windows in UiO-66.

Table 3. Diffusivities of Ne in UiO-66 using Boyd et al. flexible and rigid framework models.

Force field	D_s (m^2/s)
Flexible	$2.15(5) \times 10^{-8}$
Rigid	$1.44(6) \times 10^{-8}$

We have investigated the molecular-level mechanism of how framework flexibility impacts the diffusivity of acetone by measuring distances between pairs of specific carbon atoms on the

benzene rings of adjacent BDC linkers making up the triangular window between the pores of UiO-66 during the process of acetone traversing the pore window. Plots of the distance between atoms on adjacent pairs of linkers are given in Figure 6. The BDC linkers are roughly oriented so that one side of the ring is oriented toward the octahedral cage (blue lines) and one pointing at the tetrahedral cage (orange lines). Also shown in Figure 6 is the distance of the center of mass of the acetone molecule from the center of the window, along the tetrahedral to octahedral path. We see from Figure 6 that the orientation of the linkers dynamically respond as the acetone moves through the window. We note that the acetone molecule does not go through the exact middle of the window but is sometimes closer to one pair of linkers than the others during the transit. The plots show that the linkers open and close to allow acetone to move through the window with a lower barrier. We note that each linker is part of four different windows, so that when a pair of linkers "open" to allow a molecule to traverse the window, the windows to other pores are "closed". Hence it is impossible to orient the linkers such that they are "open" for all pores to which they belong. Plots of the distances between adjacent linkers, similar to the plots in Figure 6, but in the absence of acetone, are presented in Figure S7 of the Supporting Information. Comparison of Figure 6 and Figure S7 shows that the dynamic response of the linkers to the presence of acetone is dramatic.

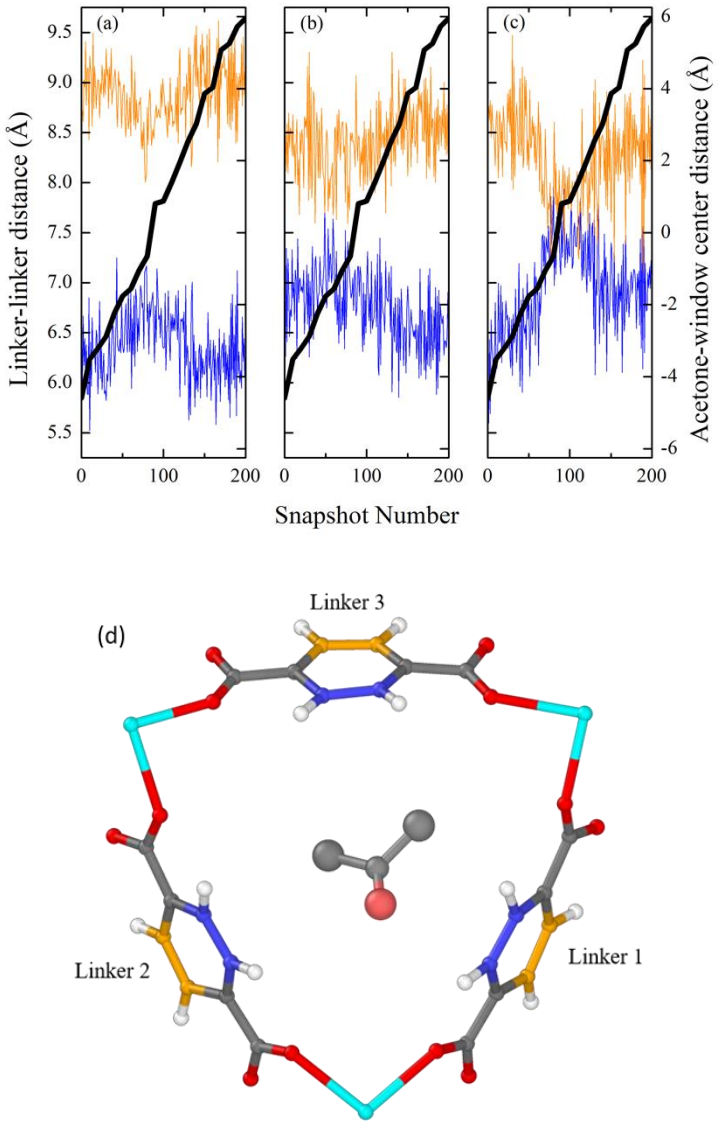

Figure 6. Distances between pairs of carbon atoms making up the window linkers as a function of time (snapshot) for acetone in transit from the tetrahedral to the octahedral pore. The blue lines are for the side of the rings facing the octahedral pore and the orange lines are for the tetrahedral pore facing side of the rings. Distances shown between (a) linkers 1 and 2, (b) linkers 1 and 3, and (c) linkers 2 and 3, with linkers identified in (d). The black line (right axis) is the distance from the acetone center of mass to the center of the transition window.

We next turn to the impact of finite loading on the diffusivity of acetone. We have computed the diffusivity as a function of loading for both the Boyd et al. and Rogge et al. potentials, as shown in Figure 7. We see qualitative agreement between these two potentials; diffusivity increases with increasing coverage, until the pores are filled with a liquid-like density of acetone, where the diffusivity decreases. This result is in agreement with reported literature results for CO_2 and CH_4 in dehydroxylated UiO-66, where diffusivity increased at low loading, and decreased approaching saturation.[113] Diffusion coefficients are included in Table 4.

We note that differences in the estimated errors for the diffusion coefficients in Table 4 are a result of using a different number of independent runs. We used 50 for the Boyd et al. potential, 25 for the Rogge et al. potential, and 10 for the TraPPE/Rogge et al. potential. Hence, the errors for the latter potential are much larger than the others but are still sufficiently small to distinguish the values from the other potentials. Use of a smaller number of independent simulations was for the sake of computational efficiency.

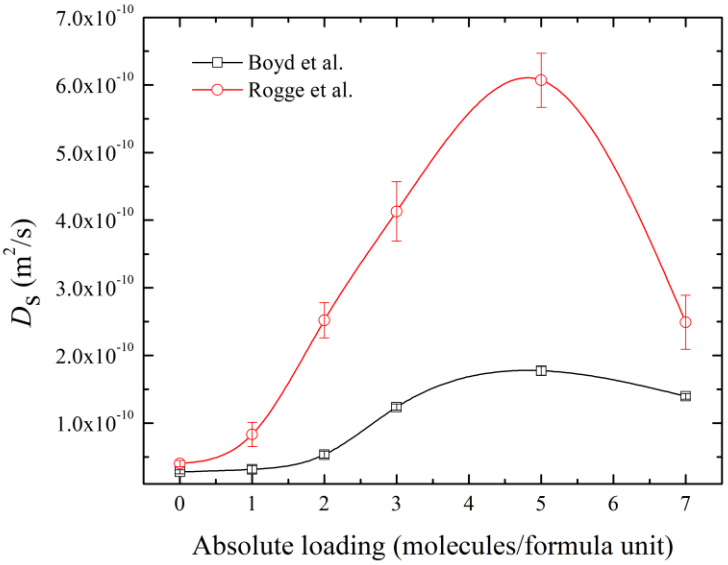

Figure 7. Effect of loading on the diffusion coefficient for the Boyd et al.[126] and Rogge et al.[127] potentials.

Table 4. Diffusion as a function of loading for acetone in a) Boyd et al. flexible UiO-66;[126] b) Rogge et al flexible UiO-66;[127] c) TraPPE/Rogge et al. UiO-66 at 325 K. Uncertainties in the least significant digits are given in parentheses (See Table 2).

***N* (molecules/cell)**	a) D_s (m^2/s)	b) D_s (m^2/s)	c) D_s (m^2/s)
0	2.80(30) × 10^{-11}	4.02(48) × 10^{-11}	4.88(150) × 10^{-12}
1	3.18(54) × 10^{-11}	8.33(180) × 10^{-11}	7.67(280) × 10^{-12}
2	5.35(50) × 10^{-11}	2.52(26) × 10^{-10}	1.92(53) × 10^{-11}
3	1.24(4) × 10^{-10}	4.13(44) × 10^{-10}	4.40(190) × 10^{-11}
5	1.78(7) × 10^{-10}	6.07(40) × 10^{-10}	1.44(48) × 10^{-10}
7	1.40(4) × 10^{-10}	2.49(40) × 10^{-10}	8.47(100) × 10^{-11}

We note that the quantitative values of diffusion coefficients from the Boyd et al. and Rogge et al. potentials are not in agreement within the estimated errors of the simulations, with the latter potential giving larger diffusivities (Table 4). After observing these differences, we carefully

examined the structures of UiO-66 predicted by these two potentials and found that the Boyd et al. potential gives a relaxed structure of the SBU that is unphysical, with some μ_3-O atoms relaxing toward the center of the SBU and overlapping. This can be seen from Figure S8 in the Supporting Information and a movie of the relaxation (just showing the SBU) also in the Supporting Information. This is surprising because the Boyd et al. potential was reported to give good values of the bulk modulus (UFF in Table 2 of Boyd et al.[126]). We therefore assume that the diffusivities computed from the Rogge et al. potential are more accurate than those computed from the Boyd et al. potential.

Up to this point, we have used published classical potentials to compute diffusivities of acetone in UiO-66. The Lennard-Jones terms for these potentials, which govern the van der Waals interactions between the acetone and framework, were taken from UFF.[82] However, we have not examined whether these classical potentials correctly account for hydrogen bonding between the μ_3-OH and acetone. Before doing this, it is important to establish whether or not acetone-framework hydrogen bonding is important.

As a second method for assessing the importance of acetone-framework hydrogen bonding, we have carried out DFT calculations to identify the most favorable binding sites for acetone in UiO-66. The strongest binding configuration found was of acetone in the μ_3-OH tetrahedral pore, with a binding energy of -87.5 kJ/mol. This configuration, shown in Figure 8, was strongest due to the formation of a hydrogen bond between the μ_3-OH hydrogen and the acetone oxygen. This value is in rough agreement with TPD-MS calculated binding energies. The strongest binding configurations found in the μ_3-O tetrahedral and octahedral pores are shown in Figure 9 and Figure 10, respectively. The energies of these configurations are -59.0 kJ/mol and -48.8 kJ/mol

respectively. These energies and relative binding energies are summarized in Table 5. The binding modes are likely dominated by electrostatic interactions.

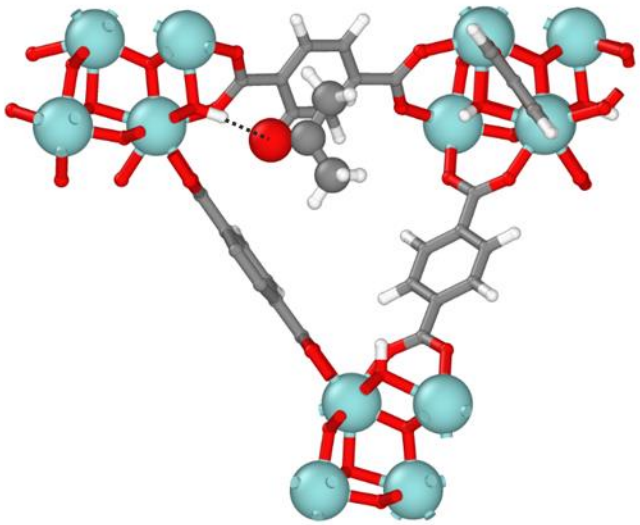

Figure 8. Configuration of local minima with the strongest binding energy for acetone in the μ_3-OH tetrahedral pore of UiO-66. The hydrogen bond between the μ_3-OH and the ketone oxygen is shown by the black dashed line. Atoms are as follows: White: H, gray: C, red: O, cyan, Zr. Created with OVITO.[85]

Table 5. Binding energies and relative binding energies of acetone in the three distinct pores of UiO-66, $\Delta\Delta E_{\mathbf{bind},i} = \Delta E_{\mathbf{bind},i} - \min(\Delta E_{\mathbf{bind},i})$

Pore	$\Delta E_{\mathbf{bind}}$ (kJ/mol)	$\Delta\Delta E_{\mathbf{bind}}$ (kJ/mol)
Tetrahedral with μ_3-OH	-87.5	0
Tetrahedral with μ_3-O	-59.0	28.5
Octahedral	-48.8	38.7

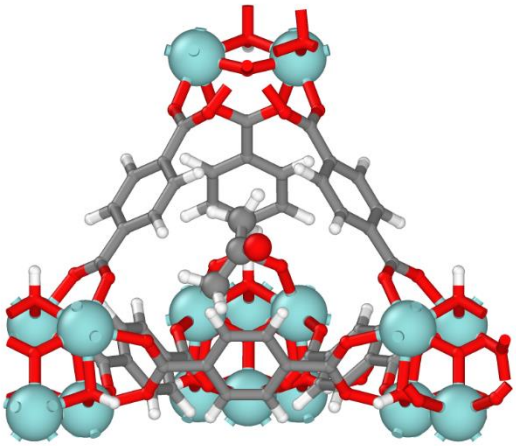

Figure 9. Configuration of local minima with the strongest binding energy for acetone in the μ_3-O tetrahedral pore of UiO-66. Atoms are as follows: White: H, gray: C, red: O, cyan, Zr. Created with OVITO.[85]

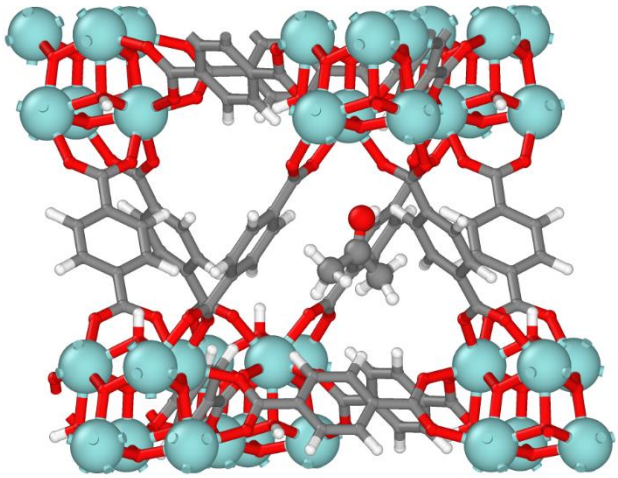

Figure 10. Configuration of local minima with the strongest binding energy for acetone in the octahedral pore of UiO-66. Atoms are as follows: White: H, gray: C, red: O, cyan, Zr. Created with OVITO.[85]

We have calculated binding energies of acetone in the different pores of UiO-66 using the Rogge et al. potential and the standard UFF Lennard-Jones terms and our calculated charges. We found, however, that this potential does not account for hydrogen bonding, as can be seen from the difference in binding energies of acetone in the tetrahedral μ_3-OH and μ_3-O pores of only 5.5 kJ/mol (Table S3 of the Supporting Information). Examination of the potentials identified the problem as being the Lennard-Jones diameter parameter used for hydrogen in the μ_3-OH group; this parameter effectively prohibits the oxygen atom of acetone from getting closer than about 0.28 nm to the H atom of μ_3-OH, whereas hydrogen bonds are typically less than 0.2 nm. Indeed, our DFT calculations give a hydrogen bond distance of about 0.18 nm for acetone μ_3-OH. We have therefore developed a modified potential for the adsorbate-framework cross interactions by replacing the O and H Lennard-Jones parameters for the μ_3-OH cross interactions with adsorbate molecules with the O and H parameters used for the TraPPE isopropanol potential,[137] namely, $\sigma_{\mathrm{H}} = \varepsilon_{\mathrm{H}} = 0, \sigma_{\mathrm{O}} = 0.302$ nm, $\varepsilon_{\mathrm{O}} = 93$ K. The binding energies for acetone in the pores using these cross-parameters are in very good agreement with our DFT calculations, with the binding energy of acetone in the tetrahedral μ_3-OH pore about 23 kJ/mol and 40 kJ/mol more favorable than in the tetrahedral μ_3-O and octahedral pores, respectively (see Table S4 of the Supporting Information). The absolute binding energy of acetone in the tetrahedral μ_3-OH pore is -75.4 kJ/mol, which is about 12 kJ/mol more weakly bound than predicted by DFT, and in excellent agreement with the TPD-MS results.

We have used this TraPPE/Rogge et al. potential to compute the diffusivities of acetone at zero loading as a function of temperature. The calculated values (Table 2) are roughly an order of magnitude smaller than the corresponding values for the Rogge et al. potential, which indicates that adsorbate-framework hydrogen bonding has a profound impact on the diffusivity. The

calculated barrier to diffusion computed from the Arrhenius equation from the TraPPE/Rogge et al. simulations (Figure 5) is 27.2 kJ/mol, which is 10.7 kJ/mol higher than without hydrogen bonding.

The diffusivities of acetone for the TraPPE/Rogge et al. potential as a function of loading are given in Table 4. Comparison with the diffusivities from the Rogge et al. potential reveal that hydrogen bonding decreases the diffusivity by about one order of magnitude at low loading and about a factor of 3 at high loading. A plot of the loading dependent diffusivities for the Rogge et al. and TraPPE/Rogge et al. potentials is given in Figure 11. We see from this figure that the diffusivity is qualitatively the same with and without hydrogen bonding but shifted to much lower values. From this we conclude that accounting for adsorbate-framework hydrogen bonding is necessary to get a quantitative picture of diffusion, but not required if one is only interested in the qualitative behavior.

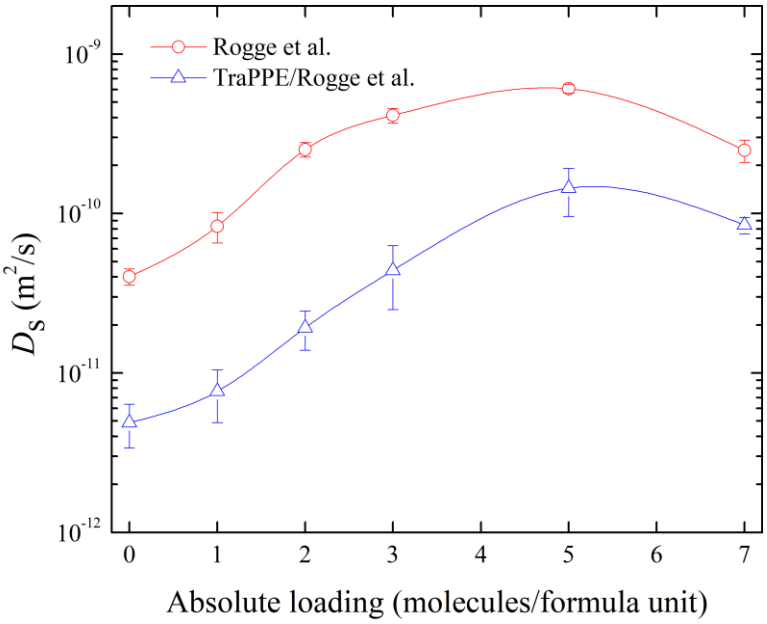

Figure 11. Loading dependent diffusivities for acetone in UiO-66 computed from the Rogge et al. potential and the TraPPE/Rogge et al. potential.

We have computed the fraction of acetone molecules that are hydrogen bonded to μ_3-OH groups as a function of loading (average over the length of the simulation) and also the fraction of μ_3-OH groups that are hydrogen bonded to acetone as a function of loading, shown in

Figure **12**. As expected, the fraction of acetone molecules hydrogen bonded decreases with increased loading and the fraction of μ_3-OH groups hydrogen bonded increases with loading. Even at high loading, the fraction of acetone molecules hydrogen bonded is surprisingly high. The fraction of μ_3-OH groups hydrogen bonded is always less than 50%, which indicates that steric hindrance likely prevents more than two acetone molecules in a single pore from forming hydrogen bonds to the μ_3-OH groups on the SBUs.

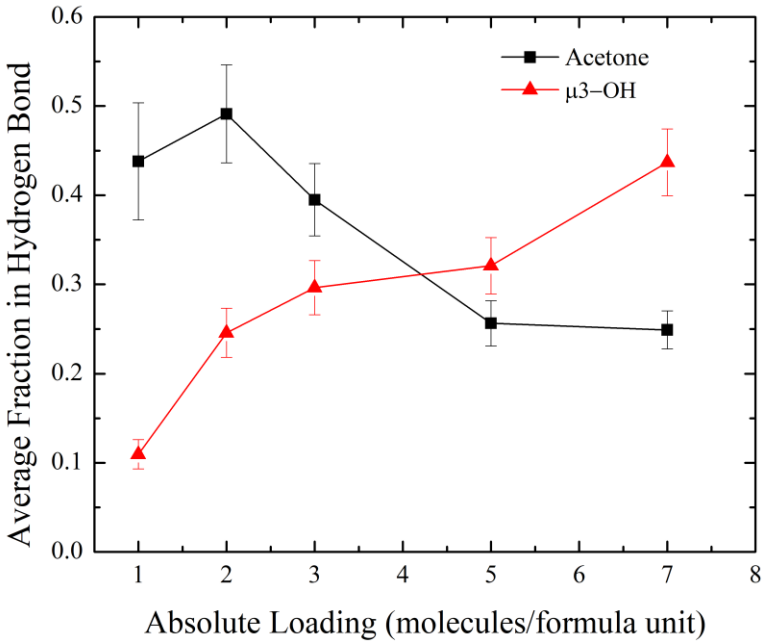

Figure 12. Fraction of acetone hydrogen bonded to framework μ_3-OH groups and the fraction of framework μ_3-OH groups that are hydrogen bonded to the node as a function of acetone loading in UiO-66 using the TraPPE/Rogge et al. potential.

2.6 Conclusions

We have shown that a flexible model potential model is necessary to obtain qualitatively correct diffusivities of acetone in UiO-66 and that the mechanism of diffusion involves the BDC linkers dynamically accommodating acetone as it moves through the triangular window of the pore. Diffusivities initially increase with loading at low coverage then decrease as saturation is approached. Hydrogen bonding between acetone and the framework μ_3-OH groups has been shown to be important from both experimental (TP-IR) and theoretical (DFT) studies. However, the potentials from the literature we have tested do not allow for an accurate accounting of

hydrogen bonding. We have constructed a modified potential that allows for hydrogen bond interactions between adsorbate molecules and the framework. Diffusivities computed with hydrogen bonding are roughly an order of magnitude smaller than when hydrogen bonding is ignored.

3.0 Interaction of HD and 2-Chloroethyl Ethyl Sulfide with a Series of Functionalized UiO-67 MOFs

3.1 Introduction

Recent events[138-141] have motivated interest in the development of novel materials to protect against chemical weapon attacks. While vesicants have not attracted as much recent attention as the nerve agent classes (G and V), they are still an important consideration in the development of new CWA mitigation materials. The ideal material should be effective across a range of agent classes, including both vesicants and nerve agents. We have recently studied the metal organic framework (MOF) UiO-67-X, with X being a series of ligand functionalizations, for the capture of the nerve agent simulant dimethyl methyl phosphonate (DMMP).[1] We aim to use stratified MOFs containing a different functionalization in each strata[37] to concentrate CWAs for detection and destruction. Therefore, while there are known methods to destroy HD,[142-144] it is important to evaluate our new technology on the vesicant class to determine if it might meet the criteria of a widely effective material. In our previous work, we found that UiO-67-NH_2 had the greatest affinity for DMMP out of the MOFs studied, while UiO-67 had the least affinity.[1]

MOFs have drawn substantial attention for toxic species removal.[5, 145-151] Simulant molecules are often used as safer (and legal, with regard to experimental work) surrogates to approximate the behavior and properties of HD. Among these simulants, 2-chloroethyl ethyl sulfide (2-CEES)[152-157] is most common, although dialkyl sulfides[158] and thilolane[159] have also been used. Of particular interest here is the work of Roy et al.[157] who studied degradation of both HD and 2-CEES on HKUST-1 and found the 16 min^{-1} 2-CEES half-life was half the 35 min^{-1} half-

life of HD. This raises questions about the suitability of using 2-CEES as a simulant for HD in MOFs that we aim to address here, although we limit the scope of our work to considering physisorption processes. It is further important to consider that the degradation products of HD decomposition are often toxic themselves,[160-162] with some exceptions being the partial oxidation of HD to the non-vesicant sulfoxide[163] and hydrolysis to thiodiglycol.[164-165] Therefore any study of HD that considers degradation must also consider the reaction products. Nanocatalysts have shown promise in CWA applications,[166] and we aim to use them as the reaction site, allowing the MOFs to remain intact. Therefore, we limit the scope of this work to non-reactive systems.

Peterson et al. considered loading of 2-CEES on UiO-67-NH_2.[34] They varied levels of missing linker defects from 0.55 to 1.27 defects out of 12 per secondary building unit (SBU) (while noting that analysis showed missing SBUs as well) and found only moderate changes in loading and an uptake of ~4.5 mol/kg, which was comparable to loading of Cl_2, a much smaller molecule. They proposed that the amine group is reactive toward 2-CEES, although that may be unlikely because aniline is both a poor nucleophile and a weak base. It may be that reactions are occurring at defective sites within the MOF; Vo et al.[167] have demonstrated the importance of defects on reactivity of organophosphates on UiO-66, and it is possible that defects are required for reactions of HD/2-CEES as well.

Here we use density functional theory (DFT) to evaluate the effect of ligand functionalization on UiO-67-X interactions with HD and the simulant 2-CEES. We evaluate the systems to identify the optimal binding site for each MOF with both HD and 2-CEES and compare the performance of the MOFs at trapping both analytes, and determine whether 2-CEES is sufficient in these systems to serve as a simulant molecule for HD. This will inform our design of stratified MOFs capable of capturing a wide range of CWAs.

3.2 Methodology

We consider the ligands shown in Appendix Figure B1 based our previous work on MOFs and CWA simulants.[1] Ligands were functionalized to produce multiple pore environments within the μ_3-OH tetrahedral pore of UiO-67 in the following manner: functionalization sites were chosen to give environments with 0, 1, 2, and 3 functionalized rings neighboring a μ_3-OH site. Binding energies for both HD and 2-CEES in the periodic MOF structures were calculated using a procedure which has been reported previously.[1] In summary, the functionalized linkers were incorporated into perfect UiO-67 primitive cells. The atom positions, using lattice parameters of relaxed UiO-67 ($a = b = c = 19.1$ Å, $\alpha = \beta = \gamma = 60°$), were then relaxed using DFT as implemented in CP2K.[55-57] The lattice parameters of each MOF were not relaxed because it has been shown that there is minimal difference between the cell parameters of functionalized ligand MOFs.[58] The Goedecker-Teter-Hutter pseudopotentials[59] were used with the DZVP-MOLOPT-SR basis set,[60] and Grimme's dispersion correction[50] was applied. The cutoff and relative cutoff were 400 Ry and 50 Ry, respectively. These values have been verified as converged previously.[1] The conjugate gradient orbital transformation minimizer[134] and LBFGS optimizer[61] were used. These settings were used for all other CP2K calculations in this work. Isolated gas phase HD and 2-CEES molecules were also relaxed using this procedure, with a box length of 23 Å.

The ground state energy of a single HD and 2-CEES molecule in each UiO-67-X MOF was estimated using the following procedure: A single analyte molecule was randomly placed into the μ_3-OH containing tetrahedral pore of each primitive cell. Ab initio molecular dynamics (AIMD) simulations in the canonical ensemble were carried out on the periodic system at a temperature of 1000 K using the GLE thermostat.[62-63] The AIMD simulations were run for 7.5 ps, using a timestep of 0.5 fs. The coordinates of the AIMD simulations were saved every 100 timesteps and the

sampled geometries were relaxed in CP2K to their local minima using the procedure described in this work. The lowest energy structure identified was used to compute the binding energy for each functionalized MOF as described in Chapter 1. Strongest binding energy structures for each MOF were then retested by substituting functional groups for all other MOFs into these structures as additional configurations to test.

Strain calculations were performed to measure the changes to each MOF due to the presence of the analyte. The analyte was removed from the binding configuration of each MOF, and a single point energy was calculated using the same settings as the geometry optimization calculations. The strain energy was calculated using eq (3-1), where E_{A*B} is the energy of the binding configuration with the analyte removed, and E_B is the energy of the relaxed MOF structure.

$$E_{strain} = E_{A*B} - E_B \tag{3-1}$$

3.3 Results and Discussion

The strongest binding site observed is the two neighboring functionalizations μ_3-OH group found within the tetrahedral pores of each MOF. This trend is consistent across all MOF studied for both analytes. Calculated binding energies are reported in Figure 13 and tabulated in Appendix Table B1. The MOFs are ordered from greatest to least binding energy between HD and each MOF. The average binding energy with HD is 17 kJ mol stronger than that of 2-CEES. This may have implications for calculations of transport properties such as diffusion. It is known that the mechanism of diffusion through UiO-6X MOFs is jumps between tetrahedral and octahedral

pores.[113] The energy differences observed here indicate that HD may diffuse more slowly than 2-CEES through these MOFs. The standard deviations of the binding energies are ~11 kJ/mol.

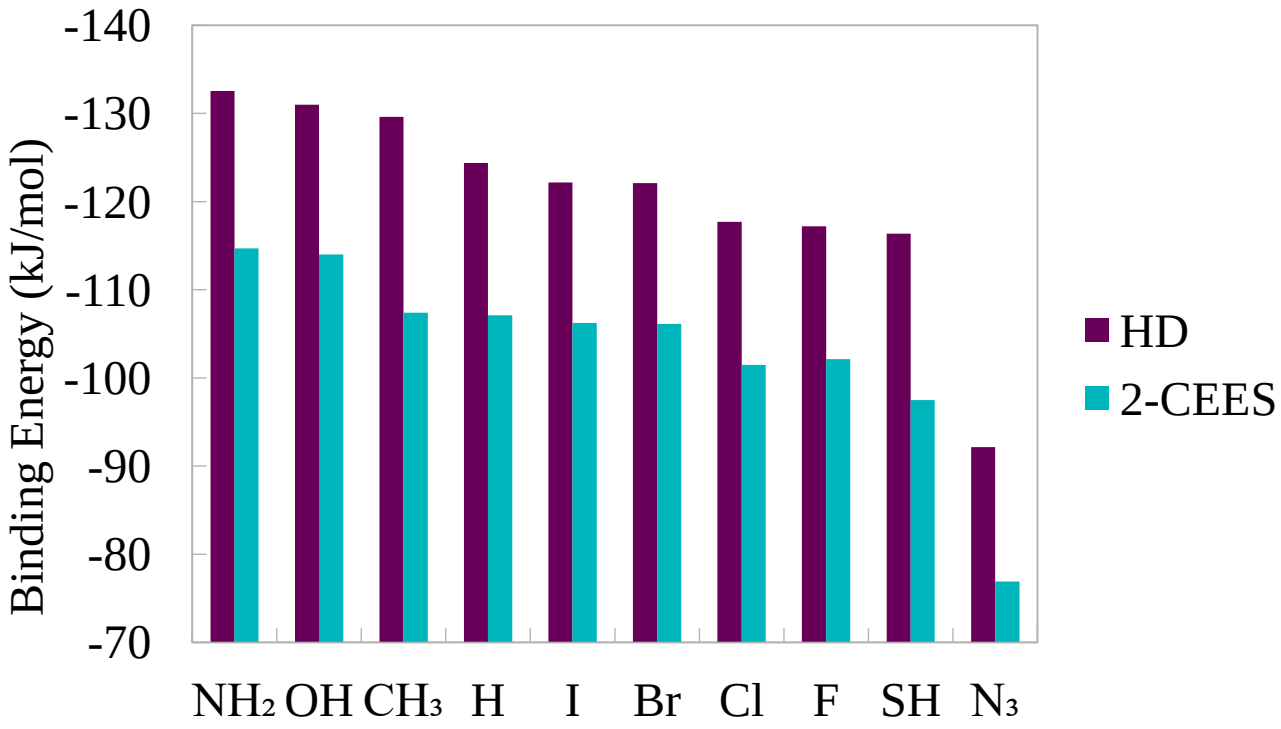

Figure 13. Binding energies of local minima for HD and 2-CEES with functionalized UiO-67-X MOFs.

The binding configurations of HD and 2-CEES in UiO-67-NH_2 are shown in Figure 14. Hydrogen bonds and electrostatic interactions are shown with dashed lines. For HD, the primary modes of interaction are electrostatic attractions on the order of 3 Å between the Cl atoms and hydrogen atoms on the ligands, and through a 2.65 Å hydrogen bond between the μ_3-OH group on the secondary building unit (SBU) of the MOF and the S atom in HD. 2-CEES has a similar binding mode, but is not bound as strongly because there is only one Cl atom forming electrostatic

interactions with the ligands. Overall, UiO-67-NH_2 has the strongest interactions with both HD and 2-CEES, which can likely be attributed to the ~2.9 Å interactions between the HD Cl atoms and the NH_2 substituent. While this interaction cannot be considered a hydrogen bond under the updated IUPAC guidelines due to the deviation from a 180° angle,[168] it is a strong electrostatic interaction relative to most of the other interactions observed in this work based on the distance between the atoms. These same binding configurations were observed for the other hydrogen bonding functionalizations considered, UiO-67-OH and UiO-67-SH, which are shown in Appendix Figure B2 and Appendix Figure B3 respectively. The binding energies of UiO-67-NH_2 and UiO-67-OH are effectively the same, both are ~ -132 kJ/mol with HD and ~ -114 kJ/mol with 2-CEES. However, the binding energies of HD and 2-CEES with UiO-67-SH are -116 kJ/mol and -97 kJ/mol, a difference of ~17 kJ/mol for each. Differences in energies of these three MOFs with the analytes are probably not attributable to the increasing distance and decreasing angle[168] of the XH-Cl interaction, where X is ordered as N, O, S. These values are included in Appendix Table B2. The difference in XH-Cl distances is negligible, and the change in angles in consistent across all three functional groups, which does not explain the similar energies obtained for UiO-67-NH_2 and UiO-67-OH. It may be that the electronegativity of the hydrogen bond acceptor impacts the strength of these interactions. S is in the third period, while N and O are both in the second.

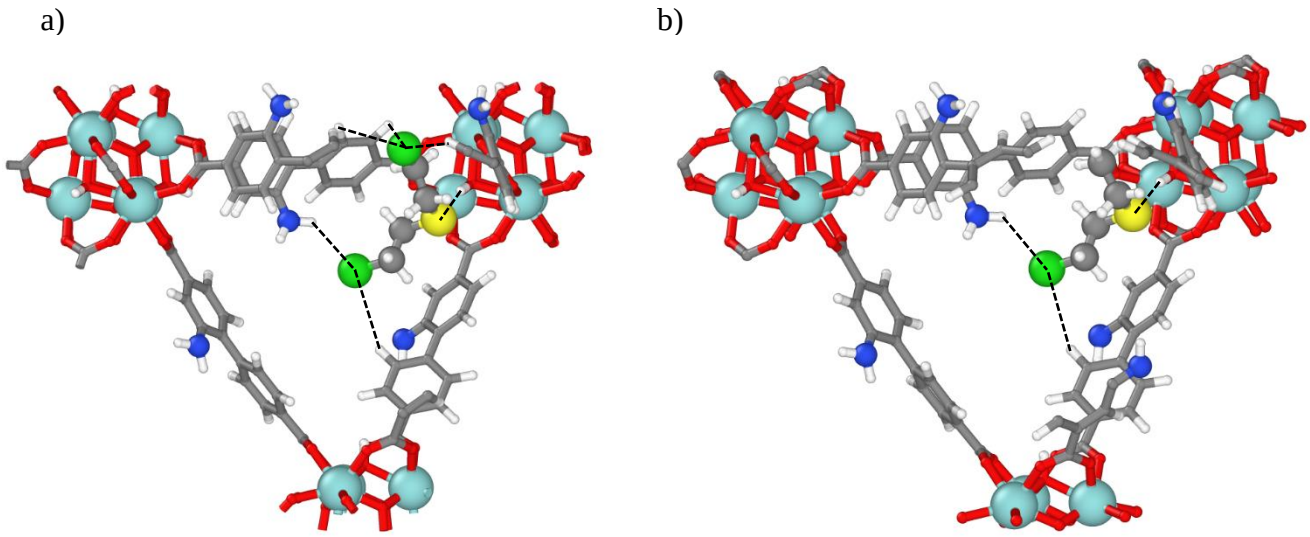

Figure 14. Binding configurations in UiO-67-NH_2 a) HD: The distances for upper Cl-H electrostatic interactions are, from left to right, 3.98 Å, 3.99 Å, and 3.37 Å. The S···H hydrogen bond is 2.65 Å. The NH-Cl interaction is 2.89 Å. The distances for lower Cl-H electrostatic interaction is 3.68 Å. b) 2-CEES: The S···H hydrogen bond is 2.58 Å. The Cl-H electrostatic interaction distance is 3.57 Å and the NH-Cl interaction distance is 2.91 Å. Zr is shown in teal, C in grey, O in red, H in white, S in yellow, Cl in green, and N in blue.

The binding configurations of HD and 2-CEES with UiO-67-CH_3 are shown in Figure 15. The energy difference between the HD and 2-CEES binding energies can be attributed to additional electrostatic interactions on the order of 3 Å between H atoms on the ligands and the second Cl atom found in HD, as was the case for UiO-67-NH_2. Relative to the other MOFs studied, these interactions are the second strongest after UiO-67-NH_2. The methyl substituents on the ligands allow for weak electrostatic interactions between the methyl H atoms and the HD and 2-CEES Cl atoms, similar to the hydrogen bonder functionalizations. There are also two methyl groups interacting with each analyte, further increasing the magnitude of the binding energy.

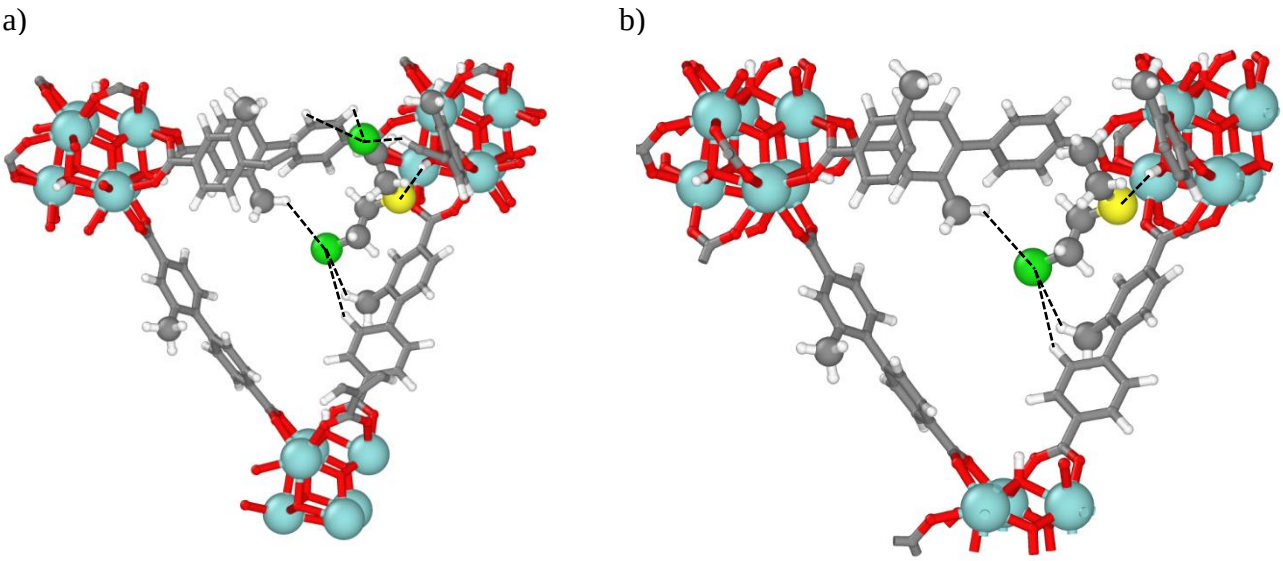

Figure 15. Binding configurations in UiO-67-CH_3. a) HD: The distances for upper Cl-H electrostatic interactions are, from left to right, 3.99 Å, 3.96 Å, and 3.16 Å. The S···H hydrogen bond distance is 2.62 Å. The lower Cl-H electrostatic interaction distances, clockwise from vertical, are 3.18 Å, 3.33 Å and 3.09 Å. b) 2-CEES: The S···H hydrogen bond distance is 2.58 Å. Cl-H electrostatic interaction lengths, clockwise from vertical, are 3.16 Å, 3.38 Å, and 3.00 Å. Zr is shown in teal, C in grey, O in red, H in white, S in yellow, and Cl in green.

The binding configurations of HD and 2-CEES in UiO-67 are shown in Figure 16. The HD structure has similar interactions to those seen with UiO-67-CH_3, but in this case the distances tend to be larger as the interacting hydrogens are on the aromatic rings as opposed to the methyl groups. This is apparent from the energies as well, with HD interacting more strongly with UiO-67-CH_3 by 5 kJ/mol. The 2-CEES binding modes for UiO-67-CH_3 and UiO-67 are similar in that there is effectively no energy difference between the structures: both are -107 kJ/mol.

a) b)

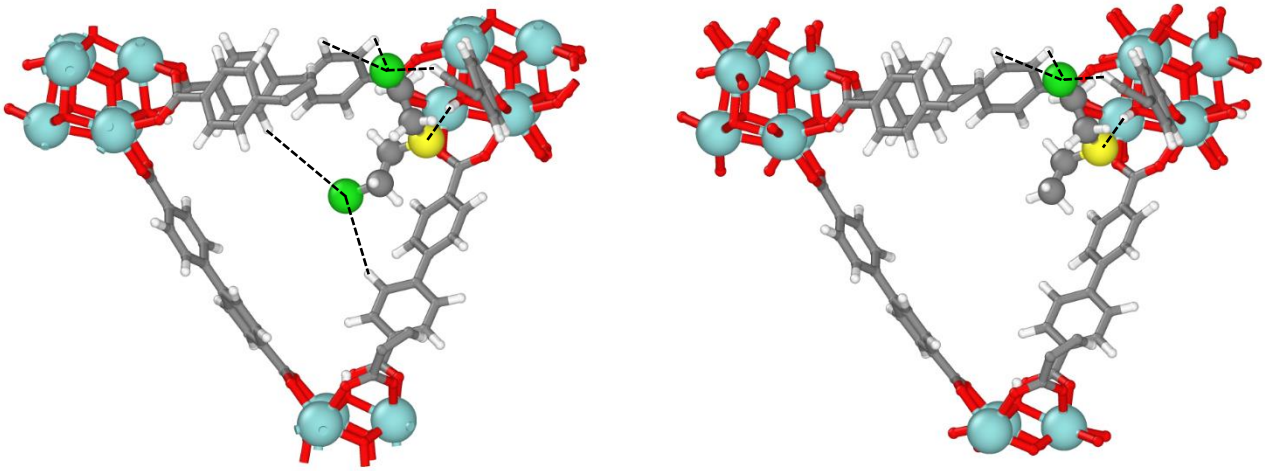

Figure 16. Binding configurations in UiO-67. a) HD: The upper Cl-H electrostatic interaction distances are, from left to right, 4.02 Å, 3.93 Å, and 3.64 Å. The S···H hydrogen bond distance is 2.63 Å. The lower Cl-H electrostatic interaction distances are, clockwise from vertical, 3.54 Å and 4.45 Å. b) 2-CEES: The Cl-H electrostatic interaction distances are, from left to right, 4.07 Å, 3.94 Å, and 3.60. The S···H hydrogen bond distance is 2.55 Å. Zr is shown in teal, C in grey, O in red, H in white, S in yellow, and Cl in green.

The binding configurations of HD and 2-CEES with UiO-67-I are shown in Figure 17. As was the case for the hydrogen bonders, UiO-67-CH_3, and UiO-67, the stronger interaction between HD as compared to 2-CEES results from the electrostatic interactions between the additional Cl atom in HD and the ligands. This trend is repeated for the Br, Cl, and F functionalized MOFs, configurations which are shown in Appendix Figure B4 through Appendix Figure B6. Unlike the other MOFs studied, there is a repulsive interaction in each of HD configurations between a Cl atom in HD and a halogen on the ligand. These atom pair distances are tabulated in Appendix Table B3, and do not change significantly based on the halogen present in the ligand. While the

binding energies appear to follow a periodic trend, with smaller binding energies as electronegativity increases, the energies are so close that drawing such a conclusion is not justified. As an example, the energies for UiO-67-I and UiO-67-Br differ by no more than 0.1 kJ/mol for both HD and 2-CEES. Overall, there is effectively no difference among any of the halogens. The mean energy with HD is -120 kJ/mol with a standard deviation of 2.7 kJ/mol, while the mean energy for 2-CEES binding is -103 kJ/mol with a standard deviation of 2.5 kJ/mol.

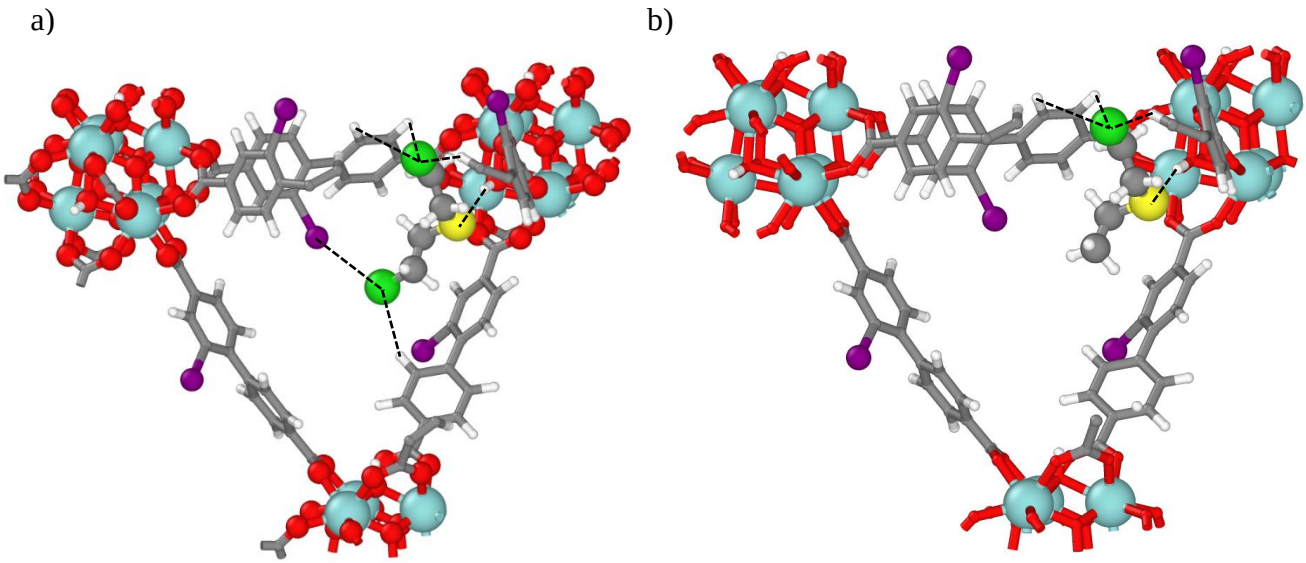

Figure 17. Binding configurations in UiO-67-I. a) HD: The upper Cl-H electrostatic interaction distances are, from left to right, 4.07 Å, 4.01 Å, and 3.46 Å. The S···H hydrogen bond distance is 2.58 Å. The Cl-I distance is 3.65 Å. The lower Cl-H electrostatic interaction distance is 3.06 Å. b) 2-CEES: The Cl-H electrostatic interaction distances are, from left to right, 4.15 Å, 4.05 Å, and 3.38 Å. The S···H hydrogen bond length is 2.52 Å. Zr is shown in teal, C in grey, O in red, H in white, S in yellow, Cl in green, and I in purple.

The binding configurations of HD and 2-CEES in UiO-67-N_3 are shown in Figure 18. While the optimal configurations resemble those found for other MOFs, the energies for both are ~20 kJ/mol weaker than the next weakest interactions, those with UiO-67-SH. To understand why the azide group binds so weakly compared to the other groups studied, we calculated dihedral torsion angles between the two aromatic rings in each linker using the atomic coordinates shown in Appendix Figure B7 and Avogadro 1.2.[169] Using the ligand labels shown in Appendix Figure B8, the dihedral torsions for UiO-67-N_3 are reported in Table 6. From examining these data, the deviation from equilibrium position of the ligands is ~4.5° on each ligand. Greater deviations from the angles of the empty MOF correspond to increased ring strain, which negates some of the favorable interactions formed between the analyte and MOF, reducing the binding strength. The nature of the azide functional group lends itself to greater ring strain. As the group is larger than others considered here and linear, the introduction of analyte molecules into the pore results in close unfavorable electrostatic interactions between N_3 and the analyte to a greater degree than that exhibited by other functionalizations, as shown in Figure 19 and confirmed by the dihedral torsion angles calculated for the other MOFs considered in this work, tabulated in Appendix Table B4 through Appendix Table B 12, and reported in the order they were mentioned. The average deviations for all of these are < 2° except for the SH and CH_3 functionalizations. This results in significantly lower binding energies for UiO-67-N_3 as compared to the other MOFs studied.

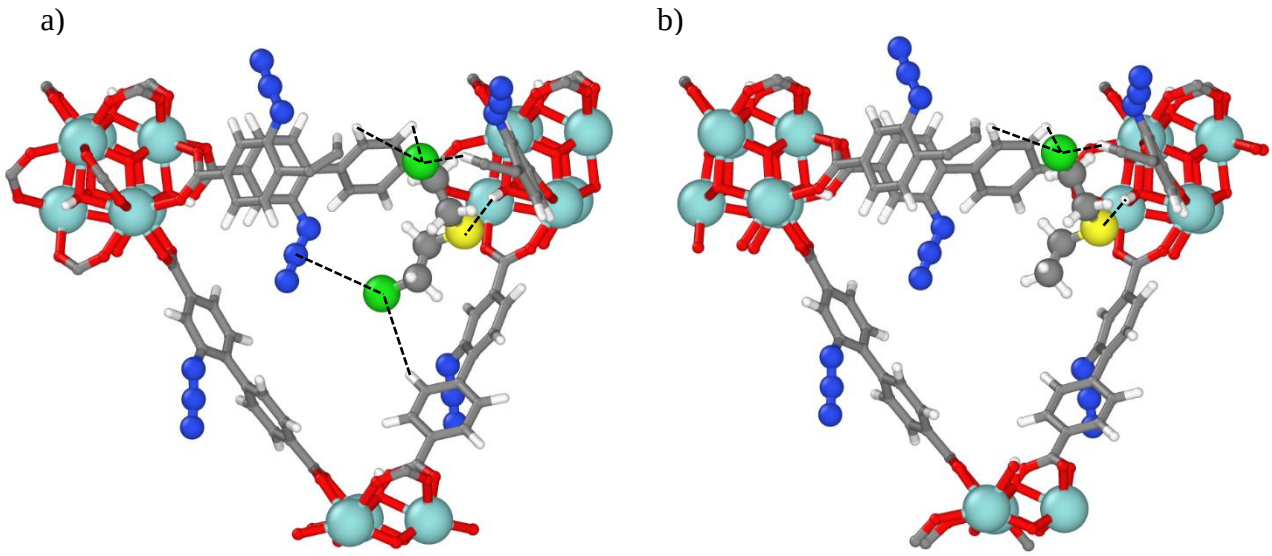

Figure 18. Binding configurations in UiO-67-N_3 a) HD. The upper Cl-H electrostatic interaction distances are, from left to right, 4.09 Å, 4.13 Å, and 3.39 Å. The S···H hydrogen bond length is 2.56 Å. The Cl-H electrostatic interaction distance is 3.55 Å. The Cl-N distance is 3.98 Å. b) 2-CEES. The Cl-H electrostatic interaction distances are, from left to right, 4.13 Å, 4.04 Å, and 3.35 Å. The S···H hydrogen bond length is 2.49 Å. Zr is shown in teal, C in grey, O in red, H in white, S in yellow, Cl in green, and N in blue.

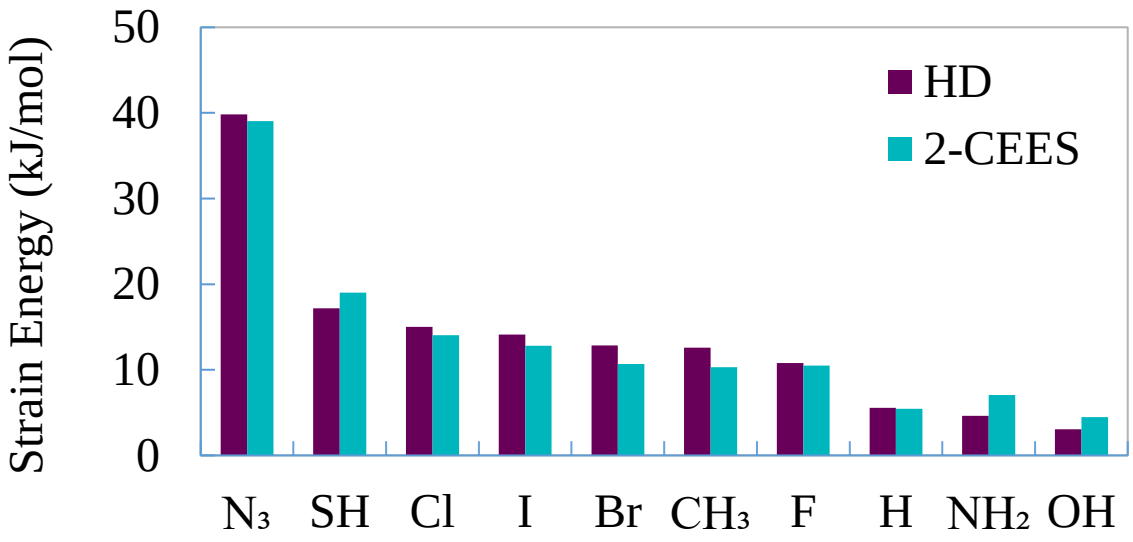

Figure 19. Strain energies calculated for each MOF analyte pair.

Table 6. Dihedral torsion angles for the ligands of UiO-67-N_3.

	Angle (°)			Δ°		
Ligand	**HD**	**2-CEES**	**Void MOF**	**HD/2-CEES**	**HD/Void**	**2-CEES/Void**
A	45.4	46.2	39.0	0.8	6.4	7.2
B	38.5	39.4	44.4	0.9	5.9	5.0
C	-39.9	-40.0	-44.2	0.1	4.3	4.2
D	-43.3	-42.0	-39.3	1.3	4.0	2.7
E	-45.1	-45.2	-41.1	0.1	4.0	4.1
F	-39.6	-39.6	-43.6	0.0	4.0	4.0
Average (magnitude)	**42.0**	**42.1**	**41.9**	**0.5**	**4.8**	**4.5**
Std Dev	**2.7**	**2.7**	**2.2**	**0.5**	**1.0**	**1.4**

3.4 Conclusions

The strongest affinity for HD and 2-CEES was UiO-67-NH_2, as was the case for our study on DMMP. We find that while 2-CEES may be suitable for predicting HD trends in MOFs, studies focused on reliable property calculations should use HD where possible. In particular, the interactions of HD with the MOFs generally involve multiple ligands, and this effect is likely to impact studies of transport properties. We further find that ligand functionalization does affect the binding energy of HD and 2-CEES in UiO-67-X MOFs; although it does not change the binding site, there are configurational differences that result in substantial contributions to the binding energies. The main interaction observed is the formation of a hydrogen bond between the μ_3-OH group and the S atom in both HD and 2-CEES. The interaction that modifies the binding strength of each MOF with the analytes is electrostatic interactions. We find that both repulsive and attractive electrostatic interactions contribute to the interactions identified in this work.

4.0 Interaction of GB, VX, and A-234 with Pristine Functionalized UiO-67-X Metal-Organic Frameworks

4.1 Introduction

There have been several attacks using chemical warfare agents in the past decade that motivate this work. The first of these incidents is the deployment of munitions containing GB in Syria in 2013.[138] GB has two isomers. The *S* isomer (*S*-propan-2-yl methylphosphonofluoridate), shown in Figure 20, is more toxic,[170-171] and will be a subject of this work.

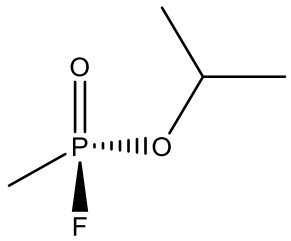

Figure 20. The *S* isomer of GB.

The second incident involves the assassination of Kim Jong-nam with VX in the Kuala Lumpur International Airport in 2017.[139] There are two isomers of VX. As in GB, the *S* isomer (*O*-ethyl *S*-[2-(diiso-propylamino)ethyl] methylphosphonothioate), shown in Figure 21, is the more toxic of the two,[170] and is a subject of this work.

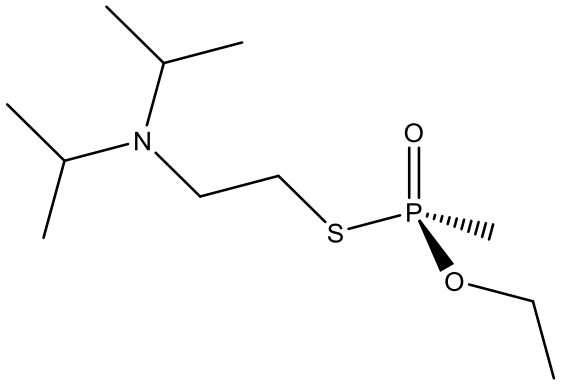

Figure 21. The *S* isomer of VX.

The third and fourth incidents are the attempted assassinations of Sergei Skripal in Salisbury, England, in 2018,[140] and Alexei Navalny in 2020.[141] There has been some debate regarding the identity of the suspected agent, A-234 (ethyl N-[(1E)-1-(diethylamino)ethylidene]-phosphoramidofluoridate).[172-174] Here, we will consider A-234 to be the structure proposed by Mirzayanov,[174] shown in Figure 22, following the lead of previous literature accounts.[175-177] There is little mention of A-234 in the published literature, as interest in the Novichok agents has largely developed because of these attacks. We note that phosphorous is a stereocenter in Mirzayanov's representation of A-234. We have not found any literature indicating whether the *R* or *S* isomer is more toxic, so we will proceed using the *S* stereoisomer following the pattern of GB and VX.

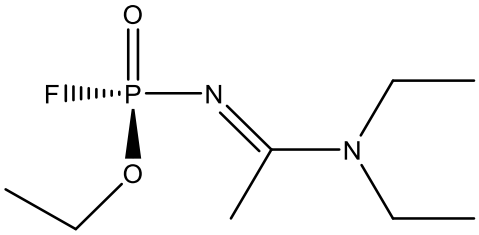

Figure 22. A-234 as identified by Mirzayanov,[174] with the specification of *S* stereochemistry. While other authors[172-173] report a different molecule, previous literature accounts[175-177] focus on the molecule presented here.

These incidents have motivated research into new materials and methods capable of mitigating the damage wrought by such attacks. One material that has shown promise in capturing and degrading CWAs are metal-organic frameworks.

While there are published examples of experimental work[13, 34, 157, 176] on CWAs with MOFs, prohibitions on the possession of such materials limit such work to a select few governmental institutions. As such, published research, including simulation-based work, focuses on simulant molecules, with some common examples being 2-CEES[178] for the blistering agent HD, and both DMMP[1, 22, 179] and DMNP[98, 178, 180-181] for G class nerve agents including GB (sarin) and GD (soman). While some studies consider GD[13, 34] here we will focus on GB because it was used in the attack described above. It is also easier to synthesize and less expensive than GD, with the latter requiring pinacolyl alcohol as opposed to isopropanol.[182] Further, separation of the four stereoisomers produced in the synthesis of GD adds a further hurdle to its use,[183] so one might expect that GB is more likely to be used in an attack. For these reasons, we will focus on GB.

In our previous work, we considered the interactions of 2-CEES and HD with a series of 10 functionalized UiO-67-X MOFs. We found significant differences in the interaction energies of 2-CEES and HD with several of the MOFs studied. Soares et al. found differences in adsorption of between agent and simulant molecules in adsorption Monte Carlo simulations.[184] This motivates the need for more computational studies of agents to help develop effective materials for capture and destruction. In situations where similarities between agent and simulant behavior break down, or the risk of live agent studies is greater than the potential benefits of the work, simulation-based methods can fill the gap.

Some published works that consider reactive systems do not address the effect of defects[19, 98] although it has been shown that the presence of missing linker defects is a major contributor to the destruction of both agent and simulant using MOFs.[22, 185] While UiO-67 MOFs have been synthesized in the range 0% to 30% missing linker defects,[186-187] here we consider pristine systems to develop understanding of the MOF + agent interactions in a non-reactive environment.

Peterson et al. studied the effect of missing linker defects (0.55, 1.02, and 1.27 linkers missing per secondary building unit (SBU)) on the uptake of Cl_2, and 2-CEES, and the hydrolysis (in an *N*-ethylmorpholine buffer) of DMNP, GD, and VX in UiO-66-NH_2.[185] They found a tradeoff between reactive sites and diffusion in their synthesized materials. The removal of additional linkers allowed for diffusion deeper into the MOF but removed active sites. DMNP, GD, and VX all underwent hydrolysis reactions. Katz et al.[19] found that UiO-67 is a stronger catalyst (again in *N*-ethylmorpholine) for methyl-paraoxon hydrolysis (an organophosphate pesticide) than UiO-66. They propose that methyl-paraoxon is so large that it does not enter the MOF; only the surface sites of UiO-66 were catalytically active. Katz et al. also consider UiO-67-NH_2 and find that it has similar activity, with turn-over frequencies on the same order of magnitude. They expect that only

surface sites are active on UiO-67, and do not consider the effect of defects on their results. Peterson et al. found a half-life one order of magnitude greater for all agents studied in their experiments with the best performing MOFs than that reported for methyl-paraoxon by Katz et al. and several orders of magnitude greater than those predicted by Katz el al. for low-defect materials, which indicates variability in hydrolysis rates for different organophosphates. An important limitation of both of these works is the necessity of a buffer for hydrolysis. This may not be realistic for field applications; hence the use of buffer solution and solvents will not be considered here. For this study, we selected UiO-67 as the base MOF, considering that Peterson et al. found the pores of UiO-66 were too small to admit the studied organophosphates, and Katz et al. studied methyl paraoxon, which contains a bulky benzene group that may hinder diffusion of the molecule into the MOF; noting that the three agents considered here do not contain such a bulky group. We examine the NH_2 functionalization analogous to that studied by Peterson et al, along with the hydrogen bonding OH functionalization and the unfunctionalized MOF to understand the contributions of the functional group to the MOF + agent interaction.

Here we describe, for the first time, interactions of CWAs, including a Novichok agent, with UiO-67-X MOFs through the application of density functional theory (DFT). To the best of our knowledge, there are no examples at all of MOF studies that consider A-234. We hope to develop an understanding of how A-234 interacts with the functionalized UiO-67 MOFs and compare that to the behavior of GB and VX. The ideal protection material must function against a variety of chemical agents.

A-234 is easier to synthesize and more persistent than VX.[175] As such, we expect it will garner greater attention in coming years as nations develop defenses for it, and rogue actors attempt

to obtain stockpiles of it for future attacks. Therefore, we hope this work serves as the first of many studies targeted to protection against attacks with A-234.

4.2 Computational Methods

We consider the ligands shown in Figure 23 based on our previous work on MOFs and CWAs.[1]

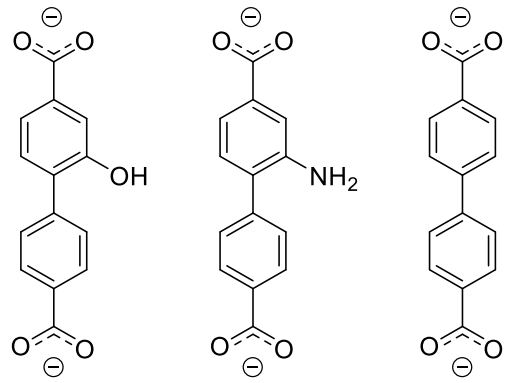

Figure 23. Biphenyl dicarboxylate (BPDC) based ligands considered in this work are based on previous studies.[1] From left to right: BPDC-OH, BPDC-NH_2, BPDC.

Ligands were functionalized to produce multiple pore environments within the μ_3-OH tetrahedral pore of UiO-67 in the following manner: functionalization sites were chosen to give environments with 0, 1, 2, and 3 functionalized rings neighboring a μ_3-OH site. Binding energies for GB, VX, and A-234 in the periodic MOF structures were calculated using a procedure which

has been reported previously.[1] In summary, the functionalized linkers were incorporated into perfect UiO-67 primitive cells. The functional groups were placed to create pockets with 0, 1, 2, and 3 functional groups on the adjacent rings of the ligands. The atom positions, using lattice parameters of relaxed UiO-67 ($a = b = c$ = 19.1 Å, $\alpha = \beta = \gamma = 60°$), were then relaxed using DFT as implemented in CP2K 5.1.[55-57] The lattice parameters of each MOF were not relaxed because it has been shown that there is minimal difference between the parameters of functionalized ligand MOFs.[58] The Goedecker-Teter-Hutter pseudopotentials[59] were used with the DZVP-MOLOPT-SR basis set,[60] and Grimme's dispersion correction[50] was applied. The cutoff and relative cutoff were 400 Ry and 50 Ry, respectively. These values have been verified as converged previously.[1] The conjugate gradient orbital transformation minimizer[134] and LBFGS optimizer[61] were used. These settings were used for all other CP2K calculations in this work. Isolated gas phase GB, VX, and A-234 molecules were also relaxed using this procedure.

The ground state energy of a single GB, VX, and A-234 molecule in each UiO-67-X MOF was estimated using the following procedure: Two systems were considered for each MOF + analyte pair. In the first, a single analyte molecule was placed into the octahedral pore of each primitive cell. In the second, the analyte was placed into the μ_3-OH tetrahedral pore. Ab initio molecular dynamics (AIMD) simulations in the canonical ensemble were carried out on the periodic system at a temperature of 1000 K using the GLE thermostat.[62-63] The AIMD simulations ran for 5 ps, using a timestep of 0.5 fs. The coordinates of the AIMD simulations were saved every 100 timesteps and the sampled geometries were relaxed in CP2K to their local minima. The lowest energy structure from the two systems for each MOF + analyte pair was used to compute the binding energy via eq (4-1). Strongest binding energy structures for each MOF were then retested by substituting functional groups for all other MOFs into these structures as additional

configurations to test. Additional structures were generated by swapping agent molecules at strong binding sites.

$$\Delta E_{\text{bind}} = E_{AB} - E_A - E_B \tag{4-1}$$

4.3 Results

4.3.1 GB

Binding energy differences and configurations of GB in UiO-67-X are shown in Figure 24. Binding energies and binding energy differences are tabulated in Table 7**.**

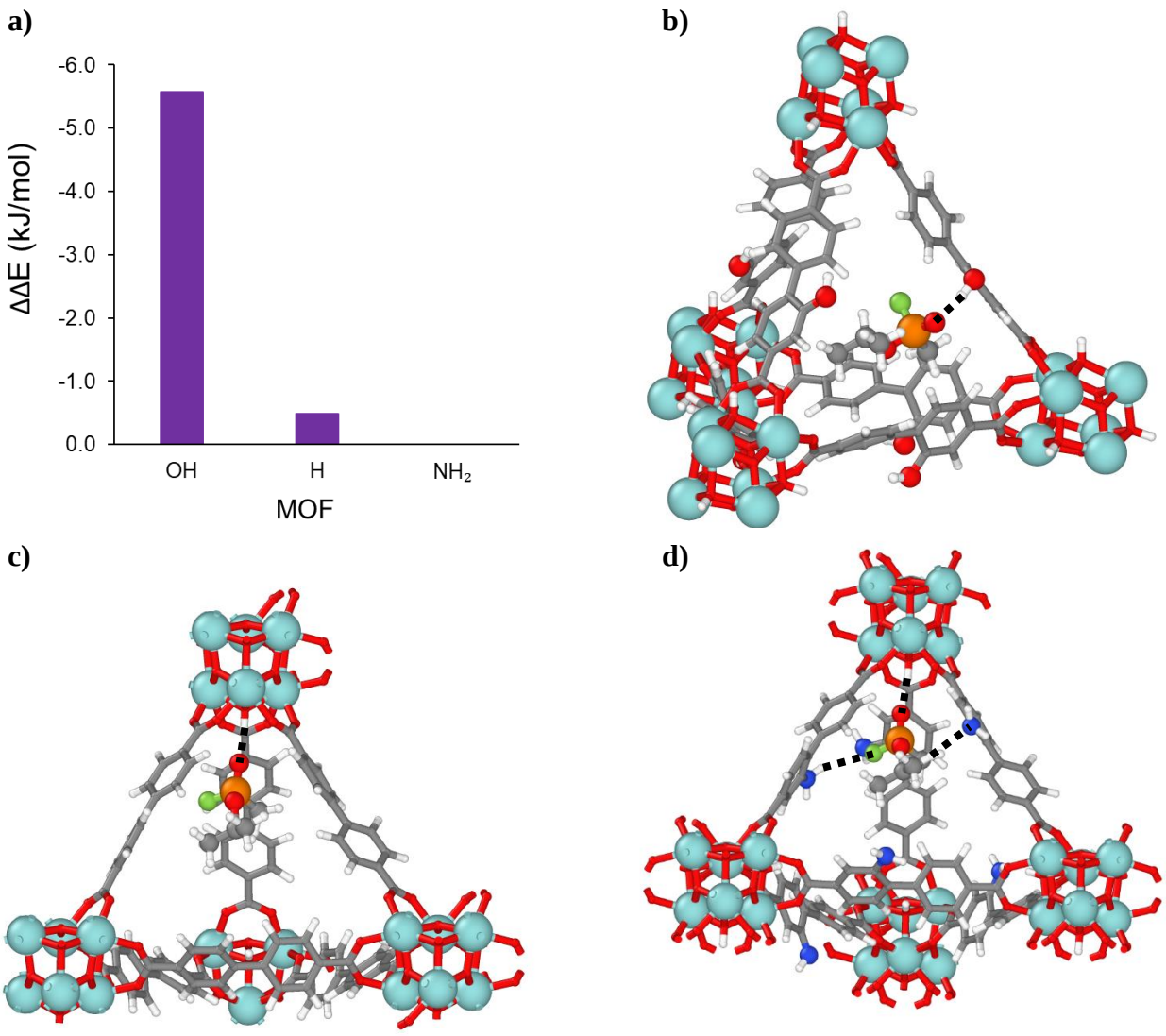

Figure 24. Binding energies and configurations of GB in UiO-67-X. a) Binding energies. b) GB in UiO-67-OH. c) GB in UiO-67. d) GB in UiO-67-NH_2. Zr is shown in teal, C in grey, O in red, H in white, F in olive, P in orange, and N in blue.

Table 7. Binding energies and binding energy differences for GB in the functionalized MOFs.

MOF	Energy (kJ/mol)	ΔΔEnergy (kJ/mol)
OH	-95.82	-5.58
H	-90.72	-0.48
NH_2	-90.24	0.00

The optimum binding configuration in the OH functionalized MOF is not the same as the NH_2 functionalized and unfunctionalized MOFs. However, the equivalent configuration has a binding energy of -92.9 kJ/mol and is included in Appendix Figure C1. The configuration shown in Figure 24b has an OH···O hydrogen bond length of 1.78 Å, while the configuration in Appendix Figure C1 has an OH···O hydrogen bond length of 2.05 Å.

The interaction shown in Figure 24b likely has the strongest energy of the three because it is able to form a strong hydrogen bond outside of the pocket environment where there is more open space, allowing for a reduction in repulsive interactions between analyte and ligands. This is also likely true for the comparison geometry shown in Appendix Figure C1, where there is also an OH – F electrostatic interaction of 3.25 Å resulting in similar energies.

The OH···O hydrogen bond in the UiO-67 configuration is 1.79 Å. The UiO-67-NH_2 configuration's hydrogen bonds are OH···O 2.05 Å and NH···F 3.05 Å, and there is a weak electrostatic interaction: CH···N 2.88 Å. The 0.25 Å difference in hydrogen bond length between GB and the μ_3-OH group indicates that the NH_2 groups are unnecessary to make a strong binding site. GB relaxes out of the pocket to interact with those groups, resulting in similar energies between the two configurations.

4.3.2 VX

Binding energy differences and configurations of VX in UiO-67-X are shown in Figure 25.

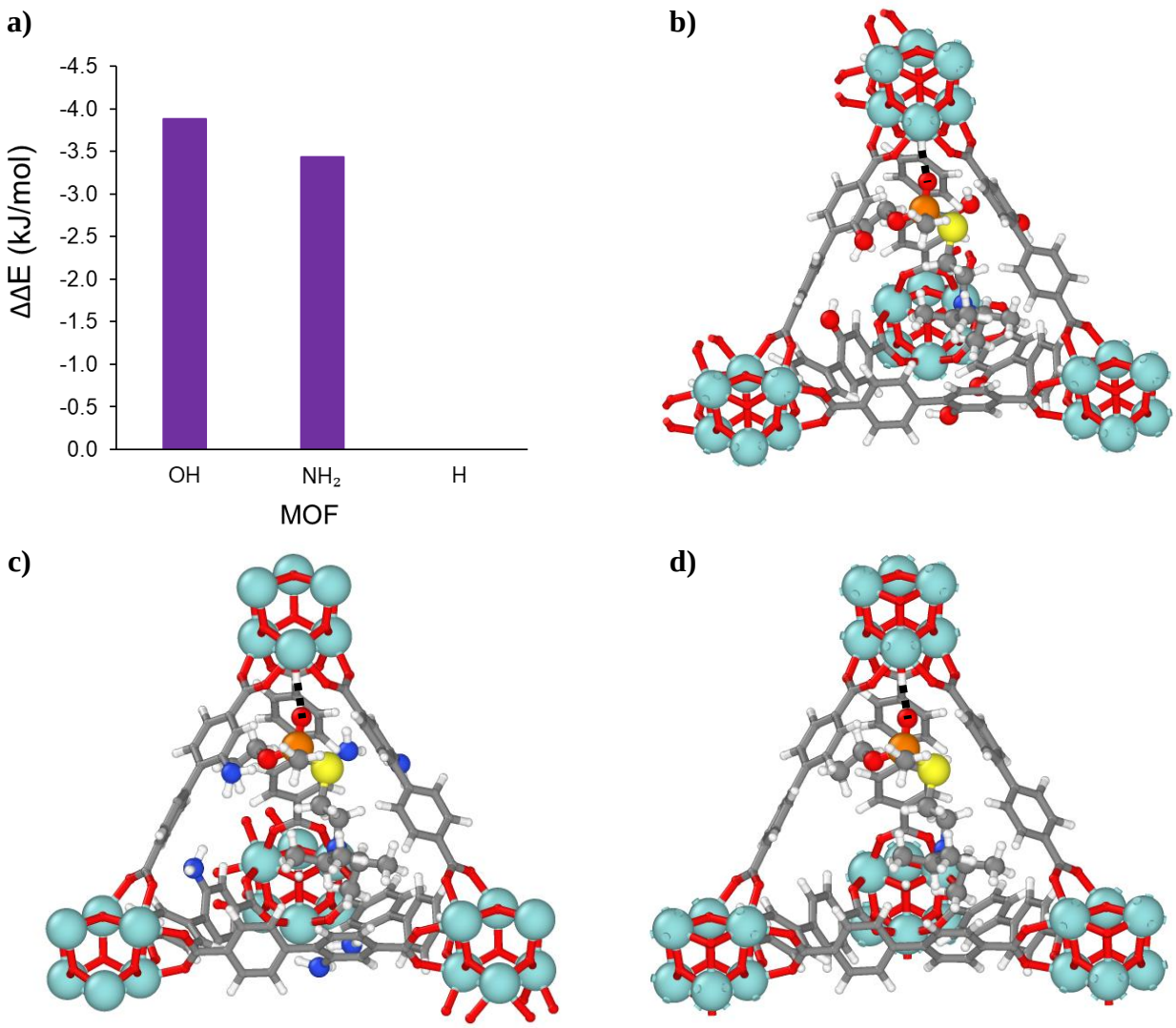

Figure 25. Binding energies and configurations of VX in UiO-67-X. a) Binding energies. b) VX in UiO-67-OH. c) VX in UiO-67-NH_2. d) VX in UiO-67. Zr is shown in teal, C in grey, O in red, H in white, S in yellow, P in orange, and N in blue.

All three of the MOFs have similar binding configurations with VX. The binding energies are all within 4 kJ/mol of each other as shown in Table 8.

Table 8. Binding energies and binding energy differences of VX in functionalized MOFs.

MOF	Energy (kJ/mol)	ΔΔEnergy (kJ/mol)
OH	-185.56	-3.88
NH_2	-185.12	-3.44
H	-181.68	0.00

There is a hydrogen bond between the phosphonyl oxygen and the H atom of the μ_3-OH group. The hydrogen bond length for all three structures is ~1.79 Å (values in Appendix Table C1). The similarity in binding energies and hydrogen bond lengths indicates that the functional groups do not have an effect on the binding strength in this system. VX in such a large molecule that the substituent groups may prevent any stronger interactions between the ligand functionalizations from forming with the core of the agent.

4.3.3 A-234

Binding energy differences and configurations of A-234 in UiO-67-X are shown in Figure 26.

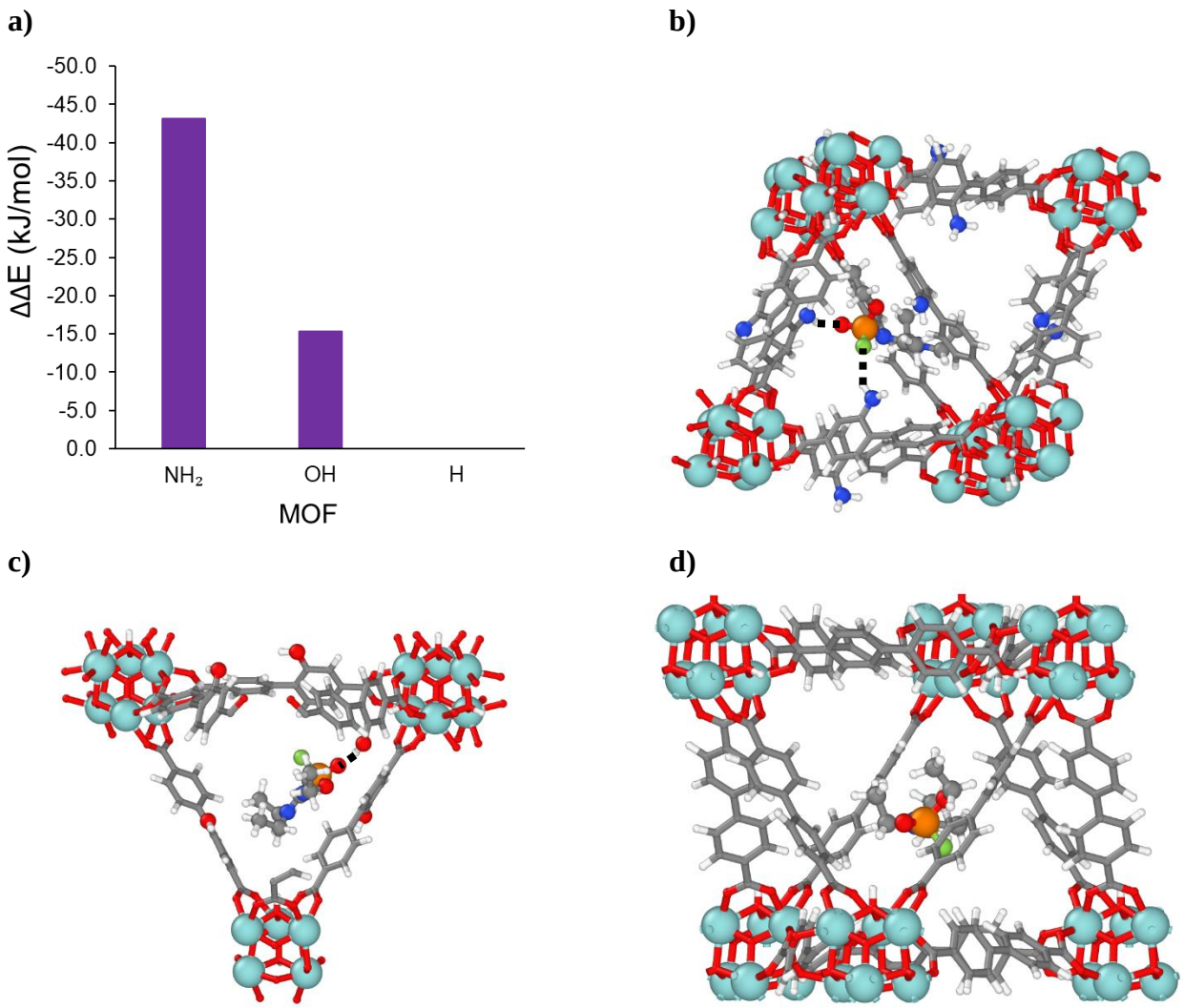

Figure 26. Binding energies and configurations of A-234 in UiO-67-X. a) Binding energy differences. b) A-234 in UiO-67-NH_2. c) A-234 in UiO-67-OH. d) A-234 in UiO-67. Zr is shown in teal, C in grey, O in red, H in white, F in olive, P in orange, and N in blue.

The strongest binding configurations in UiO-67-NH_2 and UiO-67 occur in the octahedral pore. The strongest binding configuration for UiO-67-OH occurs in the μ_3-OH tetrahedral pore. The corresponding binding energies are tabulated in Table 9.

Table 9. Binding energies and binding energy differences for A-234 in functionalized UiO-67.

MOF	Energy (kJ/mol)	ΔΔEnergy (kJ/mol)
NH_2	-147.32	-43.14
OH	-119.52	-15.34
H	-104.18	0.00

In UiO-67-NH_2, A-234 strongly interacts with two NH_2 functionalized ligands, shown in Figure 26b. The NH···O hydrogen bond is 1.98 Å, and the NH···F hydrogen bond is 2.53 Å. The OH functionalized MOF configuration is 28 kJ/mol weaker and has a 1.68 Å hydrogen bond between one ligand OH group and the phosphonyl oxygen. We evaluated the OH functionalized analogue of UiO-67-NH_2 + A-234 configuration shown in Figure 26b, and found the configuration shown in Appendix Figure C2. Here, the OH···O hydrogen bond is 1.83 Å, and the OH···F hydrogen bond is 2.65 Å. The binding energy is -75.6 kJ/mol. This is ~ 70 kJ/mol weaker than the corresponding configuration with UiO-67-NH_2. We evaluated the hydrogen bond angles, shown in Appendix Table C2, in an attempt to explain this energy discrepancy, and found that while the UiO-67-OH configuration has smaller angles, the differences are not substantial enough to explain the binding energy difference.

Comparing the binding energies of the three agents, those of VX are almost 100 kJ stronger than those of GB. This difference can be attributed to VX being a larger molecule with many more

opportunities for the formation of weak electrostatic interactions between the ligands and the analyte.

Comparing VX and A-234, structures were identified that featured the formation of a hydrogen bond between the phosphonyl oxygen of A-234 and the μ_3-OH group found in some tetrahedral pores. The strongest of these for UiO-67-NH_2 had a binding energy of -122 kJ/mol, and a hydrogen bond length of 2.06 Å, corresponding to a weaker energy by 63 kJ/mol and a hydrogen bond 0.27 Å longer than the corresponding VX in UiO-67-NH_2 structure. This configuration is shown in Appendix Figure C3. While the energy difference may be attributable to the additional weak electrostatic interactions possible between the larger VX molecule and the ligands, the difference in hydrogen bond length indicates that the greater steric bulk of A-234 may be preventing it from interacting with the μ_3-OH site as strongly.

4.4 Conclusions

We find no difference in the binding energies for different MOFs for either GB or VX. This is attributable to strongest binding site being located in the μ_3-OH containing tetrahedral pores. However, this is not the case for A-234, where the strongest binding sites are located in the octahedral pore. While there are local minima at the μ_3-OH site, stronger interactions occur through multiple ligand interactions in the octahedral pore, where there is more space for the steric bulk of A-234.

5.0 From "In-situ NMR Investigation of Molecular Adsorption and Kinetics in MOF UiO-66" (under review)

The primitive cell of pristine UiO-66 has three distinct pores: a tetrahedral pore containing 4 μ_3-OH groups, a tetrahedral pore containing 4 μ_3-O groups, and the octahedral pore. The lowest energy configurations of an IPA molecule in the three different pores of pristine UiO-66 was estimated from density functional theory (DFT) as implemented within CP2K 5.1.[55-57] Minimum energy structures were identified using a modified basin hopping technique described in our previous paper.[1] Goedecker-Teter-Hutter pseudopotentials[59] were used with the DZVP-MOLOPT-SR basis set,[60] and Grimme's D3 dispersion correction[50] was applied. The cutoff and relative cutoff values were 400 Ry and 50 Ry, respectively. Convergence of these parameters has been verified previously[1] for UiO-67, and we have successfully used these parameters with UiO-66. The conjugate gradient orbital transformation minimizer[134] and LBFGS optimizer[61] were used. Relaxation calculations were performed on the periodic UiO-66 primitive cell ($a = b = c = 14.83$ Å, $\alpha = \beta = \gamma = 60°$). The energy of IPA was calculated by relaxing an isolated molecule of IPA in a cubic box 25 Å on a side. All three pristine pore environments were studied independently. A single IPA molecule was placed into each of the three pores: the μ_3-OH tetrahedral pore, the μ_3-O containing pore, and the octahedral pore.

Ab initio molecular dynamics (AIMD) simulations in the canonical ensemble were carried out on each of the three periodic systems at a temperature of 1000 K using the GLE thermostat.[62-63] The AIMD simulations were run for 5 ps, using a time step of 0.5 fs. The coordinates of the AIMD simulations were saved every 100 timesteps and the sampled geometries were relaxed to their local minima. The resulting energies were then used to calculate binding energies defined as

$$\Delta E_{\text{bind}} = E_{\text{MOF}/A} - E_{\text{MOF}} - E_A \quad \textbf{(5-1)}$$

where $E_{\text{MOF}/A}$ is the energy of the MOF + IPA system, and E_{MOF}, E_A are energies of the empty MOF and IPA in the gas phase, respectively. The strongest binding configuration found was of IPA in the μ_3-OH tetrahedral pore, with a binding energy of -89.9 kJ/mol. This configuration, shown in Figure 27, was strongest due to the formation of a 1.77 Å hydrogen bond between the μ_3-OH hydrogen and the IPA oxygen. The strongest binding configurations found in the μ_3-O tetrahedral and octahedral pores are shown in Figure 28 and Figure 29, respectively. The energies of these configurations are -59.4 kJ/mol and -50.5 kJ/mol respectively. These energies and relative binding energies are summarized in Table 10. The binding modes are likely dominated by electrostatic interactions.

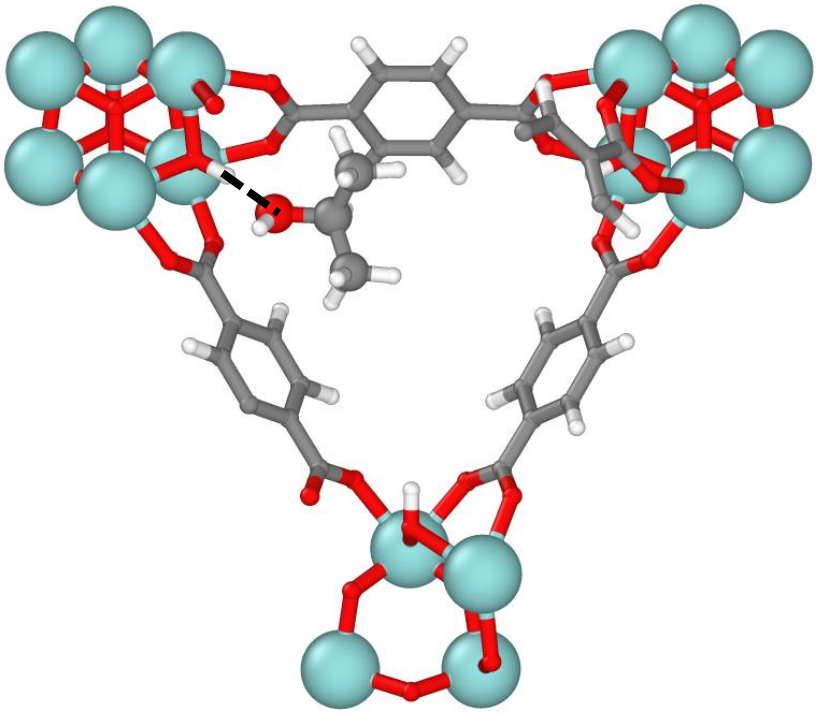

Figure 27. Configuration of local minima with the strongest binding energy for IPA in the μ_3-OH tetrahedral pore of UiO-66. The hydrogen bond between the μ_3-OH and the ketone oxygen is shown by the black dashed line. Atoms are as follows: White: H, gray: C, red: O, cyan, Zr. Created with OVITO.[188]

Table 10. Binding energies and relative binding energies of IPA in the three distinct pores of UiO-66.

$$\Delta\Delta E_{\mathbf{bind},i} = \Delta E_{\mathbf{bind},i} - \min\left(\Delta E_{\mathbf{bind},i}\right)$$

Pore	$\Delta E_{\mathbf{bind}}$ (kJ/mol)	$\Delta\Delta E_{\mathbf{bind}}$ (kJ/mol)
Tetrahedral with μ_3-OH	-89.9	0
Tetrahedral with μ_3-O	-59.4	30.5
Octahedral	-50.5	39.4

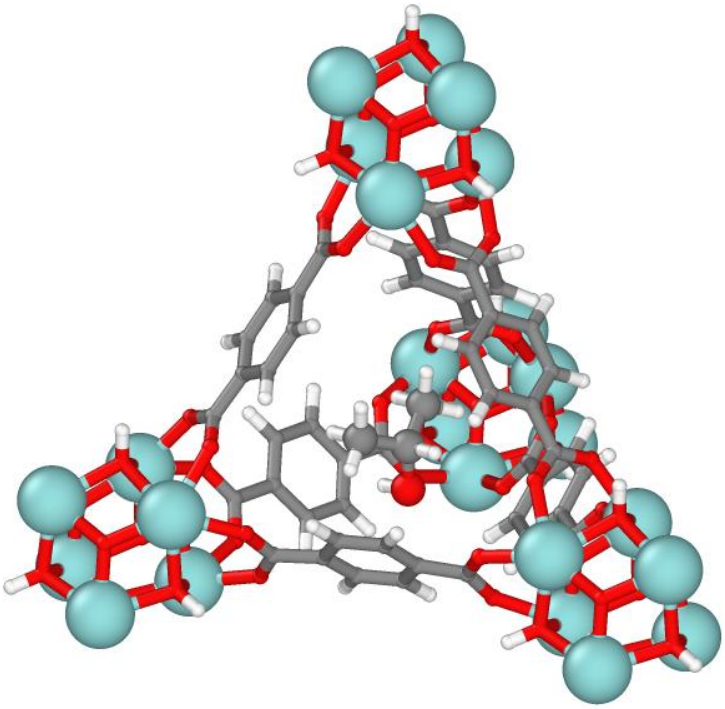

Figure 28. Configuration of local minima with the strongest binding energy for IPA in the μ_3-O tetrahedral pore of UiO-66. Atoms are as follows: White: H, gray: C, red: O, cyan, Zr. Created with OVITO.[188]

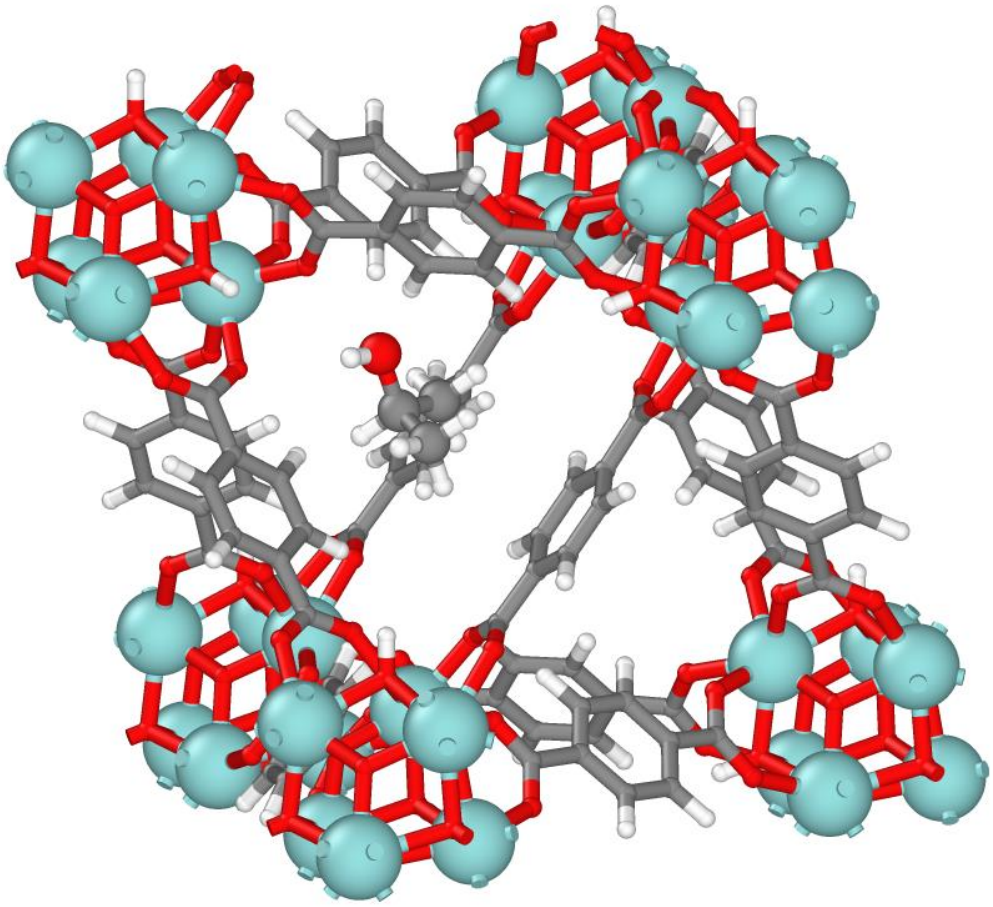

Figure 29. Configuration of local minima with the strongest binding energy for IPA in the octahedral pore of UiO-66. Atoms are as follows: White: H, gray: C, red: O, cyan, Zr. Created with OVITO.[188]

6.0 Publications

This chapter contains a list of all publications, published, submitted, and planned, to which I contributed along with a list of those contributions.

1. Li, L., Zhang, S., Ruffley, J. P., & Johnson, J. K. (2018). Energy Efficient Formaldehyde Synthesis by Direct Hydrogenation of Carbon Monoxide in Functionalized Metal–Organic Frameworks. *ACS Sustainable Chemistry & Engineering, 7*(2), 2508-2515. doi:10.1021/acssuschemeng.8b05413
    a. Isotherm calculations of H_2 and CO in UiO-67-NBF_2
    b. UiO-67-NBF_2 graphic
    c. Wrote part of the experimental methodology and revised manuscript.

2. Mohamed, M. H., Yang, Y., Li, L., Zhang, S., Ruffley, J. P., Jarvi, A. G., . . . Rosi, N. L. (2019). Designing Open Metal Sites in Metal–Organic Frameworks for Paraffin/Olefin Separations. *Journal of the American Chemical Society, 141*(33), 13003-13007. doi:10.1021/jacs.9b06582
    a. Isotherm calculations of N_2 in Cu(I)-MFU-4*l* and Zn(II)-MFU-4*l*
    b. MOF surface area calculations
    c. Blocked pore estimations
    d. Contributions to supporting information methodology

3. Ruffley, J. P., Goodenough, I., Luo, T.-Y., Richard, M., Borguet, E., Rosi, N. L., & Johnson, J. K. (2019). Design, Synthesis, and Characterization of Metal–Organic Frameworks for Enhanced Sorption of Chemical Warfare Agent Simulants. *The Journal of Physical Chemistry C, 123*(32), 19748-19758. doi:10.1021/acs.jpcc.9b05574
    a. Cluster and crystal density functional theory calculations
    b. Proposed 6 novel MOFs. CAS numbers: 2376615-42-6, 2376615-43-7, 2376615-45-9, 2374313-47-8, 2376447-74-2, 2376447-75-3

c. Developed classical DMMP potential

d. Isotherm calculations of DMMP in UiO-67-NH_2, UiO-67-CH_3, UiO-67

e. Isotherm calculations of N_2 in UiO-67-NH_2, UiO-67-CH_3, UiO-67

f. Surface area calculations for UiO-67-NH_2, UiO-67-CH_3, UiO-67

g. Lead writer

4. Vo, M. N., Ruffley, J. P., Johnson, J. K., (2021) Impact of Defects on the Decomposition of Chemical Warfare Agent Simulants in Zr-based Metal Organic Frameworks *AIChE Journal* 2021;e17156.
    a. Optimized periodic MOF geometries

    b. Writing and revisions

5. Wardzala, J.J., Ruffley, J. P., Bagusetty, A., Goodenough, I., Schmidt, A. M., Shukla, P. B., DeSouza, M., Das, P., Wei, X., Thompson, D. J., Karwacki, C. J., Wilmer, C. E., Borguet, E., Rosi, N. L., Johnson, J. K., Modeling of Diffusion of Acetone in UiO-66. *The Journal of Physical Chemistry C* 2020, 124, 52, 28469–28478
    a. Literature review

    b. Created molecular dynamics simulation input files

    c. Wrote bulk job submission scripts

    d. Wrote analysis scripts

    e. Developed method to dynamically insert acetone molecules into MOF pores

    f. Density functional theory binding energy calculations of acetone in UiO-66

    g. Intellectual contributions: Method to identify pore window behavior during acetone transit

    h. Supervision of undergraduate students

    i. Lead writer

6. An, Y., Kleinhammes, A., Doyle, P., Chen, E-Y., Song, Y., Morris, A. J., Gibbons, B., Cai, M., Johnson, J. K., Shukla, P. B., Vo, M. N., Wei, X., Wilmer, C. E., Ruffley, J. P., Huang, L., Tovar, T. M., Mahle, J. J., Karwacki, C. J., Wu, Y. In-situ NMR Investigation of Molecular Adsorption and Kinetics in MOF UiO-66. *The Journal of Physical Chemistry Letters* (under review)

    a. Density functional theory calculations of IPA in UiO-66

    b. Writing

7. Harper, D. K., Klan, J. M., Ruffley, J. P., Gan, X-Y., Millstone, J. E., Johnson, J. K., A Theoretical Study of the Impact of Vacancies and Disorder on the Electronic Properties of $Cu_{2-x}Se$, *The Journal of Physical Chemistry C* (to be submitted)

    a. Literature review

    b. Writing

    c. Supervision of undergraduate students

8. Ruffley, J. P, Johnson, J. K., Interaction of HD and 2-Chloroethyl Ethyl Sulfide with a Series of Functionalized UiO-67 MOFs. *The Journal of Physical Chemistry C* (to be submitted)
    a. Project idea

    b. Density functional theory binding energy calculations on 2-CEES, HD in 10 UiO-67 MOFs

    c. Density functional theory strain calculations

    d. Writing

9. Ruffley, J. P., Johnson, J. K., Interaction of GB, VX, and A-234 with Pristine Functionalized UiO-67-X Metal-Organic Frameworks *The Journal of Physical Chemistry C* (to be submitted)
    a. Project idea

    b. Density functional theory calculations on GB, VX, A-234 in UiO-67-NH_2, UiO-67-OH, UiO-67

    c. Writing

7.0 Future Work

One next step for this work would be to develop robust classical potentials for the blister and nerve agents studied here. A major limitation of chemical warfare agent (CWA) research is the lack of such potentials, limiting computational studies to ab initio approaches. While potentials have been reported for GB and GD,[64], we were unable to reproduce that literature account during my PhD, and have had discussions with other scientists who also could not reproduce that account. While ab initio methods can be used to study reactivity, they preclude calculation of properties such as diffusion and adsorption, both of which would greatly advance our ability to identify materials for CWA capture.

Another important contribution to this work would be to understand the interface of plasmonic nanoparticles encapsulated in MOFs through simulations. This might influence nanoparticle and MOF design to enhance potential reactivity.

MOFs must also be designed to allow for reaction products to diffuse out. If such products sorb more strongly to the MOFs than agents of interest, the material will be ineffective. In conjunction with this work, studies must be undertaken which consider the interactions between agents and degradation products when both are in a MOF. As agent concentrates in the MOF, interactions between multiple agent molecules will occur. The effects of such interactions on the efficacy of the MOF materials must also be evaluated.

Appendix A Additional Figures and Tables for Chapter 1

Appendix Table A1. Convergence criteria for ORCA geometry optimizations. G is the gradient and D is displacement.

type	tolerance
E	5×10^{-6} Eh
RMSG	1×10^{-4} Eh/bohr
Max G	3×10^{-4} Eh/bohr
RMSD	2×10^{-3} bohr
Max D	4×10^{-3} bohr

Appendix Table A2. Gaussian 09 cluster binding energies between DMMP and ligand models for UiO-67, with counterpoise corrected energies. While the counterpoise correction energies result in substantial error of over 50% for the weakest binding energies, applying the correction does not change the relative order of binding strength.

Interaction Pair	ΔE_{bind} (kJ/mol)	E_{CP} (kJ/mol)	$\Delta E_{bind,CP}$ (kJ/mol)
DMMP + aniline	-25.33	3.19	-22.14
DMMP + thiophenol	-20.74	3.25	-17.49
DMMP + nitrobenzene	-17.88	3.57	-14.31
DMMP + bromobenzene	-11.31	2.60	-8.71
DMMP + toluene	-10.70	2.84	-7.86
DMMP + chlorobenzene	-9.80	2.80	-7.00
DMMP + phenyl azide	-8.32	2.96	-5.36
DMMP + benzene	-6.36	2.50	-3.85

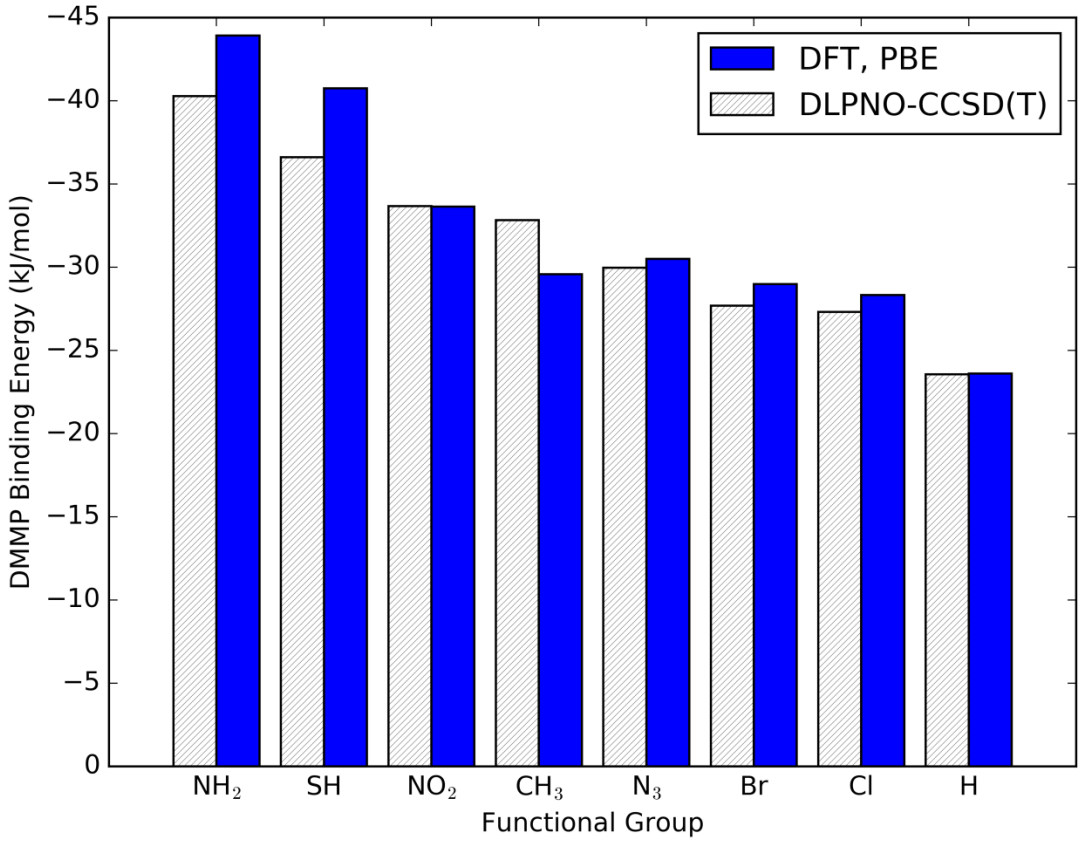

Appendix Figure A1. Binding energies calculated between DMMP and functional groups using DFT with the PBE functional and DLPNO-CCSD(T). Orca[46] was used for all calculations. The only change in the relative binding strength is the N_3 functionalized ligand. However, the energies in question differ by less than 1 kJ/mol, making this change in relative binding strength inconsequential.

Primitive cell optimizations, done with CP2K 4.1,[55-57] required selection of both cutoff and relative cutoff at converged values. Convergence was defined as no change in the single point energy to 1×10^{-5} hartree. Converged values were 400 rydberg cutoff and 50 rydberg relative cutoff.

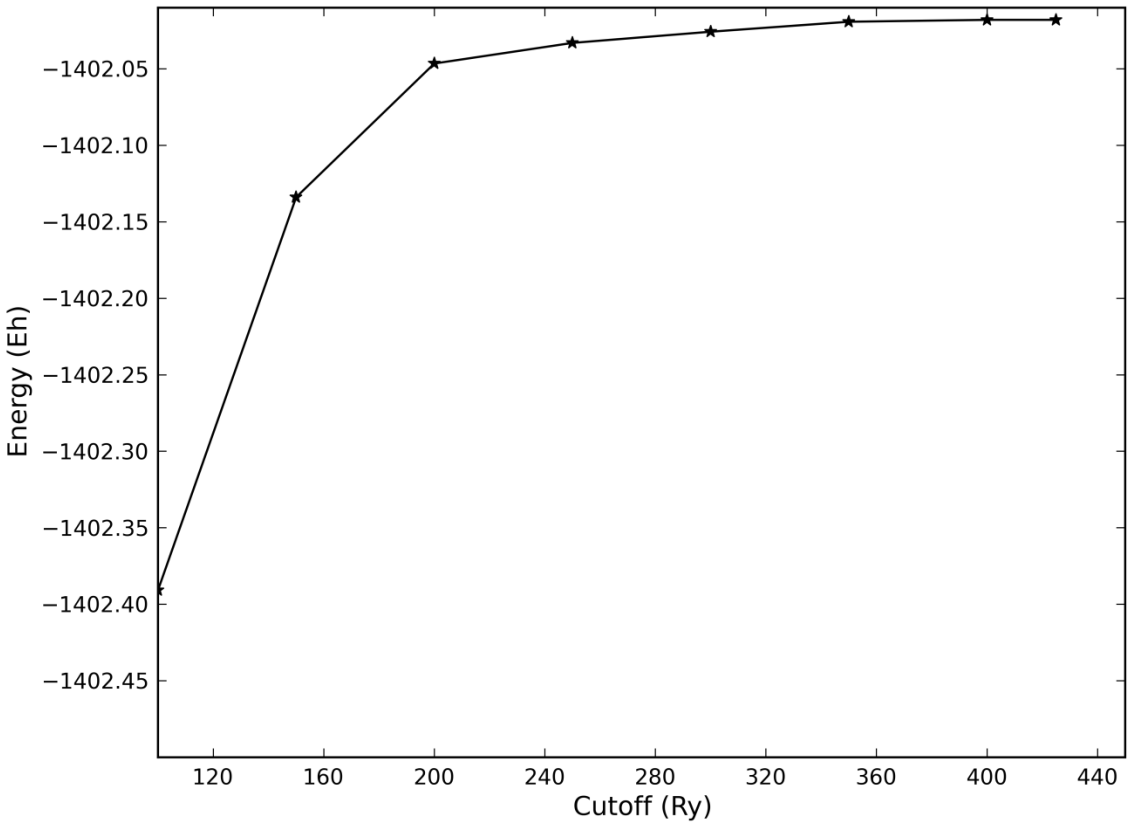

Appendix Figure A2. Convergence of the cutoff for UiO-67 using CP2K.

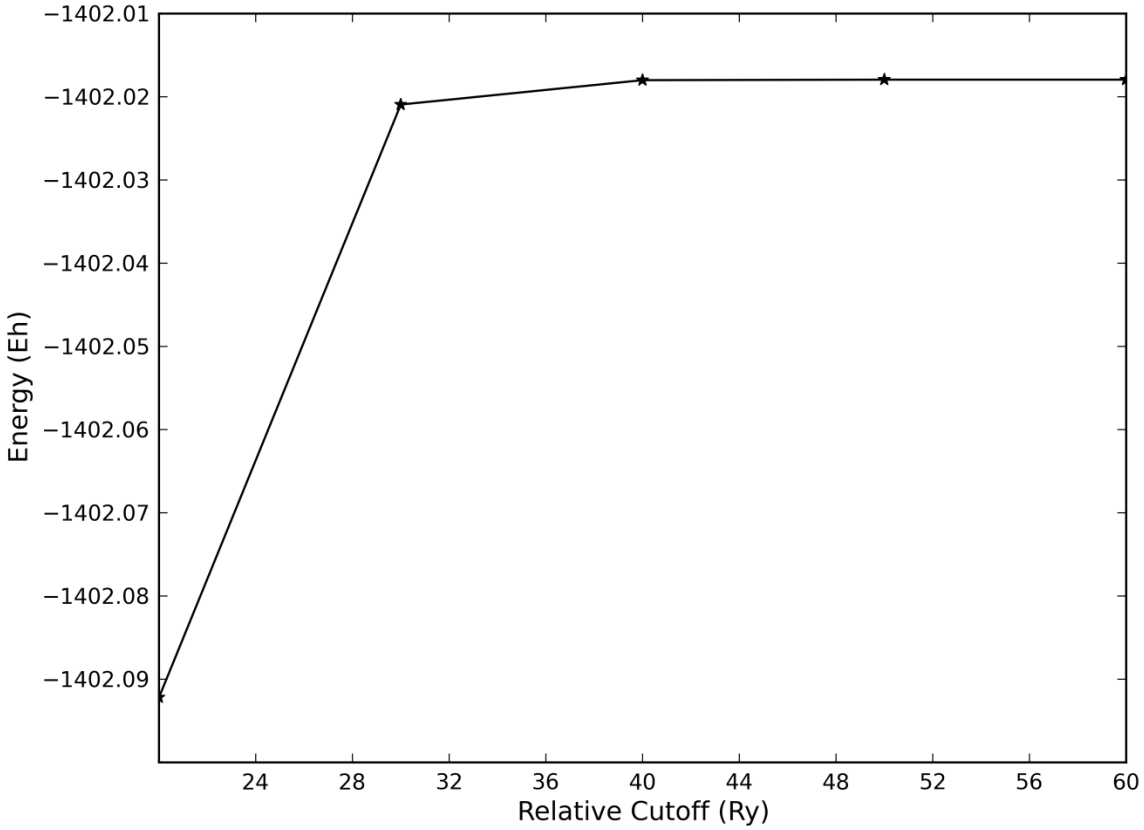

Appendix Figure A3. Convergence of the relative cutoff for UiO-67 using CP2K.

The united atom DMMP potential was described by eq (A-1), where the bond contribution was determined by eq (A-2), the angle contribution was determined by eq (A-3), and the dihedral torsion contribution was determined by eq (A-4).

$$V = V_{bond} + V_{bend} + V_{torsion} \quad \textbf{(A-1)}$$

$$V_{bond} = \frac{1}{2} K_r (r - r_0)^2 \quad \textbf{(A-2)}$$

$$V_{angle} = \frac{1}{2} K_\theta (\theta - \theta_0)^2 \quad \textbf{(A-3)}$$

$$V_{torsion} = K_\varphi [1 + \cos\{\mathrm{m}(\varphi - \varphi_0)\}] \quad \textbf{(A-4)}$$

QuickFF[66] parameters were generated using standard accuracy and output from a VASP[189-192] vibrational calculation.

It is expected that the bonded potential terms will be widely applicable for force-field based simulations of DMMP, as QuickFF has been shown to be robust and generally applicable to a variety of molecules.[66] While the Lennard-Jones and electrostatic parameters developed here were not tested over a range of states for accuracy, the goal of this work is not to develop such a widely robust model. Rather, the intention is to produce a model that will give a reasonable prediction of the behavior of DMMP. Here, a density of 1143 kg/m^3 at 298 K and 1 atm is obtained, while the literature value at these conditions is 1145 kg/m^3.

Appendix Table A3. Simulation parameters for LAMMPS NPT to fit an atomic potential for DMMP.

cutoff	14 Å
molecules	155
equilibration steps	100,000
production steps	500,000
timestep	0.25 fs

Appendix Table A4. Simulation parameters for RASPA NPT to fit an atomic potential for DMMP.

cutoff	14 Å
molecules	155
equilibration cycles	100,000
production cycles	300,000

Appendix Table A5. Lennard-Jones 12-6 potential parameters and atomic charges used to calculate non-bonded contributions to the potential for the DMMP molecule.

atom	ε (kcal/mol)	σ (Å)	q (e)
CH_3(-O)	0.169	3.75	0.135
CH_3(-P)	0.169	3.75	0.021
O	0.095	2.80	-0.360
O(=P)	0.137	3.05	-0.691
P	0.149	4.00	1.120

Appendix Table A6. Bond stretch parameters for the DMMP molecule. Parameters were used with eq (A-2) to calculate the bond stretch contribution to the potential.

bond	K_r (kcal/(mol*Å^2))	r_0 (Å)
CH_3 - O	682.44	1.469
CH_3 - P	444.2	1.801
O - P	684.62	1.633
O = P	1335.98	1.47

Appendix Table A7. Bending parameters for the DMMP molecule. Parameters were used with eq (A-3) to calculate the angle contribution to the potential.

angle	K_θ (kcal/(mol*rad^2))	θ_0 (degree)
CH_3 - O - P	56.451	111.13
CH_3 - P - O	87.035	101.9
CH_3 - P = O	71.5	118.7
O - P - O	88.928	106.08
O - P = O	77.731	113.55

Appendix Table A8. Dihedral torsion parameters for the DMMP molecule. Parameters were used with eq (A-4) to calculate the dihedral torsion contribution to the potential.

torsion	Kφ (kcal/mol)	m	φ_0 (degree)
CH_3 - O - P - CH_3	0.7192	3	0
CH_3 - O - P - O	0.0809	3	0
CH_3 - O - P = O	0.6096	3	0

Appendix Table A9. Helium void fractions calculated for each MOF were used to calculate excess adsorption isotherms in RASPA.

MOF	He void fraction
UiO-67	0.6793
UiO-67-NH_2	0.6429
UiO-67-CH_3	0.6289

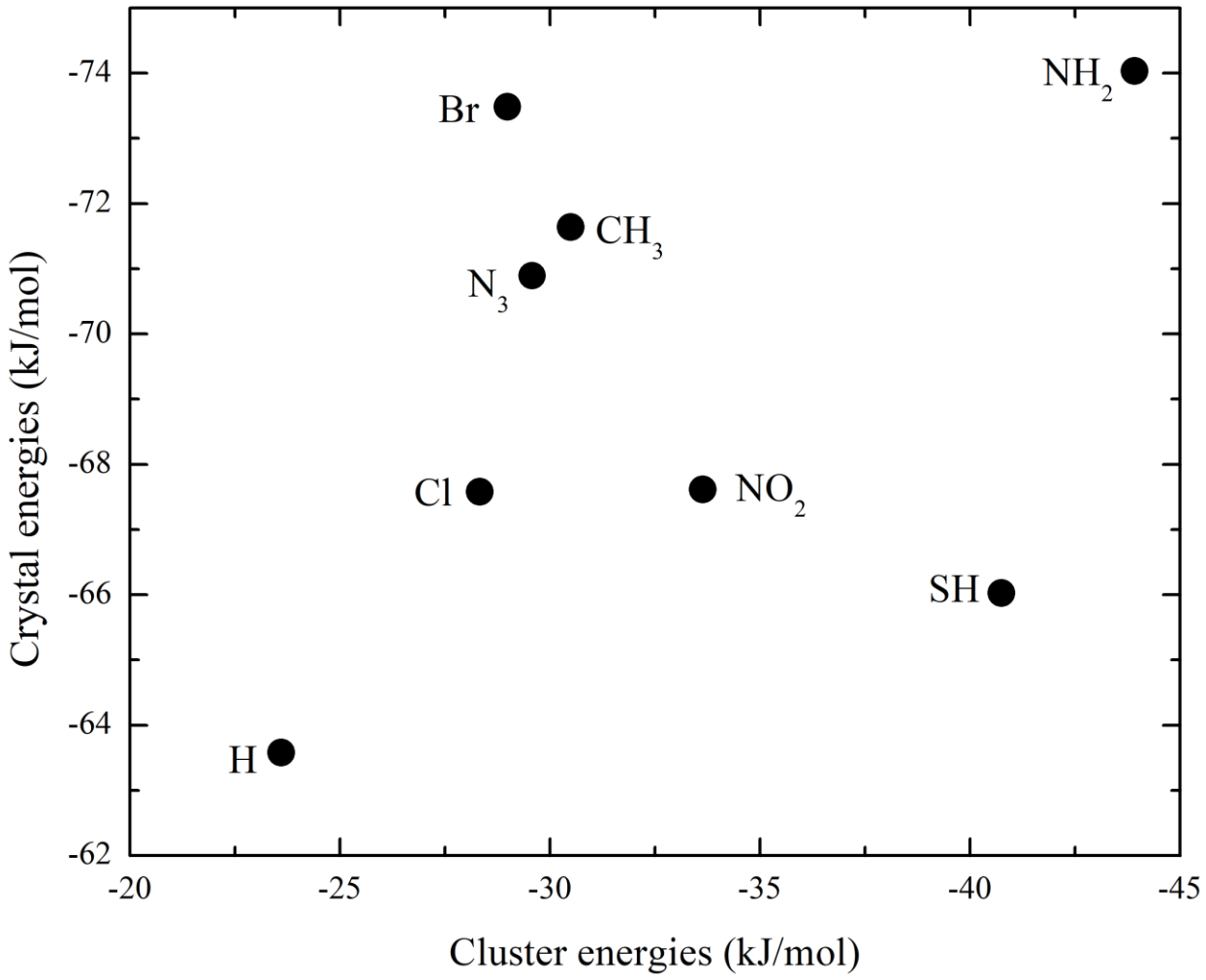

Appendix Figure A4. Comparison of cluster and crystal binding energies between DMMP and functionalized MOFs, as calculated from Orca and CP2K respectively. Only the strongest binding energy is shown.

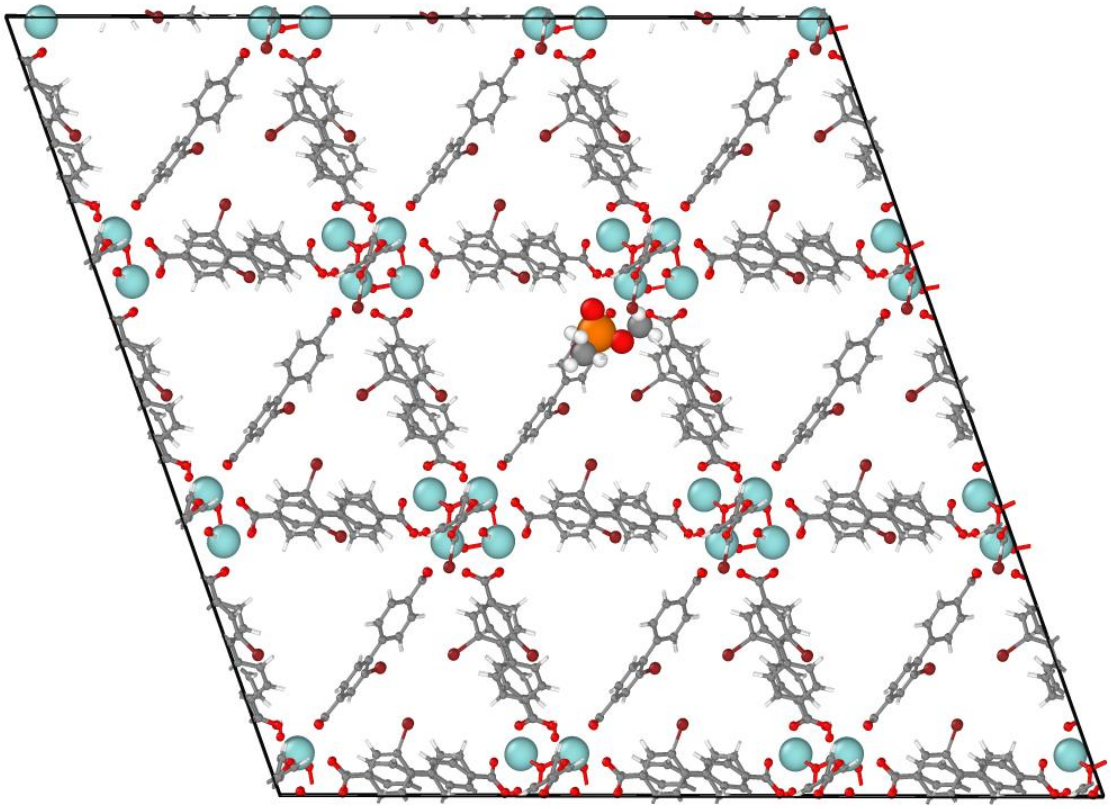

Appendix Figure A5. UiO-67-Br interaction with DMMP. Zr shown in light blue, oxygen shown in red, carbon shown in gray, bromine shown in burgundy, hydrogen shown in white.

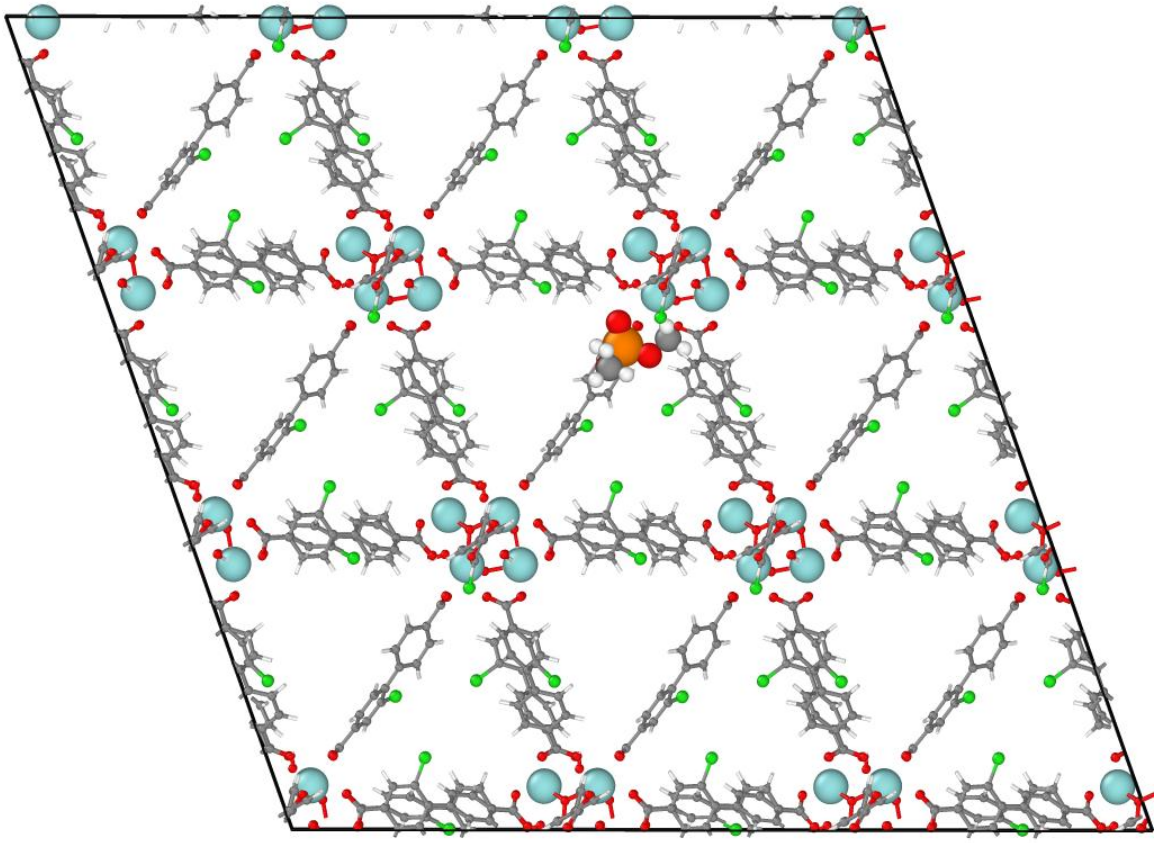

Appendix Figure A6. UiO-67-Cl interaction with DMMP. Zr shown in light blue, oxygen shown in red, carbon shown in gray, chlorine shown in lime green, hydrogen shown in white.

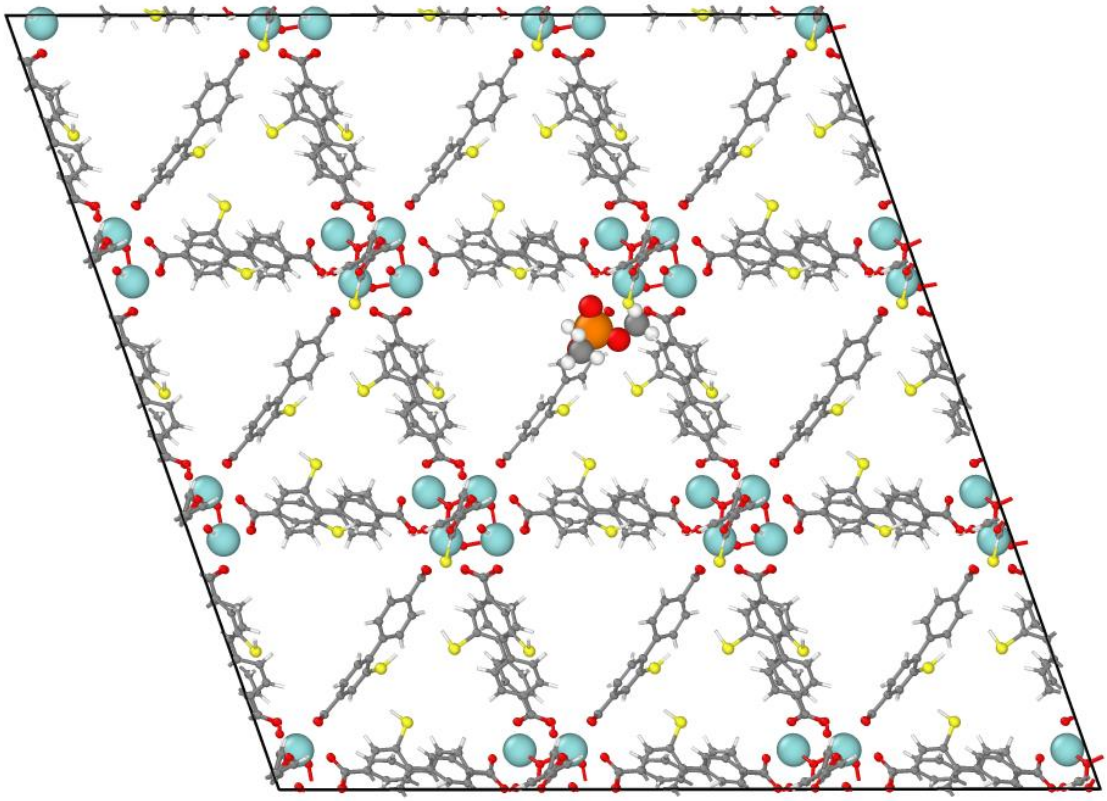

Appendix Figure A7. UiO-67-SH interaction with DMMP. Zr shown in light blue, oxygen shown in red, carbon shown in gray, sulfur shown in yellow, hydrogen shown in white.

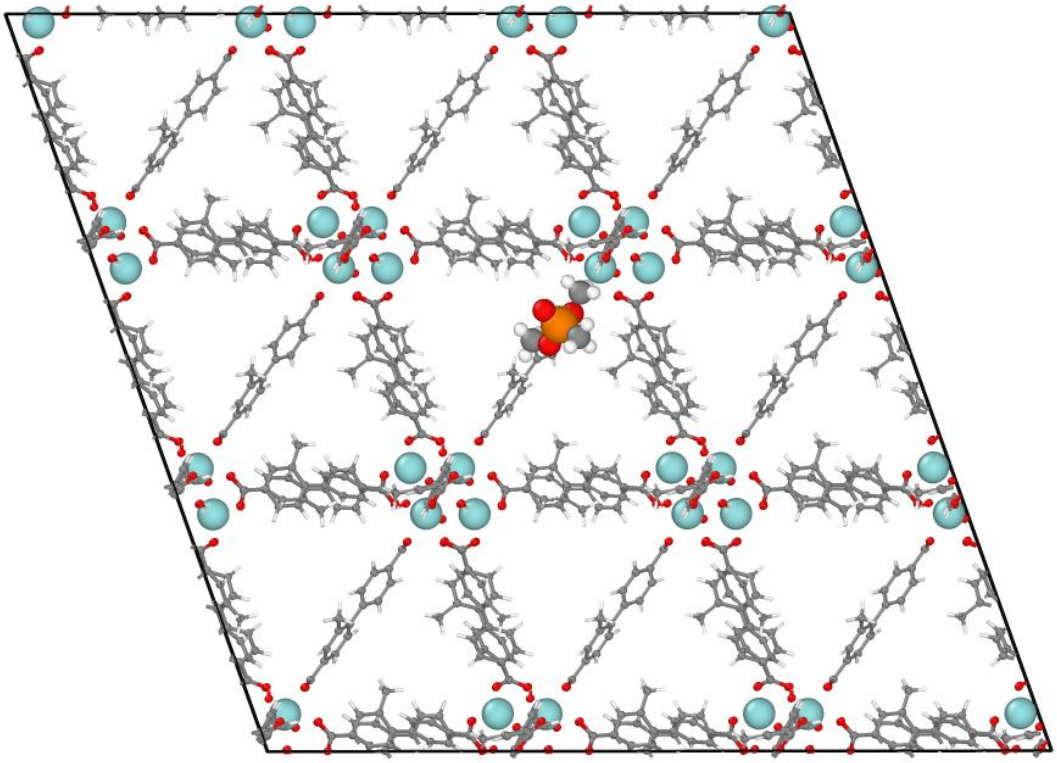

Appendix Figure A8. UiO-67-CH_3 interaction with DMMP. Zr shown in light blue, oxygen shown in red, carbon shown in gray, hydrogen shown in white.

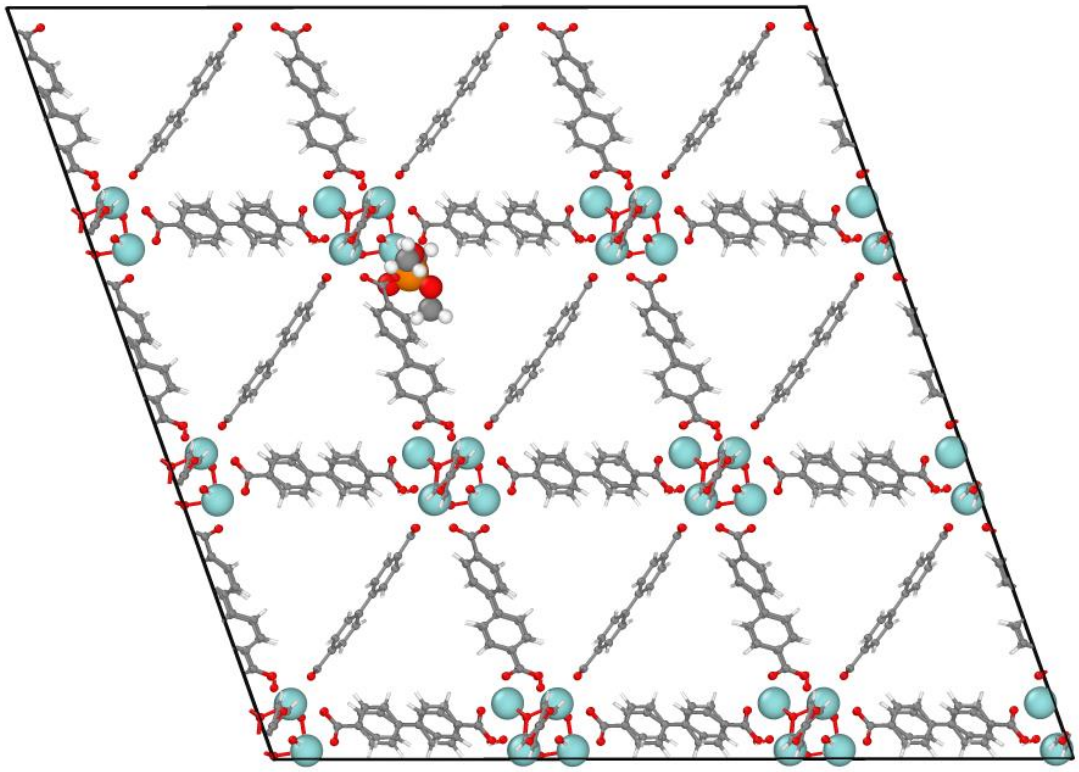

Appendix Figure A9. UiO-67 interaction with DMMP. Zr shown in light blue, oxygen shown in red, carbon shown in gray, hydrogen shown in white.

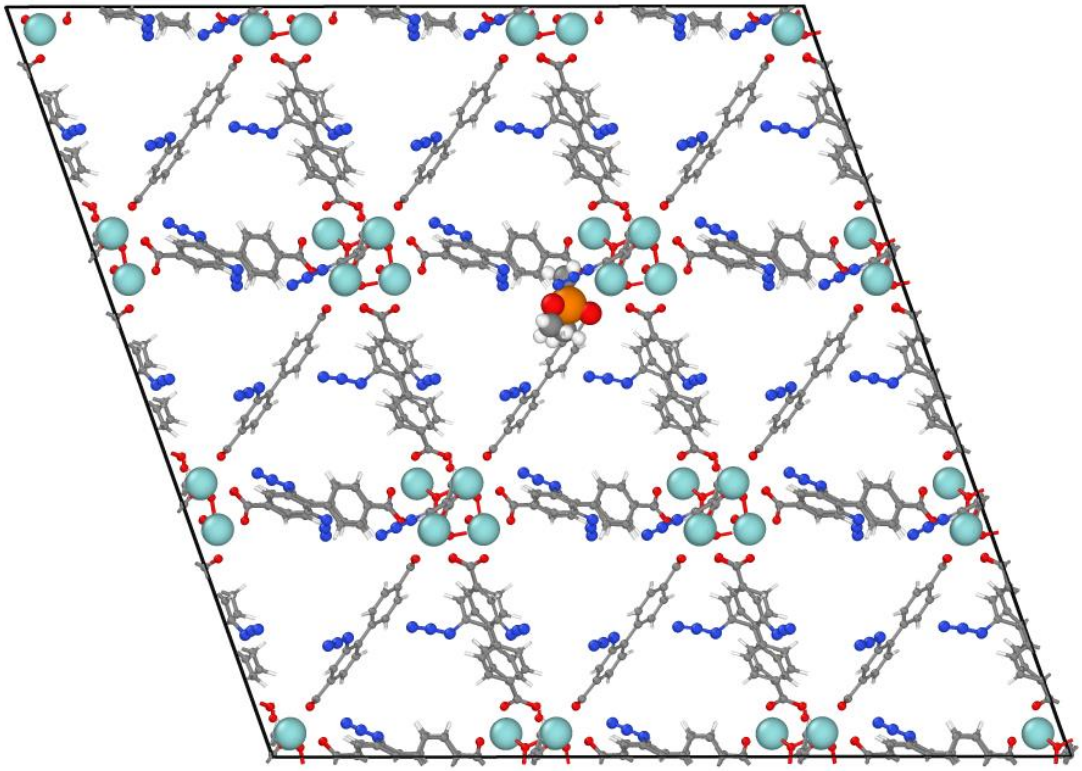

Appendix Figure A10. UiO-67-N_3 interaction with DMMP. Zr shown in light blue, oxygen shown in red, carbon shown in gray, nitrogen shown in blue, hydrogen shown in white.

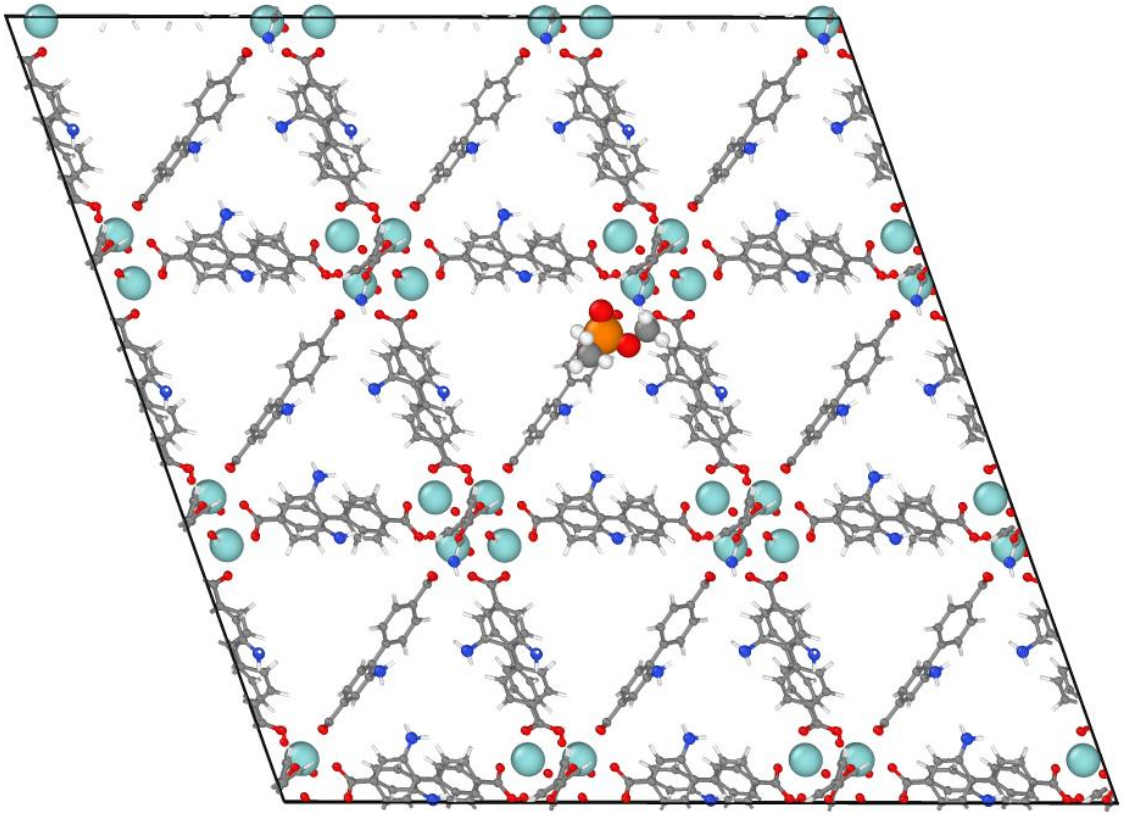

Appendix Figure A11. UiO-67-NH_2 interaction with DMMP. Zr shown in light blue, oxygen shown in red, carbon shown in gray, nitrogen shown in blue, hydrogen shown in white.

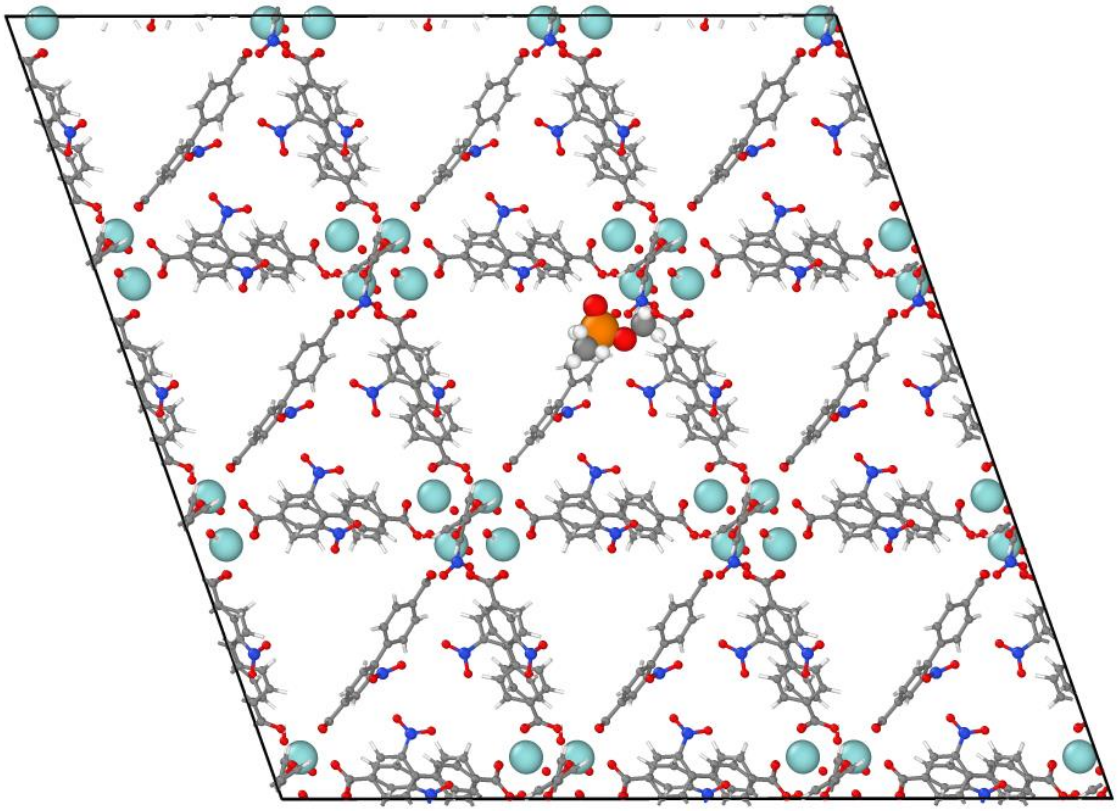

Appendix Figure A12. UiO-67-NO_2 interaction with DMMP. Zr shown in light blue, oxygen shown in red, carbon shown in gray, nitrogen shown in blue, hydrogen shown in white.

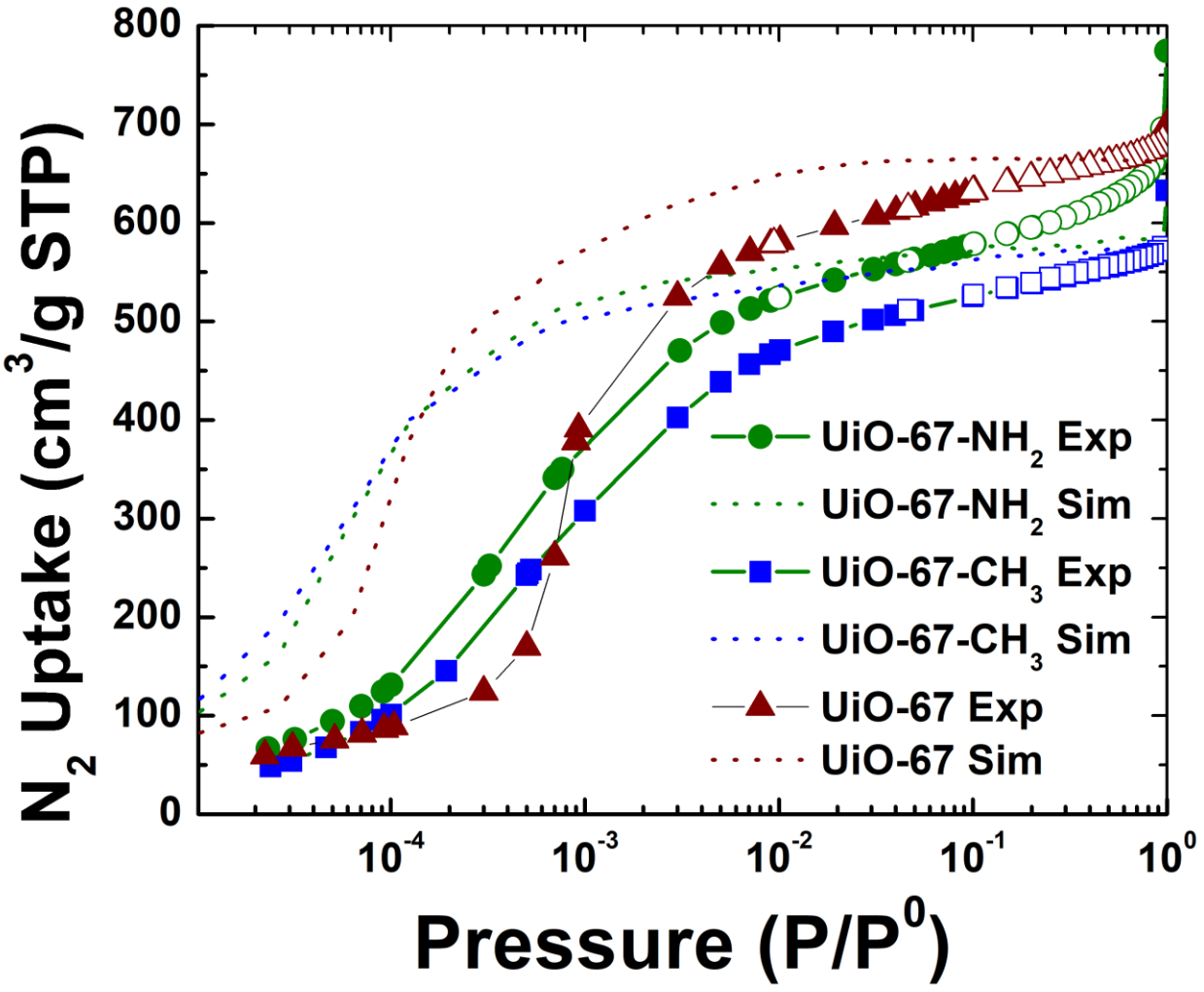

Appendix Figure A13. Nitrogen adsorption isotherms at 77 K from experiments (points) and simulations (lines). The model is too attractive at low to moderate pressures, but it correctly captures the behavior of the isotherms. There is no hysteresis in the experimental isotherms, as seen from agreement between adsorption (filled symbols) and desorption (open symbols). The model gives reasonable agreement at saturation.

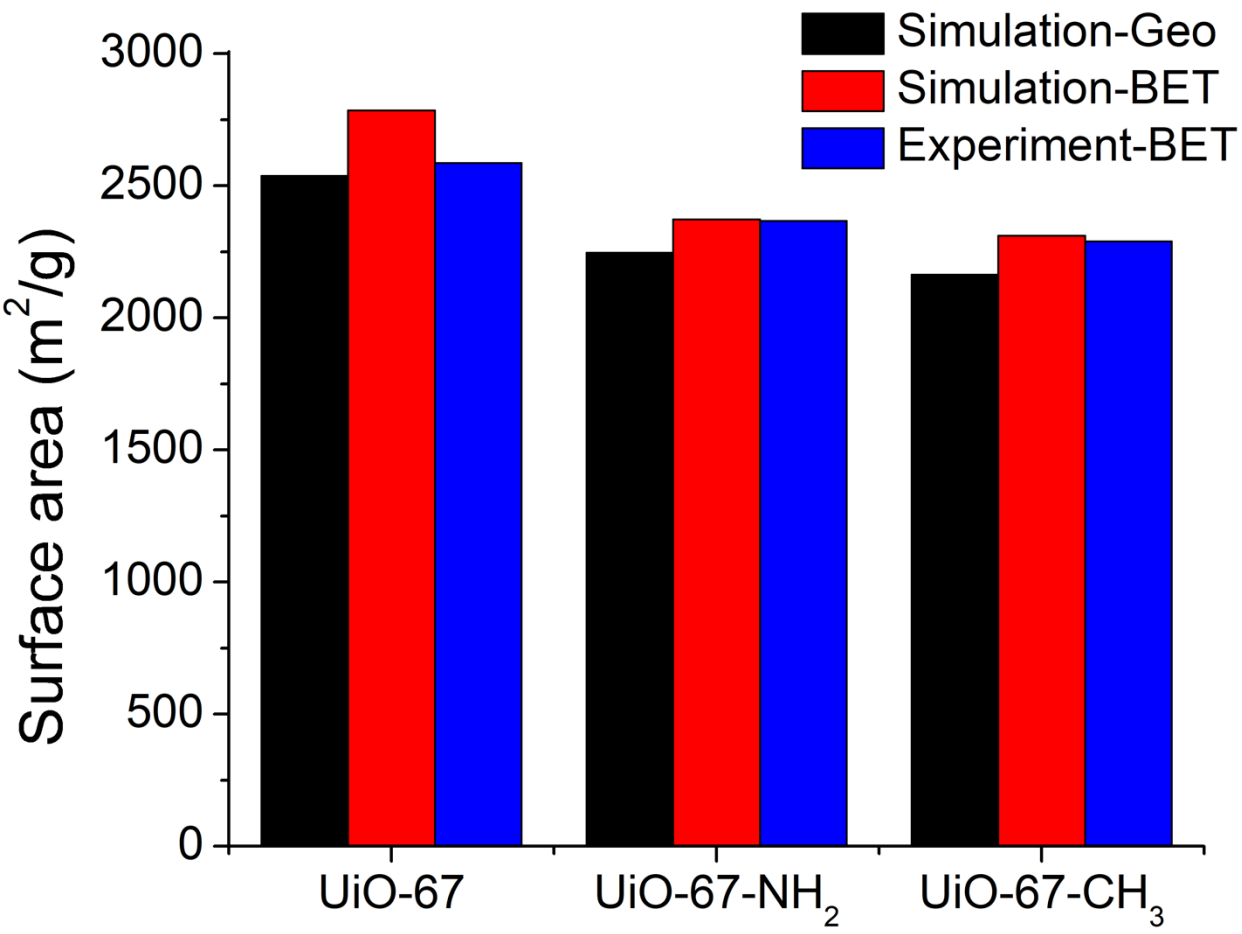

Appendix Figure A14. Surface areas for the synthesized MOFs computed from simulations and from experimental BET measurements based on N_2 isotherms at 77 K. The data shown as black bars were computed from a geometric algorithm involving rolling an argon atom over the surface of the MOF. The data shown as red bars were computed from applying the BET equation to simulated N_2 isotherms at 77 K (Appendix Figure A13). The blue bars represent BET surface areas from experimental N_2 isotherms at 77 K (Appendix Figure A13). The slight difference in geometric and BET surface areas is to be expected from different definitions of the surface area. Overall, the agreement is very good between the experiments and simulations.

The results of statistical analysis tabulated in Appendix Table A10 through Appendix Table A12 show that the models of adsorption for each MOF significantly differed from the mean. This is only one way of conducting a statistical analysis for non-linear models. Another way to examine the data for significant differences is by conducting an equivalence test, which directly compares the models to each other. Here, UiO-67-CH_3 was selected to be the reference model. For both analysis methods, α was set at 0.05. The results of this analysis are tabulated in Appendix Table A13 and Appendix Table A14. That a significant result is observed in this analysis as well cements the assertion that there is a significant difference in DMMP adsorption based on the model developed here.

Appendix Table A10. Analysis of means found that the growth rate term of the models was significantly different from the mean for the methyl and unfunctionalized MOFs.

level	lower limit	estimate	upper limit	limit exceeded
UiO-67	1648	2705	2384	upper
UiO-67-CH_3	1783	1695	2249	lower
UiO-67-NH_2	1775	2064	2257	

Appendix Table A11. Analysis of means found that the inflection points of the models were significantly different from the mean for all three of the models.

level	lower limit	estimate	upper limit	limit exceeded
UiO-67	0.002516	0.003635	0.002762	upper
UiO-67-CH_3	0.002529	0.002892	0.002749	upper
UiO-67-NH_2	0.002575	0.002283	0.002703	lower

Appendix Table A12. Analysis of means found that the asymptotes of the models were significantly different from the mean for all three models.

level	lower limit	estimate	upper limit	limit exceeded
UiO-67	147	162	152	upper
UiO-67-CH_3	147	143	152	lower
UiO-67-NH_2	147	145	152	lower

Appendix Table A13. Equivalence tests between the model for UiO-67-CH3 and UiO-67 show that the growth rate and inflection points of the models were significantly different.

level	lower CL	ratio	upper CL	limit exceeded
growth rate	1.38	1.60	1.81	both
inflection point	1.21	1.26	1.30	upper
asymptote	1.12	1.13	1.15	

Appendix Table A14. Equivalence tests between the model for UiO-67-CH_3 and UiO-67-NH_2 show that the growth rate and inflection points of the models were significantly different.

level	lower CL	ratio	upper CL	limit exceeded
growth rate	1.06	1.22	1.37	upper
inflection point	0.76	0.79	0.82	lower
asymptote	1.00	1.01	1.03	

The differences in binding energies for DMMP in the UiO-67-NH_2, UiO-67-CH_3, and UiO-67 MOFs can give rise to equilibrium concentration differences in a stratified MOF. Assume a three-stratum MOF UiO-67-NH_2⊂UiO-67-CH_3⊂UiO-67 (inner most stratum MOF UiO-67-NH_2). The DFT calculated binding energies for DMMP in these MOFs are -74, -71, and -64 kJ/mol, respectively. Assuming a Boltzmann distribution and referencing to UiO-67 (differential binding energies of -10, -7, 0 kJ/mol, respectively) gives Boltzmann factors of 55.1 and 16.6 for UiO-67-NH_2 and UiO-67-CH_3, respectively. Thus, the concentration of DMMP in the UiO-67-NH_2 stratum should be 55.1 times larger than in UiO-67.

Appendix B Additional Figures and Tables for Chapter 3

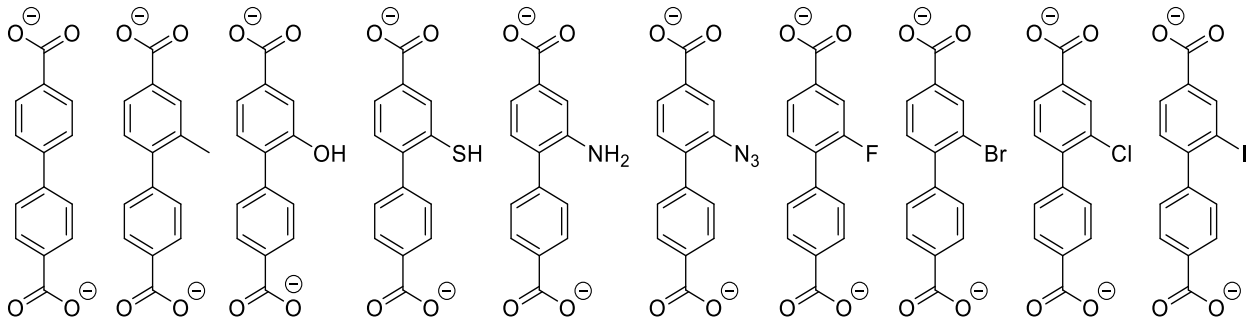

Appendix Figure B1. Ligands considered in this work are based on our previous work.1 From left to right: BPDC, CH3-BPDC, OH-BPDC, SH-BPDC, NH2-BPDC, N3-BPDC, F-BPDC, Br-BPDC, Cl-BPDC, I-BPDC.

Appendix Table B1. Tabulated binding energies of HD and 2-CEES in UiO-67-X

MOF	HD Energy (kJ/mol)	2-CEES Energy (kJ/mol)
UiO-67-NH_2	-132.5	-114.7
UiO-67-OH	-131.0	-114.0
UiO-67-CH_3	-129.6	-107.4
UiO-67	-124.4	-107.1
UiO-67-I	-122.2	-106.2
UiO-67-Br	-122.1	-106.1
UiO-67-Cl	-117.7	-101.5
UiO-67-F	-117.2	-102.1
UiO-67-SH	-116.4	-97.5
UiO-67-N_3	-92.1	-76.9
STDDEV	**11.5**	**10.68**
mean	**-120.5**	**-103.36**

a)

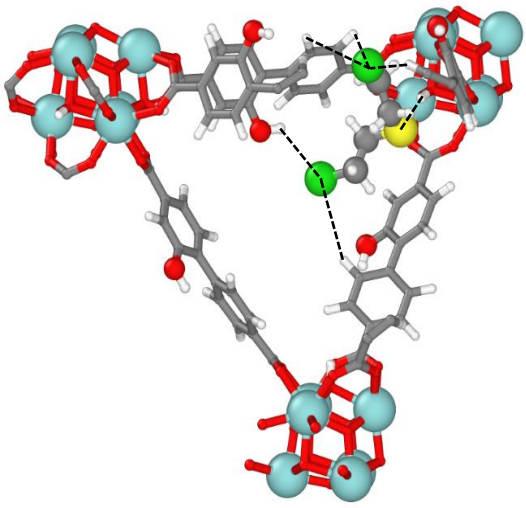

b

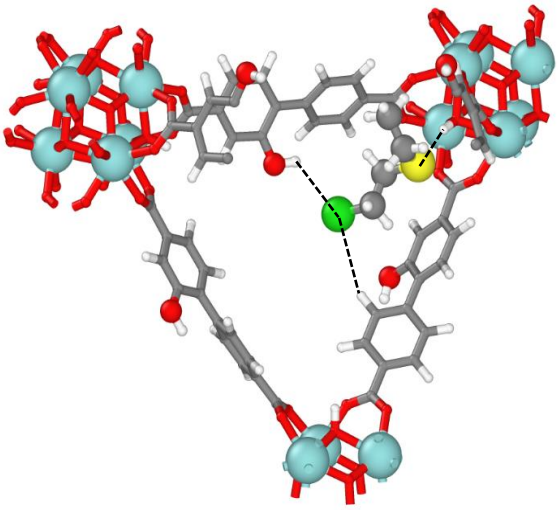

Appendix Figure B2. Binding configurations in UiO-67-OH. a) HD: The S···H hydrogen bond is 2.65 Å. The upper Cl-H electrostatic interactions are, from left to right, 4.05 Å, 4.09 Å and 3.23 Å. The Cl-HO electrostatic interaction is 2.93 Å. The lower Cl-H electrostatic interaction is 3.73 Å. b) 2-CEES: The S···H hydrogen bond is 2.58 Å. The Cl-HO electrostatic interaction is 2.98 Å. The Cl-H electrostatic interaction is 3.63 Å. Zr is shown in teal, C in grey, O in red, H in white, S in yellow, and Cl in green.

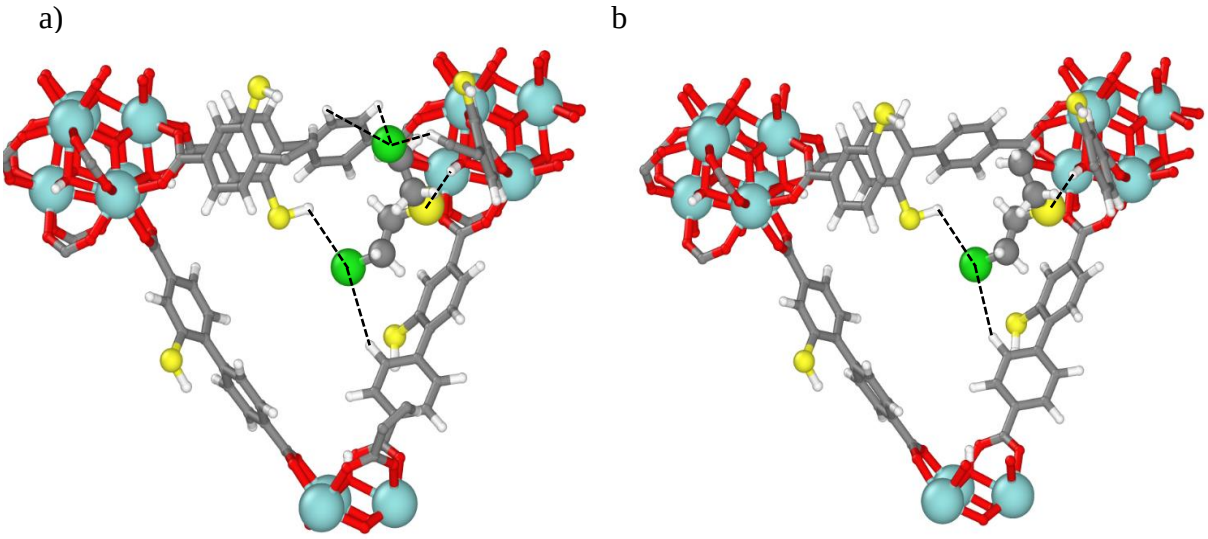

Appendix Figure B3. Binding configurations in UiO-67-SH. a) HD: The upper Cl-H electrostatic interactions are, from left to right, 4.13 Å, 4.21 Å, and 3.17 Å. The S···H hydrogen bond is 2.65 Å. The SH-Cl electrostatic interaction is 3.02 Å. The lower Cl-H electrostatic interaction is 3.34 Å. b) 2-CEES: The S···H hydrogen bond is 2.56 Å. The Cl-H electrostatic interaction is 3.26 Å. The SH-Cl electrostatic interaction is 3.00 Å. Zr is shown in teal, C in grey, O in red, H in white, S in yellow, and Cl in green.

Appendix Table B2. Distances and angles of the XH-Cl interaction found in the hydrogen bonder functionalized MOFs with HD.

	HD		2-CEES	
X	**Distance (Å)**	**Angle (°)**	**Distance (Å)**	**Angle (°)**
N	2.89	135.4	2.91	133.2
O	2.93	125.0	2.98	125.3
S	3.02	112.5	3.00	111.1

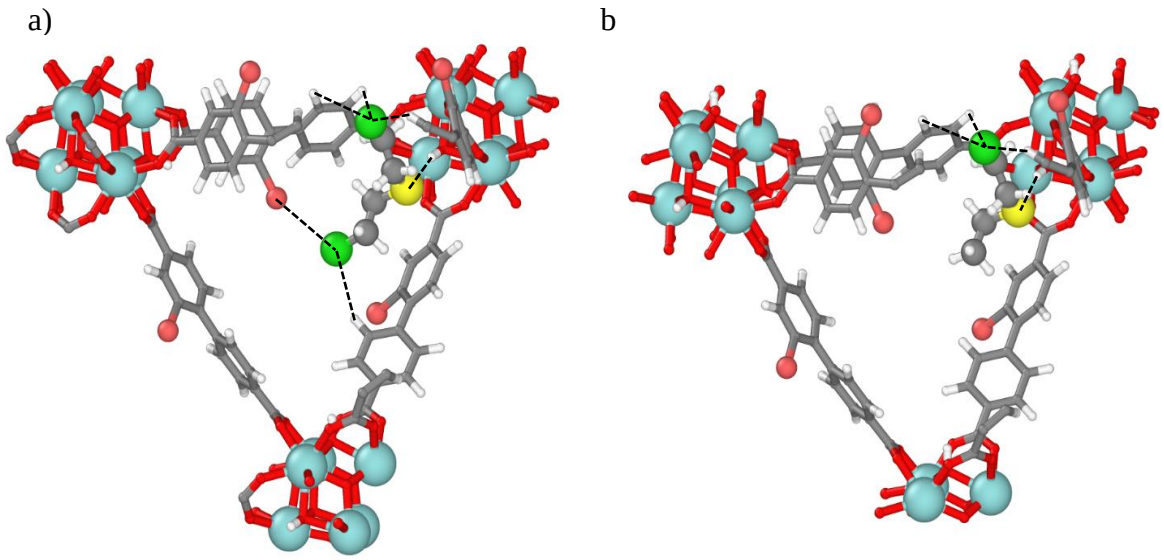

Appendix Figure B4. Binding configurations in UiO-67-Br. a) HD: The upper Cl-H electrostatic interactions are, from left to right, 4.05 Å, 4.02 Å, and 3.49 Å. The S···H hydrogen bond is 2.59 Å. The Cl-Br electrostatic interaction distance is 3.67 Å, and the Cl-H interaction distance is 3.21 Å. b) 2-CEES: The Cl-H electrostatic interactions are, from left to right, 4.16 Å, 4.04 Å, and 3.37 Å. The S···H hydrogen bond is 2.54 Å. The Cl-Br electrostatic interaction has a distance of 3.63 Å, and the Cl-H interaction has a distance of 3.18 Å. Zr is shown in teal, C in grey, O in red, H in white, S in yellow, Cl in green, and Br in pink.

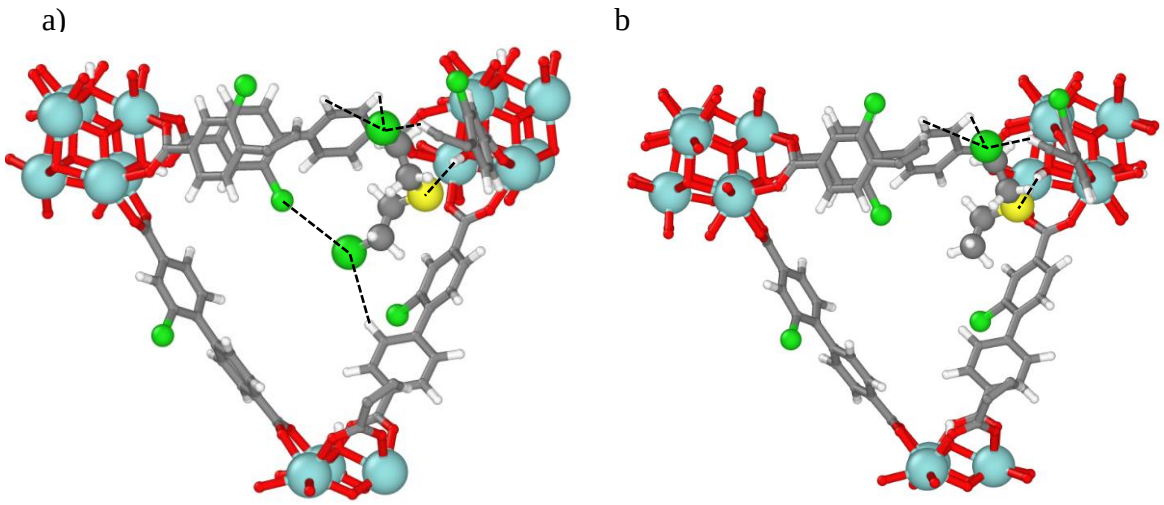

Appendix Figure B5. Binding configurations in UiO-67-Cl a) HD: The upper Cl-H electrostatic interactions are, from left to right, 4.03 Å, 3.99 Å, and 3.48 Å. The S···H hydrogen bond is 2.67 Å. The Cl-Cl distance is 3.73 Å, and the lower Cl-H electrostatic interaction is 3.29 Å. b) 2-CEES: The Cl-H electrostatic interactions are, from left to right, 4.07 Å, 4.05 Å, and 3.42 Å. The S···H hydrogen bond is 2.51 Å. Zr is shown in teal, C in grey, O in red, H in white, S in yellow, and Cl in green.

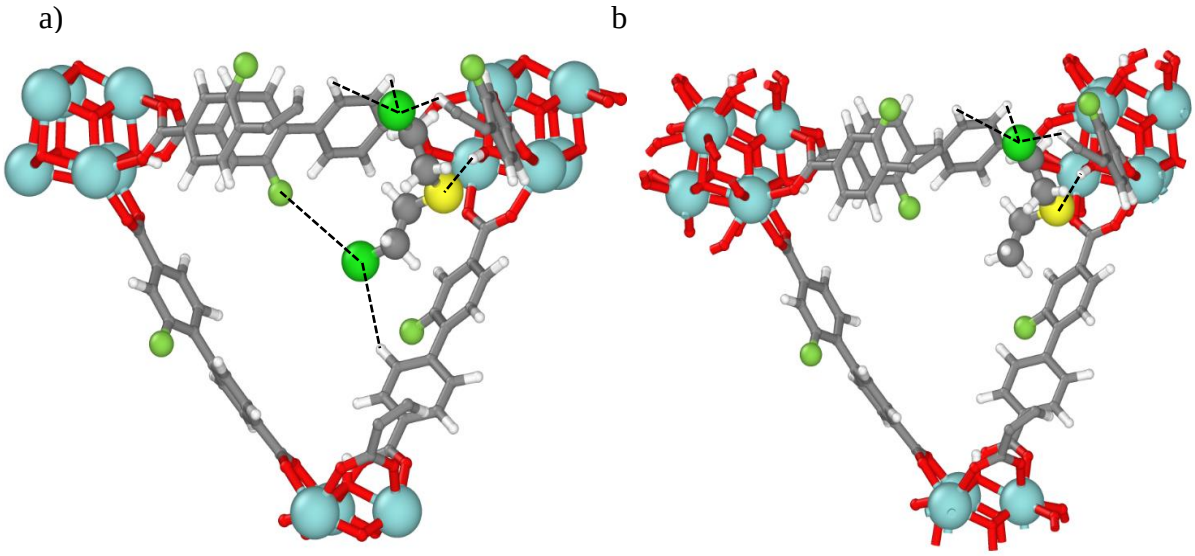

Appendix Figure B6. Binding configurations in UiO-67-F a) HD: The upper Cl-H electrostatic interactions are, from left to right, 4.03 Å, 3.99 Å, and 3.48 Å. The S···H hydrogen bond is 2.67 Å. The Cl-F distance is 3.73 Å, and the lower Cl-H electrostatic interaction is 3.29 Å. b) 2-CEES: The Cl-H electrostatic interactions are, from left to right, 4.16 Å, 4.10 Å, and 3.54 Å. The S···H hydrogen bond is 2.50 Å. Zr is shown in teal, C in grey, O in red, H in white, S in yellow, Cl in green, and F in olive.

Appendix Table B3. Cl-X repulsion distances in UiO-67-X + HD configurations.

X	Distance (Å)
I	3.65
Br	3.63
Cl	3.73
F	3.73

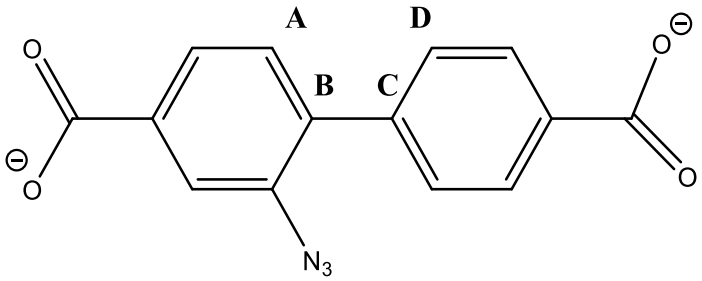

Appendix Figure B7. Atomic coordinates of the carbons labeled A, B, C, and D were used to calculate dihedral torsions via Avogadro 1.2[169]

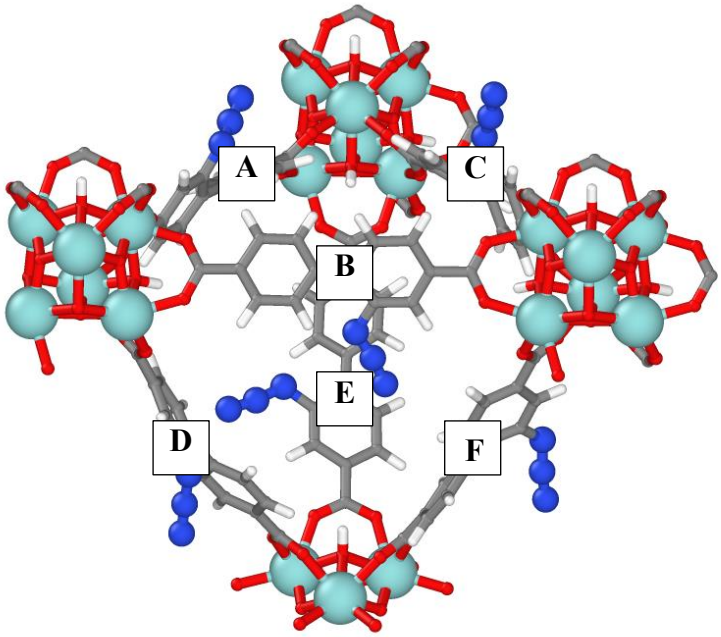

Appendix Figure B8. Ligand labels for reporting torsion angles. The analyte occupies the pocket formed by ligands A, B, and D.

Appendix Table B4. Dihedral torsion angles for UiO-67-NH_2.

	Angle (°)			Δ°		
Ligand	**HD**	**2-CEES**	**Void MOF**	**HD/2-CEES**	**HD/Void**	**2-CEES/Void**
A	42.9	40.1	41.6	2.8	1.3	1.5
B	37.9	38.6	43.5	0.7	5.6	4.9
C	-41.7	-41.4	-41.0	0.3	0.7	0.4
D	-42.0	-42.0	-39.6	0.0	2.4	2.4
E	-41.6	-41.5	-41.7	0.1	0.1	0.2
F	-42.0	-41.0	-41.1	1.0	0.9	0.1
Average (magnitude)	**41.4**	**40.8**	**41.4**	**0.8**	**1.8**	**1.6**
Std Dev	**1.6**	**1.1**	**1.2**	**1.0**	**1.8**	**1.7**

Appendix Table B5. Dihedral torsion angles for UiO-67-OH.

	Angle (°)			Δ°		
Ligand	**HD**	**2-CEES**	**Void MOF**	**HD/2-CEES**	**HD/Void**	**2-CEES/Void**
A	43.1	40.8	40.7	2.3	2.4	0.1
B	40.7	39.0	42.8	1.7	2.1	3.8
C	-42.3	-41.5	-42.6	0.8	0.3	1.1
D	-41.3	-41.7	-41.2	0.4	0.1	0.5
E	-43.3	-42.9	-43.6	0.4	0.3	0.7
F	-42.0	-42.0	-42.4	0.0	0.4	0.4
Average (magnitude)	**42.1**	**41.3**	**42.2**	**0.9**	**0.9**	**1.1**
Std Dev	**0.9**	**1.2**	**1.0**	**0.8**	**0.9**	**1.2**

Appendix Table B6. Dihedral torsion angles for UiO-67-SH.

	Angle (°)			Δ°		
Ligand	**HD**	**2-CEES**	**Void MOF**	**HD/2-CEES**	**HD/Void**	**2-CEES/Void**
A	49.1	43.8	46.7	5.3	2.4	2.9
B	44.0	42.5	47.7	1.5	3.7	5.2
C	-47.0	-45.5	-46.5	1.5	0.5	1.0
D	-46.4	-46.1	-45.7	0.3	0.7	0.4
E	-47.4	-45.7	-47.3	1.7	0.1	1.6
F	-49.1	-45.8	-47.2	3.3	1.9	1.4
Average (magnitude)	**47.2**	**44.9**	**46.9**	**2.3**	**1.6**	**2.1**
Std Dev	**1.7**	**1.3**	**0.6**	**1.6**	**1.3**	**1.6**

Appendix Table B7. Dihedral torsion angles for UiO-67-CH_3.

	Angle (°)			Δ°		
Ligand	**HD**	**2-CEES**	**Void MOF**	**HD/2-CEES**	**HD/Void**	**2-CEES/Void**
A	43.2	41.0	44.3	2.2	1.1	3.3
B	40.2	38.6	45.7	1.6	5.5	7.1
C	-44.0	-42.0	-44.9	2.0	0.9	2.9
D	-43.4	-42.2	-44.4	1.2	1.0	2.2
E	-44.0	-41.9	-45.4	2.1	1.4	3.5
F	-44.0	-42.3	-45.7	1.7	1.7	3.4
Average (magnitude)	**43.1**	**41.3**	**45.1**	**1.8**	**1.9**	**3.7**
Std Dev	**1.3**	**1.3**	**0.6**	**0.3**	**1.6**	**1.6**

Appendix Table B8. Dihedral torsion angles for UiO-67.

	Angle (°)			Δ°		
Ligand	**HD**	**2-CEES**	**Void MOF**	**HD/2-CEES**	**HD/Void**	**2-CEES/Void**
A	32.6	32.4	30.1	0.2	2.5	2.3
B	26.5	28.6	30.7	2.1	4.2	2.1
C	-31.8	-31.3	-31.5	0.5	0.3	0.2
D	-33.0	-32.5	-31.0	0.5	2.0	1.5
E	-31.6	-31.5	-31.6	0.1	0.0	0.1
F	-31.4	-31.8	-32.1	0.4	0.7	0.3
Average (magnitude)	**31.2**	**31.4**	**31.2**	**0.6**	**1.6**	**1.1**
Std Dev	**2.2**	**1.3**	**0.7**	**0.7**	**1.5**	**0.9**

Appendix Table B9. Dihedral torsion angles for UiO-67-I.

	Angle (°)			Δ°		
Ligand	**HD**	**2-CEES**	**Void MOF**	**HD/2-CEES**	**HD/Void**	**2-CEES/Void**
A	46.1	46.9	46.4	0.8	0.3	0.5
B	45.8	46.0	47.3	0.2	1.5	1.3
C	-46.2	-47.3	-46.9	1.1	0.7	0.4
D	-45.2	-44.9	-46.7	0.3	1.5	1.8
E	-46.3	-47.4	-48.9	1.1	2.6	1.5
F	-46.7	-47.9	-48.6	1.2	1.9	0.7
Average (magnitude)	**46.1**	**46.7**	**47.5**	**0.8**	**1.4**	**1.0**
Std Dev	**0.5**	**1.0**	**0.9**	**0.4**	**0.8**	**0.5**

Appendix Table B 10. Dihedral torsion angles for UiO-67-Br.

	Angle (°)			Δ°		
Ligand	**HD**	**2-CEES**	**Void MOF**	**HD/2-CEES**	**HD/Void**	**2-CEES/Void**
A	45.0	45.1	45.2	0.1	0.2	0.1
B	44.4	44.2	45.8	0.2	1.4	1.6
C	-45.1	-45.2	-45.5	0.1	0.4	0.3
D	-44.0	-43.1	-44.6	0.9	0.6	1.5
E	-45.2	-45.1	-46.2	0.1	1.0	1.1
F	-45.7	-45.8	-45.8	0.1	0.1	0.0
Average (magnitude)	**44.9**	**44.8**	**45.5**	**0.2**	**0.6**	**0.8**
Std Dev	**0.6**	**0.9**	**0.5**	**0.3**	**0.5**	**0.7**

Appendix Table B11. Dihedral torsion angles for UiO-67-Cl.

	Angle (°)			Δ°		
Ligand	**HD**	**2-CEES**	**Void MOF**	**HD/2-CEES**	**HD/Void**	**2-CEES/Void**
A	45.9	43.2	43.1	2.7	2.8	0.1
B	42.7	42.7	43.4	0.0	0.7	0.7
C	-44.3	-44.1	-44.7	0.2	0.4	0.6
D	-43.6	-43.3	-44.5	0.3	0.9	1.2
E	-44.1	-43.9	-44.9	0.2	0.8	1.0
F	-44.8	-44.4	-45.6	0.4	0.8	1.2
Average (magnitude)	**44.2**	**43.6**	**44.4**	**0.6**	**1.1**	**0.8**
Std Dev	**1.0**	**0.6**	**0.9**	**0.9**	**0.8**	**0.4**

Appendix Table B 12. Dihedral torsion angles for UiO-67-F.

	Angle (°)			Δ°		
Ligand	**HD**	**2-CEES**	**Void MOF**	**HD/2-CEES**	**HD/Void**	**2-CEES/Void**
A	34.1	34.0	34.1	0.1	0.0	0.1
B	33.5	34.9	38.5	1.4	5.0	3.6
C	-34.7	-35.1	-36.0	0.4	1.3	0.9
D	-34.5	-34.4	-33.1	0.1	1.4	1.3
E	-35.7	-36.2	-36.7	0.5	1.0	0.5
F	-34.1	-34.6	-35.7	0.5	1.6	1.1
Average (magnitude)	**34.4**	**34.9**	**35.7**	**0.5**	**1.7**	**1.3**
Std Dev	**0.7**	**0.7**	**1.7**	**0.4**	**1.6**	**1.1**

Appendix C Additional Figures and Tables for Chapter 4

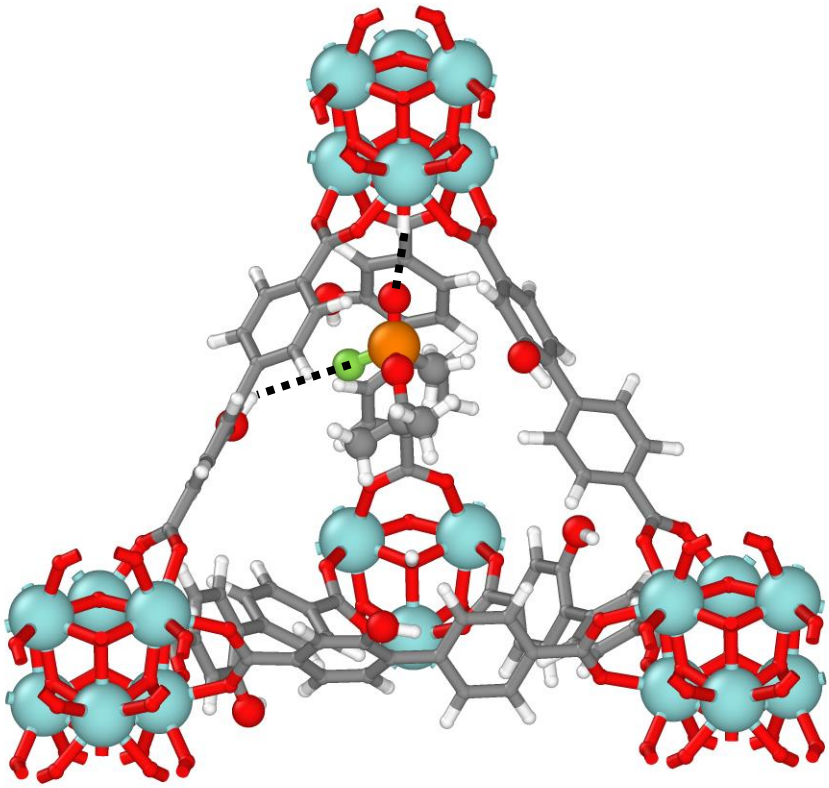

Appendix Figure C1. UiO-67-OH and GB comparable binding configuration to those shown for UiO-67-NH_2 and UiO-67 in Figure 24. Zr is shown in teal, C in grey, O in red, H in white, F in olive, and P in orange.

Appendix Table C1. Hydrogen bond lengths of the functionalized MOFs with VX.

MOF	H Bond Length (Å)
OH	1.78
NH_2	1.79
H	1.78

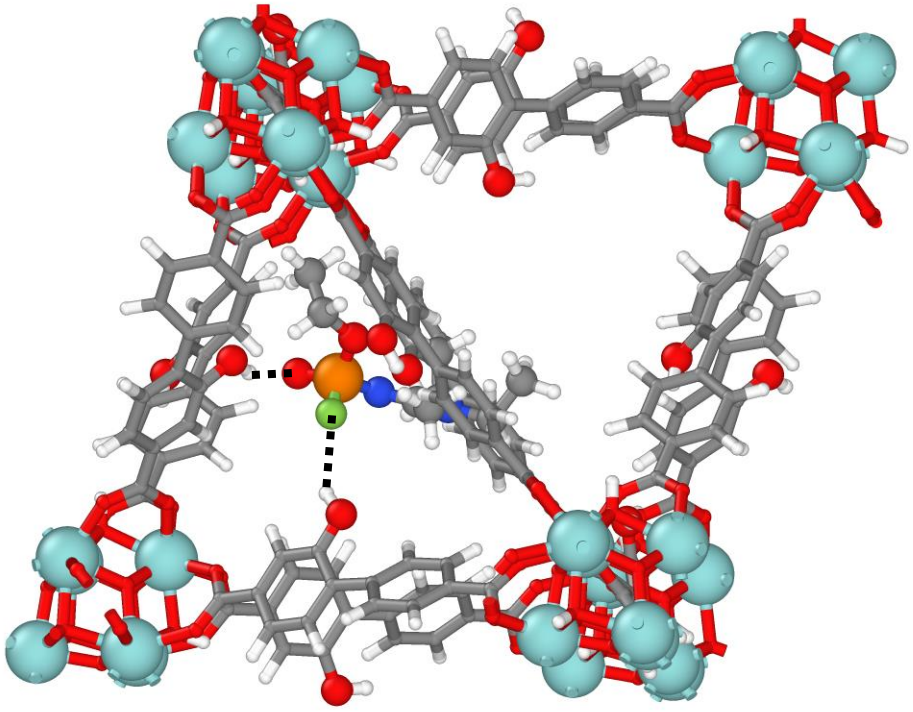

Appendix Figure C2. UiO-67-OH Corresponding structure to UiO-67-NH_2 + A-234 shown in Figure 26b. The OH···O hydrogen bond length is 1.83 Å and the OH···F hydrogen bond length is 2.65 Å. Zr is shown in teal, C in grey, O in red, H in white, F in olive, P in orange, and N in blue.

Appendix Table C2. Hydrogen bond angles comparing the A-234 interactions shown in Figure 26b and Appendix Figure C2.

Bond	Angle (°)
NH···O	156.4
OH···O	150.0
NH···F	144.5
OH···F	141.6

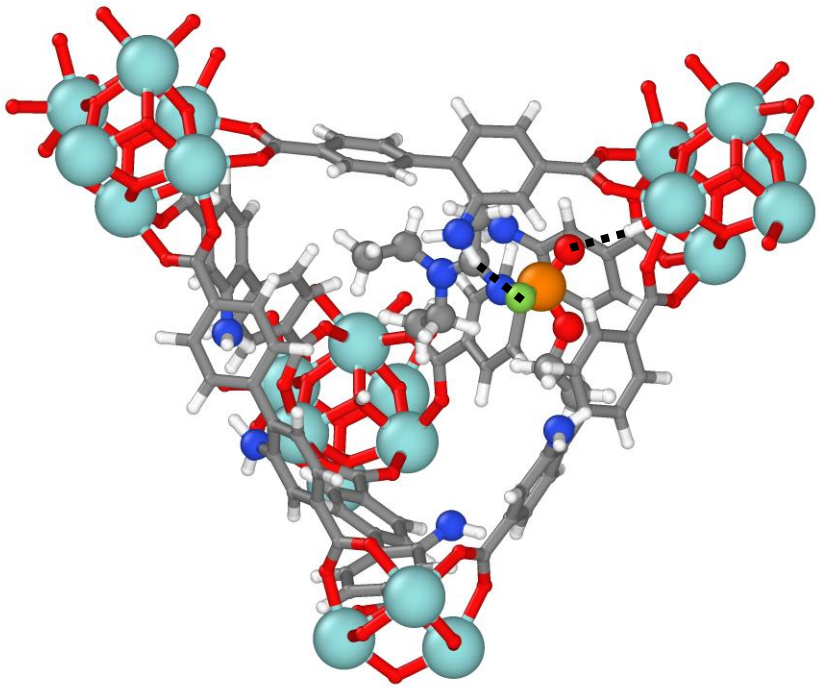

Appendix Figure C3. Optimum binding configuration of UiO-67-NH_2 and A-234 in the μ_3-OH tetrahedral pore. The OH···O hydrogen bond is 2.06 Å and the NH···F hydrogen bond is 2.48 Å. Zr is shown in teal, C in grey, O in red, H in white, F in olive, P in orange, and N in blue.

Bibliography

1.Ruffley, J. P.; Goodenough, I.; Luo, T.-Y.; Richard, M.; Borguet, E.; Rosi, N. L.; Johnson, J. K., Design, Synthesis, and Characterization of Metal–Organic Frameworks for Enhanced Sorption of Chemical Warfare Agent Simulants. *J. Phys. Chem. C* **2019**, *123*, 19748-19758.

2.Jacoby, M., Building A Better Gas Mask. *C&EN* **2014**, *92*, 34-38.

3.Morrison, R. W. In *Overview of current collective protection filtration technology*, NBC Defense Collective Protection Conference, 2002.

4.Prasad, G.; Singh, B.; Vijayaraghavan, R., Respiratory protection against chemical and biological warfare agents. *Defence Science Journal* **2008**, *58*, 686.

5.Bobbitt, N. S.; Mendonca, M. L.; Howarth, A. J.; Islamoglu, T.; Hupp, J. T.; Farha, O. K.; Snurr, R. Q., Metal–Organic Frameworks for the Removal of Toxic Industrial Chemicals and Chemical Warfare Agents. *Chem. Soc. Rev.* **2017**, *46*, 3357-3385.

6.Linders, M. J. G.; Baak, P. J.; van Bokhoven, J. J. G. M., Exploratory Investigation of the Risk of Desorption from Activated Carbon Filters in Respiratory Protective Devices. *Industrial & Engineering Chemistry Research* **2007**, *46*, 4034-4039.

7.*Adsorption and Desorption of Chemical Warfare Agents on Activated Carbon: Impact of Temperature and Relative Humidity*; U.S. Environmental Protection Agency: Washington D.C., 2014.

8.Liao, P.-Q.; Huang, N.-Y.; Zhang, W.-X.; Zhang, J.-P.; Chen, X.-M., Controlling guest conformation for efficient purification of butadiene. *Science* **2017**, *356*, 1193-1196.

9.Herm, Z. R.; Wiers, B. M.; Mason, J. A.; van Baten, J. M.; Hudson, M. R.; Zajdel, P.; Brown, C. M.; Masciocchi, N.; Krishna, R.; Long, J. R., Separation of Hexane Isomers in a Metal-Organic Framework with Triangular Channels. *Science* **2013**, *340*, 960-964.

10.Li, T.; Chen, D.-L.; Sullivan, J. E.; Kozlowski, M. T.; Johnson, J. K.; Rosi, N. L., Systematic modulation and enhancement of CO_2 : N_2 selectivity and water stability in an isoreticular series of bio-MOF-11 analogues. *Chemical Science* **2013**, *4*, 1746-1755.

11.Fracaroli, A. M.; Furukawa, H.; Suzuki, M.; Dodd, M.; Okajima, S.; Gándara, F.; Reimer, J. A.; Yaghi, O. M., Metal–Organic Frameworks with Precisely Designed Interior for Carbon

Dioxide Capture in the Presence of Water. *Journal of the American Chemical Society* **2014**, *136*, 8863-8866.

12.Ploskonka, A. M.; DeCoste, J. B., Tailoring the Adsorption and Reaction Chemistry of the Metal–Organic Frameworks UiO-66, UiO-66-NH_2, and HKUST-1 via the Incorporation of Molecular Guests. *ACS Applied Materials & Interfaces* **2017**, *9*, 21579-21585.

13.de Koning, M. C.; van Grol, M.; Breijaert, T., Degradation of Paraoxon and the Chemical Warfare Agents VX, Tabun, and Soman by the Metal–Organic Frameworks UiO-66-NH_2, MOF-808, NU-1000, and PCN-777. *Inorg. Chem.* **2017**, *56*, 11804-11809.

14.Liu, Y.; Howarth, A. J.; Hupp, J. T.; Farha, O. K., Selective Photooxidation of a Mustard-Gas Simulant Catalyzed by a Porphyrinic Metal–Organic Framework. *Angewandte Chemie International Edition* **2015**, *54*, 9001-9005.

15.Liu, Y.; Buru, C. T.; Howarth, A. J.; Mahle, J. J.; Buchanan, J. H.; DeCoste, J. B.; Hupp, J. T.; Farha, O. K., Efficient and selective oxidation of sulfur mustard using singlet oxygen generated by a pyrene-based metal–organic framework. *Journal of Materials Chemistry A: Materials for Energy and Sustainability* **2016**, *4*, 13809-13813.

16.Bromberg, L.; Klichko, Y.; Chang, E. P.; Speakman, S.; Straut, C. M.; Wilusz, E.; Hatton, T. A., Alkylaminopyridine-Modified Aluminum Aminoterephthalate Metal-Organic Frameworks As Components of Reactive Self-Detoxifying Materials. *ACS Applied Materials & Interfaces* **2012**, *4*, 4595-4602.

17.Mondloch, J. E.; Katz, M. J.; Isley Iii, W. C.; Ghosh, P.; Liao, P.; Bury, W.; Wagner, G. W.; Hall, M. G.; DeCoste, J. B.; Peterson, G. W., et al., Destruction of chemical warfare agents using metal–organic frameworks. *Nature Materials* **2015**, *14*, 512.

18.Katz, M. J.; Mondloch, J. E.; Totten, R. K.; Park, J. K.; Nguyen, S. T.; Farha, O. K.; Hupp, J. T., Simple and Compelling Biomimetic Metal–Organic Framework Catalyst for the Degradation of Nerve Agent Simulants. *Angewandte Chemie International Edition* **2014**, *53*, 497-501.

19.Katz, M. J.; Moon, S.-Y.; Mondloch, J. E.; Beyzavi, M. H.; Stephenson, C. J.; Hupp, J. T.; Farha, O. K., Exploiting parameter space in MOFs: a 20-fold enhancement of phosphate-ester hydrolysis with UiO-66-NH2. *Chemical Science* **2015**, *6*, 2286-2291.

20.Gil-San-Millan, R.; López-Maya, E.; Hall, M.; Padial, N. M.; Peterson, G. W.; DeCoste, J. B.; Rodríguez-Albelo, L. M.; Oltra, J. E.; Barea, E.; Navarro, J. A. R., Chemical Warfare Agents Detoxification Properties of Zirconium Metal–Organic Frameworks by Synergistic Incorporation of Nucleophilic and Basic Sites. *ACS Applied Materials & Interfaces* **2017**, *9*, 23967-23973.

21.Zhao, J.; Lee, D. T.; Yaga, R. W.; Hall, M. G.; Barton, H. F.; Woodward, I. R.; Oldham, C. J.; Walls, H. J.; Peterson, G. W.; Parsons, G. N., Ultra-Fast Degradation of Chemical Warfare Agents Using MOF–Nanofiber Kebabs. *Angew. Chem. Int. Ed.* **2016**, *55*, 13224-13228.

22.Wang, G.; Sharp, C.; Plonka, A. M.; Wang, Q.; Frenkel, A. I.; Guo, W.; Hill, C.; Smith, C.; Kollar, J.; Troya, D., et al., Mechanism and Kinetics for Reaction of the Chemical Warfare Agent Simulant, DMMP(g), with Zirconium(IV) MOFs: An Ultrahigh-Vacuum and DFT Study. *The Journal of Physical Chemistry C* **2017**, *121*, 11261-11272.

23.DeCoste, J. B.; Rossin, J. A.; Peterson, G. W., Hierarchical Pore Development by Plasma Etching of Zr-Based Metal–Organic Frameworks. *Chem. - Eur. J.* **2015**, *21*, 18029-18032.

24.Mondal, S. S.; Holdt, H.-J., Breaking Down Chemical Weapons by Metal–Organic Frameworks. *Angew. Chem. Int. Ed.* **2016**, *55*, 42-44.

25.Lee, D. T.; Zhao, J.; Oldham, C. J.; Peterson, G. W.; Parsons, G. N., UiO-66-NH_2 Metal–Organic Framework (MOF) Nucleation on TiO_2, ZnO, and Al_2O_3 Atomic Layer Deposition-Treated Polymer Fibers: Role of Metal Oxide on MOF Growth and Catalytic Hydrolysis of Chemical Warfare Agent Simulants. *ACS Appl. Mater. Interfaces* **2017**, *9*, 44847-44855.

26.López-Maya, E.; Montoro, C.; Rodríguez-Albelo, L. M.; Aznar Cervantes, S. D.; Lozano-Pérez, A. A.; Cenís, J. L.; Barea, E.; Navarro, J. A. R., Textile/Metal–Organic-Framework Composites as Self-Detoxifying Filters for Chemical-Warfare Agents. *Angewandte Chemie International Edition* **2015**, *54*, 6790-6794.

27.Cavka, J. H.; Jakobsen, S.; Olsbye, U.; Guillou, N.; Lamberti, C.; Bordiga, S.; Lillerud, K. P., A New Zirconium Inorganic Building Brick Forming Metal Organic Frameworks with Exceptional Stability. *JACS* **2008**, *130*, 13850-13851.

28.DeCoste, J. B.; Peterson, G. W.; Jasuja, H.; Glover, T. G.; Huang, Y.-g.; Walton, K. S., Stability and degradation mechanisms of metal–organic frameworks containing the $Zr_6O_4(OH)_4$ secondary building unit. *J. Mater. Chem. A* **2013**, *1*, 5642-5650.

29.Valenzano, L.; Civalleri, B.; Chavan, S.; Bordiga, S.; Nilsen, M. H.; Jakobsen, S.; Lillerud, K. P.; Lamberti, C., Disclosing the Complex Structure of UiO-66 Metal Organic Framework: A Synergic Combination of Experiment and Theory. *Chem. Mater.* **2011**, *23*, 1700-1718.

30.Kandiah, M.; Nilsen, M. H.; Usseglio, S.; Jakobsen, S.; Olsbye, U.; Tilset, M.; Larabi, C.; Quadrelli, E. A.; Bonino, F.; Lillerud, K. P., Synthesis and Stability of Tagged UiO-66 Zr-MOFs. *Chem. Mater.* **2010**, *22*, 6632-6640.

31.Kutzscher, C.; Nickerl, G.; Senkovska, I.; Bon, V.; Kaskel, S., Proline Functionalized UiO-67 and UiO-68 Type Metal–Organic Frameworks Showing Reversed Diastereoselectivity in Aldol Addition Reactions. *Chemistry of Materials* **2016**, *28*, 2573-2580.

32.Biswas, S.; Van Der Voort, P., A General Strategy for the Synthesis of Functionalised UiO-66 Frameworks: Characterisation, Stability and CO_2 Adsorption Properties. *Eur. J. Inorg. Chem.* **2013**, *2013*, 2154-2160.

33.Øien-Ødegaard, S.; Bouchevreau, B.; Hylland, K.; Wu, L.; Blom, R.; Grande, C.; Olsbye, U.; Tilset, M.; Lillerud, K. P., UiO-67-type Metal–Organic Frameworks with Enhanced Water Stability and Methane Adsorption Capacity. *Inorganic Chemistry* **2016**, *55*, 1986-1991.

34.Peterson, G. W.; Destefano, M. R.; Garibay, S. J.; Ploskonka, A.; McEntee, M.; Hall, M.; Karwacki, C. J.; Hupp, J. T.; Farha, O. K., Optimizing Toxic Chemical Removal through Defect-Induced UiO-66-NH_2 Metal–Organic Framework. *Chemistry - A European Journal* **2017**, *23*, 15913-15916.

35.Moon, S.-Y.; Wagner, G. W.; Mondloch, J. E.; Peterson, G. W.; DeCoste, J. B.; Hupp, J. T.; Farha, O. K., Effective, Facile, and Selective Hydrolysis of the Chemical Warfare Agent VX Using Zr6-Based Metal–Organic Frameworks. *Inorg. Chem.* **2015**, *54*, 10829-10833.

36.Trickett, C. A.; Gagnon, K. J.; Lee, S.; Gándara, F.; Bürgi, H.-B.; Yaghi, O. M., Definitive Molecular Level Characterization of Defects in UiO-66 Crystals. *Angewandte Chemie International Edition* **2015**, *54*, 11162-11167.

37.Luo, T.-Y.; Liu, C.; Gan, X. Y.; Muldoon, P. F.; Diemler, N. A.; Millstone, J. E.; Rosi, N. L., Multivariate Stratified Metal–Organic Frameworks: Diversification Using Domain Building Blocks. *Journal of the American Chemical Society* **2019**, *141*, 2161-2168.

38.Wu, H.; Yildirim, T.; Zhou, W., Exceptional Mechanical Stability of Highly Porous Zirconium Metal–Organic Framework UiO-66 and Its Important Implications. *The Journal of Physical Chemistry Letters* **2013**, *4*, 925-930.

39.Lawrence, M. C.; Schneider, C.; Katz, M. J., Determining the structural stability of UiO-67 with respect to time: a solid-state NMR investigation. *Chemical Communications* **2016**, *52*, 4971-4974.

40.Katz, M. J.; Brown, Z. J.; Colón, Y. J.; Siu, P. W.; Scheidt, K. A.; Snurr, R. Q.; Hupp, J. T.; Farha, O. K., A facile synthesis of UiO-66, UiO-67 and their derivatives. *Chemical Communications* **2013**, *49*, 9449-9451.

41.Vermoortele, F.; Vandichel, M.; Van de Voorde, B.; Ameloot, R.; Waroquier, M.; Van Speybroeck, V.; De Vos, D. E., Electronic Effects of Linker Substitution on Lewis Acid Catalysis

with Metal–Organic Frameworks. *Angewandte Chemie International Edition* **2012**, *51*, 4887-4890.

42.Kim, M.; Cahill, J. F.; Su, Y.; Prather, K. A.; Cohen, S. M., Postsynthetic ligand exchange as a route to functionalization of 'inert' metal–organic frameworks. *Chemical Science* **2012**, *3*, 126-130.

43.DeStefano, M. R.; Islamoglu, T.; Garibay, S. J.; Hupp, J. T.; Farha, O. K., Room-Temperature Synthesis of UiO-66 and Thermal Modulation of Densities of Defect Sites. *Chemistry of Materials* **2017**, *29*, 1357-1361.

44.Zhang, J.; Dolg, M., ABCluster: the artificial bee colony algorithm for cluster global optimization. *Physical Chemistry Chemical Physics* **2015**, *17*, 24173-24181.

45.Zhang, J.; Dolg, M., Global optimization of clusters of rigid molecules using the artificial bee colony algorithm. *Physical Chemistry Chemical Physics* **2016**, *18*, 3003-3010.

46.Neese, F., The ORCA program system. *Wiley Interdisciplinary Reviews: Computational Molecular Science* **2012**, *2*, 73-78.

47.Perdew, J. P.; Burke, K.; Ernzerhof, M., Generalized Gradient Approximation Made Simple. *Physical Review Letters* **1996**, *77*, 3865-3868.

48.Weigend, F.; Ahlrichs, R., Balanced basis sets of split valence, triple zeta valence and quadruple zeta valence quality for H to Rn: Design and assessment of accuracy. *Physical Chemistry Chemical Physics* **2005**, *7*, 3297-3305.

49.Weigend, F., Accurate Coulomb-fitting basis sets for H to Rn. *Physical Chemistry Chemical Physics* **2006**, *8*, 1057-1065.

50.Grimme, S.; Antony, J.; Ehrlich, S.; Krieg, H., A consistent and accurate ab initio parametrization of density functional dispersion correction (DFT-D) for the 94 elements H-Pu. *The Journal of Chemical Physics* **2010**, *132*, 154104.

51.Grimme, S.; Ehrlich, S.; Goerigk, L., Effect of the damping function in dispersion corrected density functional theory. *Journal of Computational Chemistry* **2011**, *32*, 1456-1465.

52.Boys, S. F.; Bernardi, F., The calculation of small molecular interactions by the differences of separate total energies. Some procedures with reduced errors. *Molecular Physics* **1970**, *19*, 553-566.

53.Frisch, M.; Trucks, G.; Schlegel, H.; Scuseria, G.; Robb, M.; Cheeseman, J.; Scalmani, G.; Barone, V.; Mennucci, B.; Petersson, G., Gaussian 09. 2014.

54.Guo, Y.; Riplinger, C.; Becker, U.; Liakos, D. G.; Minenkov, Y.; Cavallo, L.; Neese, F., Communication: An improved linear scaling perturbative triples correction for the domain based local pair-natural orbital based singles and doubles coupled cluster method [DLPNO-CCSD(T)]. *The Journal of Chemical Physics* **2018**, *148*, 011101.

55.Frigo, M.; Johnson, S. G., The Design and Implementation of FFTW3. *Proceedings of the IEEE* **2005**, *93*, 216-231.

56.VandeVondele, J.; Krack, M.; Mohamed, F.; Parrinello, M.; Chassaing, T.; Hutter, J., Quickstep: Fast and accurate density functional calculations using a mixed Gaussian and plane waves approach. *Computer Physics Communications* **2005**, *167*, 103-128.

57.VandeVondele, J.; Hutter, J., An efficient orbital transformation method for electronic structure calculations. *The Journal of Chemical Physics* **2003**, *118*, 4365-4369.

58.Ye, J.; Johnson, J. K., Screening Lewis Pair Moieties for Catalytic Hydrogenation of CO_2 in Functionalized UiO-66. *ACS Catalysis* **2015**, *5*, 6219-6229.

59.Goedecker, S.; Teter, M.; Hutter, J., Separable dual-space Gaussian pseudopotentials. *Physical Review B* **1996**, *54*, 1703-1710.

60.VandeVondele, J.; Hutter, J., Gaussian basis sets for accurate calculations on molecular systems in gas and condensed phases. *The Journal of Chemical Physics* **2007**, *127*, 114105.

61.Liu, D. C.; Nocedal, J., On the Limited Memory BFGS Method for Large Scale Optimization. *Math. Program.* **1989**, *45*, 503-528.

62.Ceriotti, M.; Bussi, G.; Parrinello, M., Langevin Equation with Colored Noise for Constant-Temperature Molecular Dynamics Simulations. *Physical Review Letters* **2009**, *102*, 020601.

63.Ceriotti, M.; Bussi, G.; Parrinello, M., Nuclear Quantum Effects in Solids Using a Colored-Noise Thermostat. *Phys. Rev. Lett.* **2009**, *103*, 030603.

64.Sokkalingam, N.; Kamath, G.; Coscione, M.; Potoff, J. J., Extension of the Transferable Potentials for Phase Equilibria Force Field to Dimethylmethyl Phosphonate, Sarin, and Soman. *The Journal of Physical Chemistry B* **2009**, *113*, 10292-10297.

65.Vishnyakov, A.; Neimark, A. V., Molecular Model of Dimethylmethylphosphonate and Its Interactions with Water. *J. Phys. Chem. A* **2004**, *108*, 1435-1439.

66.Vanduyfhuys, L.; Vandenbrande, S.; Verstraelen, T.; Schmid, R.; Waroquier, M.; Van Speybroeck, V., QuickFF: A program for a quick and easy derivation of force fields for metal-

organic frameworks from ab initio input. *Journal of Computational Chemistry* **2015**, *36*, 1015-1027.

67.J. Karl Johnson, J. R., Aleksey Vishnyakov, Alexander Neimark, 2018.

68.Ewald, P. P., Die Berechnung optischer und elektrostatischer Gitterpotentiale. *Annalen der Physik* **1921**, *369*, 253-287.

69.Plimpton, S., Fast Parallel Algorithms for Short-Range Molecular Dynamics. *Journal of Computational Physics* **1995**, *117*, 1-19.

70.Martyna, G. J.; Tobias, D. J.; Klein, M. L., Constant pressure molecular dynamics algorithms. *The Journal of Chemical Physics* **1994**, *101*, 4177-4189.

71.Dubbeldam, D.; Calero, S.; Ellis, D. E.; Snurr, R. Q., RASPA: molecular simulation software for adsorption and diffusion in flexible nanoporous materials. *Mol. Simul.* **2016**, *42*, 81-101.

72.Martínez, L.; Andrade, R.; Birgin, E. G.; Martínez, J. M., PACKMOL: A package for building initial configurations for molecular dynamics simulations. *Journal of Computational Chemistry* **2009**, *30*, 2157-2164.

73.Rowley, L. A.; Nicholson, D.; Parsonage, N. G., Monte Carlo grand canonical ensemble calculation in a gas-liquid transition region for 12-6 Argon. *Journal of Computational Physics* **1975**, *17*, 401-414.

74.Düren, T.; Millange, F.; Férey, G.; Walton, K. S.; Snurr, R. Q., Calculating Geometric Surface Areas as a Characterization Tool for Metal−Organic Frameworks. *The Journal of Physical Chemistry C* **2007**, *111*, 15350-15356.

75.Brunauer, S.; Emmett, P. H.; Teller, E., Adsorption of Gases in Multimolecular Layers. *Journal of the American Chemical Society* **1938**, *60*, 309-319.

76.Potoff, J. J.; Siepmann, J. I., Vapor–liquid equilibria of mixtures containing alkanes, carbon dioxide, and nitrogen. *AIChE Journal* **2001**, *47*, 1676-1682.

77.Limas, N. G.; Manz, T. A., Introducing DDEC6 Atomic Population Analysis: Part 4. Efficient Parallel Computation of Net Atomic Charges, Atomic Spin Moments, Bond Orders, and More. *RSC Adv.* **2018**, *8*, 2678-2707.

78.Manz, T. A., Introducing DDEC6 atomic population analysis: part 3. Comprehensive method to compute bond orders. *RSC Advances* **2017**, *7*, 45552-45581.

79.Limas, N. G.; Manz, T. A., Introducing DDEC6 atomic population analysis: part 2. Computed results for a wide range of periodic and nonperiodic materials. *RSC Advances* **2016**, *6*, 45727-45747.

80.Manz, T. A.; Limas, N. G., Introducing DDEC6 atomic population analysis: part 1. Charge partitioning theory and methodology. *RSC Advances* **2016**, *6*, 47771-47801.

81.Mayo, S. L.; Olafson, B. D.; Goddard, W. A., DREIDING: a generic force field for molecular simulations. *The Journal of Physical Chemistry* **1990**, *94*, 8897-8909.

82.Rappe, A. K.; Casewit, C. J.; Colwell, K. S.; Goddard, W. A.; Skiff, W. M., UFF, a Full Periodic Table Force Field for Molecular Mechanics and Molecular Dynamics Simulations. *J. Am. Chem. Soc.* **1992**, *114*, 10024-10035.

83.Ye, J.; Johnson, J. K., Catalytic hydrogenation of CO2 to methanol in a Lewis pair functionalized MOF. *Catalysis Science & Technology* **2016**, *6*, 8392-8405.

84.Allen, M. P.; Tildesley, D. J., *Computer Simulation of Liquids*; Oxford University Press, 2017.

85.Stukowski, A., Visualization and analysis of atomistic simulation data with OVITO–the Open Visualization Tool. *Modelling and Simulation in Materials Science and Engineering* **2009**, *18*, 015012.

86.Furukawa, H.; Cordova, K. E.; O'Keeffe, M.; Yaghi, O. M., The Chemistry and Applications of Metal-Organic Frameworks. *Science* **2013**, *341*, 1230444-1230444.

87.Zhou, H.-C.; Long, J. R.; Yaghi, O. M., Introduction to Metal–Organic Frameworks. *Chemical Reviews* **2012**, *112*, 673-674.

88.Ahmad, M. Z.; Peters, T. A.; Konnertz, N. M.; Visser, T.; Téllez, C.; Coronas, J.; Fila, V.; de Vos, W. M.; Benes, N. E., High-Pressure CO_2/CH_4 Separation of Zr-MOFs Based Mixed Matrix Membranes. *Separation and Purification Technology* **2020**, *230*.

89.Bae, T.-H.; Lee, J. S.; Qiu, W.; Koros, W. J.; Jones, C. W.; Nair, S., A High-Performance Gas-Separation Membrane Containing Submicrometer-Sized Metal-Organic Framework Crystals. *Angewandte Chemie International Edition* **2010**, *49*, 9863-9866.

90.Mohamed, M. H.; Yang, Y.; Li, L.; Zhang, S.; Ruffley, J. P.; Jarvi, A. G.; Saxena, S.; Veser, G.; Johnson, J. K.; Rosi, N. L., Designing Open Metal Sites in Metal–Organic Frameworks for Paraffin/Olefin Separations. *J. Am. Chem. Soc.* **2019**, *141*, 13003-13007.

91.Xie, Z.; Li, T.; Rosi, N. L.; Carreon, M. A., Alumina-Supported Cobalt–Adeninate MOF Membranes for CO_2/CH_4 Separation. *J. Mater. Chem. A* **2014**, *2*, 1239-1241.

92.Nemati Vesali Azar, A.; Keskin, S., Computational Screening of MOFs for Acetylene Separation. *Frontiers in Chemistry* **2018**, *6*.

93.Li, L.; Zhang, S.; Ruffley, J. P.; Johnson, J. K., Energy Efficient Formaldehyde Synthesis by Direct Hydrogenation of Carbon Monoxide in Functionalized Metal–Organic Frameworks. *ACS Sustainable Chemistry & Engineering* **2018**, *7*, 2508-2515.

94.Han, S.; Huang, Y.; Watanabe, T.; Nair, S.; Walton, K. S.; Sholl, D. S.; Carson Meredith, J., MOF Stability and Gas Adsorption as a Function of Exposure to Water, Humid Air, SO_2, and NO_2. *Microporous and Mesoporous Materials* **2013**, *173*, 86-91.

95.Grant Glover, T.; Peterson, G. W.; Schindler, B. J.; Britt, D.; Yaghi, O., MOF-74 Building Unit has a Direct Impact on Toxic Gas Adsorption. *Chemical Engineering Science* **2011**, *66*, 163-170.

96.Kirlikovali, K. O.; Chen, Z.; Islamoglu, T.; Hupp, J. T.; Farha, O. K., Zirconium-Based Metal–Organic Frameworks for the Catalytic Hydrolysis of Organophosphorus Nerve Agents. *ACS Appl. Mater. Interfaces* **2020**, *12*, 14702-14720.

97.Liu, Y.; Howarth, A. J.; Vermeulen, N. A.; Moon, S.-Y.; Hupp, J. T.; Farha, O. K., Catalytic Degradation of Chemical Warfare Agents and Their Simulants by Metal-Organic Frameworks. *Coord. Chem. Rev.* **2017**, *346*, 101-111.

98.Mondloch, J. E.; Katz, M. J.; Isley Iii, W. C.; Ghosh, P.; Liao, P.; Bury, W.; Wagner, G. W.; Hall, M. G.; DeCoste, J. B.; Peterson, G. W., et al., Destruction of Chemical Warfare Agents Using Metal–Organic Frameworks. *Nat. Mater.* **2015**, *14*, 512-516.

99.Islamoglu, T.; Chen, Z.; Wasson, M. C.; Buru, C. T.; Kirlikovali, K. O.; Afrin, U.; Mian, M. R.; Farha, O. K., Metal–Organic Frameworks Against Toxic Chemicals. *Chemical Reviews* **2020**.

100.Son, F. A.; Wasson, M. C.; Islamoglu, T.; Chen, Z.; Gong, X.; Hanna, S. L.; Lyu, J.; Wang, X.; Idrees, K. B.; Mahle, J. J., et al., Uncovering the Role of Metal–Organic Framework Topology on the Capture and Reactivity of Chemical Warfare Agents. *Chemistry of Materials* **2020**, *32*, 4609-4617.

101.Shearer, G. C.; Forselv, S.; Chavan, S.; Bordiga, S.; Mathisen, K.; Bjørgen, M.; Svelle, S.; Lillerud, K. P., In Situ Infrared Spectroscopic and Gravimetric Characterisation of the Solvent Removal and Dehydroxylation of the Metal Organic Frameworks UiO-66 and UiO-67. *Topics in Catalysis* **2013**, *56*, 770-782.

102.Agrawal, M.; Boulfelfel, S. E.; Sava Gallis, D. F.; Greathouse, J. A.; Sholl, D. S., Determining Diffusion Coefficients of Chemical Warfare Agents in Metal–Organic Frameworks. *The Journal of Physical Chemistry Letters* **2019**, *10*, 7823-7830.

103.Ramsahye, N. A.; Maurin, G., Modeling of Diffusion in MOFs. In *Modelling and Simulation in the Science of Micro- and Meso-Porous Materials*, 2018; pp 63-97.

104.Skoulidas, A. I., Molecular Dynamics Simulations of Gas Diffusion in Metal−Organic Frameworks: Argon in CuBTC. *Journal of the American Chemical Society* **2004**, *126*, 1356-1357.

105.Parkes, M. V.; Demir, H.; Teich-McGoldrick, S. L.; Sholl, D. S.; Greathouse, J. A.; Allendorf, M. D., Molecular Dynamics Simulation of Framework Flexibility Effects on Noble Gas Diffusion in HKUST-1 and ZIF-8. *Microporous and Mesoporous Materials* **2014**, *194*, 190-199.

106.Liu, B.; Yang, Q.; Xue, C.; Zhong, C.; Smit, B., Molecular Simulation of Hydrogen Diffusion in Interpenetrated Metal–Organic Frameworks. *Physical Chemistry Chemical Physics* **2008**, *10*.

107.Liu, B.; Sun, C.; Chen, G., Molecular Simulation Studies of Separation of CH_4/H_2 Mixture in Metal-Organic Frameworks with Interpenetration and Mixed-Ligand. *Chem. Eng. Sci.* **2011**, *66*, 3012-3019.

108.Keskin, S., Gas Adsorption and Diffusion in a Highly CO_2 Selective Metal–Organic Framework: Molecular Simulations. *Molecular Simulation* **2013**, *39*, 14-24.

109.Farzi, N.; Salehi, N.; Mahboubi, A., Molecular Dynamics Simulation of Acetylene Diffusion in MOF-508a and MOF-508b. *Microporous Mesoporous Mater.* **2017**, *248*, 246-255.

110.Cabrales-Navarro, F. A.; Gómez-Ballesteros, J. L.; Balbuena, P. B., Molecular Dynamics Simulations of Metal-Organic Frameworks as Membranes for Gas Mixtures Separation. *J. Membr. Sci.* **2013**, *428*, 241-250.

111.Borah, B.; Zhang, H.; Snurr, R. Q., Diffusion of Methane and Other Alkanes in Metal-Organic Frameworks for Natural Gas Storage. *Chem. Eng. Sci.* **2015**, *124*, 135-143.

112.Bigdeli, A.; Khorasheh, F.; Tourani, S.; Khoshgard, A.; Bidaroni, H. H., Molecular Simulation Study of the Adsorption and Diffusion Properties of Terephthalic Acid in Various Metal Organic Frameworks. *Journal of Inorganic and Organometallic Polymers and Materials* **2019**, *30*, 1643-1652.

113.Yang , Q.; Jobic, H.; Salles, F.; Kolokolov , D.; Guillerm, V.; Serre, C.; Maurin, G., Probing the Dynamics of CO_2 and CH_4 within the Porous Zirconium Terephthalate UiO-66(Zr): A Synergic Combination of Neutron Scattering Measurements and Molecular Simulations. *Chem. Eur. J.* **2011**, *17*, 8882-8889.

114.Vargas L, E.; Snurr, R. Q., Heterogeneous Diffusion of Alkanes in the Hierarchical Metal–Organic Framework NU-1000. *Langmuir* **2015**, *31*, 10056-10065.

115.Skoulidas, A. I.; Sholl, D. S., Self-Diffusion and Transport Diffusion of Light Gases in Metal-Organic Framework Materials Assessed Using Molecular Dynamics Simulations. *J. Phys. Chem. B* **2005**, *109*, 15760-15768.

116.Amirjalayer, S.; Tafipolsky, M.; Schmid, R., Molecular Dynamics Simulation of Benzene Diffusion in MOF-5: Importance of Lattice Dynamics. *Angewandte Chemie International Edition* **2007**, *46*, 463-466.

117.Koizumi, K.; Nobusada, K.; Boero, M., Hydrogen Storage Mechanism and Diffusion in Metal–Organic Frameworks. *Phys. Chem. Chem. Phys.* **2019**, *21*, 7756-7764.

118.Liu, J.; Rankin, R. B.; Karl Johnson, J., The Importance of Charge–Quadrupole Interactions for H_2 Adsorption and Diffusion in CuBTC. *Molecular Simulation* **2009**, *35*, 60-69.

119.Liu, J.; Lee, J. Y.; Pan, L.; Obermyer, R. T.; Simizu, S.; Zande, B.; Li, J.; Sankar, S. G.; Johnson, J. K., Adsorption and Diffusion of Hydrogen in a New Metal−Organic Framework Material: [Zn(bdc)(ted)0.5]. *The Journal of Physical Chemistry C* **2008**, *112*, 2911-2917.

120.Skoulidas, A. I., Molecular Dynamics Simulations of Gas Diffusion in Metal−Organic Frameworks: Argon in CuBTC. *J. Am. Chem. Soc.* **2004**, *126*, 1356-1357.

121.Keskin, S.; Liu, J.; Johnson, J. K.; Sholl, D. S., Atomically Detailed Models of Gas Mixture Diffusion Through CuBTC Membranes. *Microporous and Mesoporous Materials* **2009**, *125*, 101-106.

122.Keskin, S.; Liu, J.; Johnson, J. K.; Sholl, D. S., Testing the Accuracy of Correlations for Multicomponent Mass Transport of Adsorbed Gases in Metal−Organic Frameworks: Diffusion of H_2/CH_4 Mixtures in CuBTC. *Langmuir* **2008**, *24*, 8254-8261.

123.Skoulidas, A. I.; Sholl, D. S., Molecular Dynamics Simulations of Self-Diffusivities, Corrected Diffusivities, and Transport Diffusivities of Light Gases in Four Silica Zeolites To Assess Influences of Pore Shape and Connectivity. *The Journal of Physical Chemistry A* **2003**, *107*, 10132-10141.

124.Grissom, T. G.; Sharp, C. H.; Usov, P. M.; Troya, D.; Morris, A. J.; Morris, J. R., Benzene, Toluene, and Xylene Transport through UiO-66: Diffusion Rates, Energetics, and the Role of Hydrogen Bonding. *The Journal of Physical Chemistry C* **2018**, *122*, 16060-16069.

125.Sharp, C. H.; Abelard, J.; Plonka, A. M.; Guo, W.; Hill, C. L.; Morris, J. R., Alkane–OH Hydrogen Bond Formation and Diffusion Energetics of n-Butane within UiO-66. *The Journal of Physical Chemistry C* **2017**, *121*, 8902-8906.

126.Boyd, P. G.; Moosavi, S. M.; Witman, M.; Smit, B., Force-Field Prediction of Materials Properties in Metal-Organic Frameworks. *J. Phys. Chem. Lett.* **2017**, *8*, 357-363.

127.Rogge, S. M. J.; Wieme, J.; Vanduyfhuys, L.; Vandenbrande, S.; Maurin, G.; Verstraelen, T.; Waroquier, M.; Van Speybroeck, V., Thermodynamic Insight in the High-Pressure Behavior of UiO-66: Effect of Linker Defects and Linker Expansion. *Chem. Mater.* **2016**, *28*, 5721-5732.

128.Manz, T. A., Introducing DDEC6 Atomic Population Analysis: Part 3. Comprehensive Method to Compute Bond Orders. *RSC Adv.* **2017**, *7*, 45552-45581.

129.Stubbs, J. M.; Potoff, J. J.; Siepmann, J. I., Transferable Potentials for Phase Equilibria. 6. United-Atom Description for Ethers, Glycols, Ketones, and Aldehydes. *The Journal of Physical Chemistry B* **2004**, *108*, 17596-17605.

130.Morales, J. J.; Nuevo, M. J., Path Integral Molecular Dynamics Methods: Application to Neon. *Journal of Computational Chemistry* **1995**, *16*, 105-112.

131.Nosé, S., A Unified Formulation of the Constant Temperature Molecular Dynamics Methods. *The Journal of Chemical Physics* **1984**, *81*, 511-519.

132.Hoover, W. G., Canonical Dynamics: Equilibrium Phase-Space Distributions. *Physical Review A* **1985**, *31*, 1695-1697.

133.Agrawal, M.; Sava Gallis, D. F.; Greathouse, J. A.; Sholl, D. S., How Useful Are Common Simulants of Chemical Warfare Agents at Predicting Adsorption Behavior? *The Journal of Physical Chemistry C* **2018**, *122*, 26061-26069.

134.Weber, V.; VandeVondele, J.; Hutter, J.; Niklasson, A. M. N., Direct Energy Functional Minimization Under Orthogonality Constraints. *The Journal of Chemical Physics* **2008**, *128*.

135.Breck, D. W., *Zeolite Molecular Sieves: Structure, Chemistry, and Use*; Wiley: New York,, 1973, p ix, 771 p.

136.Ramsahye, N. A.; Gao, J.; Jobic, H.; Llewellyn, P. L.; Yang, Q.; Wiersum, A. D.; Koza, M. M.; Guillerm, V.; Serre, C.; Zhong, C. L., et al., Adsorption and Diffusion of Light Hydrocarbons in UiO-66(Zr): A Combination of Experimental and Modeling Tools. *The Journal of Physical Chemistry C* **2014**, *118*, 27470-27482.

137.Chen, B.; Potoff, J. J.; Siepmann, J. I., Monte Carlo Calculations for Alcohols and Their Mixtures with Alkanes. Transferable Potentials for Phase Equilibria. 5. United-Atom Description of Primary, Secondary, and Tertiary Alcohols. *The Journal of Physical Chemistry B* **2001**, *105*, 3093-3104.

138.Scott Cairns, A. S., Maurizio Barbeschi *United Nations mission to investigate allegations of the use of chemical weapons in the Syrian Arab Republic: Report on the alleged use of chemical weapons in the Ghouta Area of Damascus on 21 August 2013*; United Nations: 2013; p 41.

139.Justin McCurry, E. G.-H., Kim Jong-un's half-brother dies after 'attack' at airport in Malaysia. *The Guardian* February 14, 2017.

140.Vikram Dodd, L. H., Ewen MacAskill, Sergei Skripal: former Russian spy poisoned with nerve agent, say police. *The Guardian* March 8, 2018.

141.Steinbuch, Y., French, Swedish labs confirm Alexei Navalny poisoned with Novichok: Germany. *New York Post* September 14, 2020.

142.Liu, Y.; Buru, C. T.; Howarth, A. J.; Mahle, J. J.; Buchanan, J. H.; DeCoste, J. B.; Hupp, J. T.; Farha, O. K., Efficient and Selective Oxidation of Sulfur Mustard Using Singlet Oxygen Generated by a Pyrene-based Metal–Organic Framework. *J. Mater. Chem. A* **2016**, *4*, 13809-13813.

143.Wang, H.; Wagner, G. W.; Lu, A. X.; Nguyen, D. L.; Buchanan, J. H.; McNutt, P. M.; Karwacki, C. J., Photocatalytic Oxidation of Sulfur Mustard and its Simulant on BODIPY-Incorporated Polymer Coatings and Fabrics. *ACS Applied Materials & Interfaces* **2018**, *10*, 18771-18777.

144.Doris, E.; Oheix, E.; Gravel, E., Catalytic processes for the neutralization of sulfur mustard. *Chemistry – A European Journal* **2020**.

145.Howarth, A. J.; Majewski, M. B.; Farha, O. K., Metal-Organic Frameworks for Capture and Detoxification of Nerve Agents. In *Metal-Organic Frameworks (MOFs) for Environmental Applications*, 2019; pp 179-202.

146.Cha, G.-Y.; Chun, H.; Hong, D.-Y.; Kim, J.; Cho, K.-H.; Lee, U. H.; Chang, J.-S.; Ryu, S. G.; Lee, H. W.; Kim, S.-J., et al., Unique Design of Superior Metal-Organic Framework for Removal of Toxic Chemicals in Humid Environment Via Direct Functionalization of the Metal Nodes. *Journal of Hazardous Materials* **2020**, *398*.

147.DeCoste, J. B.; Peterson, G. W., Metal–Organic Frameworks for Air Purification of Toxic Chemicals. *Chemical Reviews* **2014**, *114*, 5695-5727.

148.Li, J.; Wang, X.; Zhao, G.; Chen, C.; Chai, Z.; Alsaedi, A.; Hayat, T.; Wang, X., Metal–Organic Framework-Based Materials: Superior Adsorbents for the Capture of Toxic and Radioactive Metal Ions. *Chemical Society Reviews* **2018**, *47*, 2322-2356.

149.DeCoste, J. B.; Demasky, T. J.; Katz, M. J.; Farha, O. K.; Hupp, J. T., A UiO-66 Analogue with Uncoordinated Carboxylic Acids for the Broad-Spectrum Removal of Toxic Chemicals. *New Journal of Chemistry* **2015**, *39*, 2396-2399.

150.Barea, E.; Montoro, C.; Navarro, J. A. R., Toxic Gas Removal – Metal–Organic Frameworks for the Capture and Degradation of Toxic Gases and Vapours. *Chem. Soc. Rev.* **2014**, *43*, 5419-5430.

151.Wang, H.; Lustig, W. P.; Li, J., Sensing and Capture of Toxic and Hazardous Gases and Vapors by Metal–Organic Frameworks. *Chemical Society Reviews* **2018**, *47*, 4729-4756.

152.Asha, P.; Sinha, M.; Mandal, S., Effective Removal of Chemical Warfare Agent Simulants Using Water Stable Metal–Organic Frameworks: Mechanistic Study and Structure–Property Correlation. *RSC Advances* **2017**, *7*, 6691-6696.

153.Ayoub, G.; Arhangelskis, M.; Zhang, X.; Son, F.; Islamoglu, T.; Friščić, T.; Farha, O. K., Air Oxidation of Sulfur Mustard Gas Simulants Using a Pyrene-Based Metal–Organic Framework Photocatalyst. *Beilstein Journal of Nanotechnology* **2019**, *10*, 2422-2427.

154.Grissom, T. G.; Plonka, A. M.; Sharp, C. H.; Ebrahim, A. M.; Tian, Y.; Collins-Wildman, D. L.; Kaledin, A. L.; Siegal, H. J.; Troya, D.; Hill, C. L., et al., Metal–Organic Framework- and Polyoxometalate-Based Sorbents for the Uptake and Destruction of Chemical Warfare Agents. *ACS Applied Materials & Interfaces* **2020**, *12*, 14641-14661.

155.Lee, D. T.; Jamir, J. D.; Peterson, G. W.; Parsons, G. N., Protective Fabrics: Metal-Organic Framework Textiles for Rapid Photocatalytic Sulfur Mustard Simulant Detoxification. *Matter* **2020**, *2*, 404-415.

156.Li, Y.; Gao, Q.; Zhou, Y.; Zhang, L.; Zhong, Y.; Ying, Y.; Zhang, M.; Liu, Y.; Wang, Y. a., Significant Enhancement in Hydrolytic Degradation of Sulfur Mustard Promoted by Silver Nanoparticles in the Ag NPs@HKUST-1 Composites. *Journal of Hazardous Materials* **2018**, *358*, 113-121.

157.Roy, A.; Srivastava, A. K.; Singh, B.; Mahato, T. H.; Shah, D.; Halve, A. K., Degradation of Sulfur Mustard and 2-Chloroethyl Ethyl Sulfide on Cu–BTC Metal Organic Framework. *Microporous Mesoporous Mater.* **2012**, *162*, 207-212.

158.Gall, R. D.; Hill, C. L.; Walker, J. E., Carbon Powder and Fiber-Supported Polyoxometalate Catalytic Materials. Preparation, Characterization, and Catalytic Oxidation of Dialkyl Sulfides as Mustard (HD) Analogues. *Chemistry of Materials* **1996**, *8*, 2523-2527.

159.Gall, R. D.; Hill, C. L.; Walker, J. E., Selective Oxidation of Thioether Mustard (HD) Analogs by tert-Butylhydroperoxide Catalyzed by $H_5PV_2Mo_{10}O_{40}$ Supported on Porous Carbon Materials. *Journal of Catalysis* **1996**, *159*, 473-478.

160.Bae, S. Y.; Winemiller, M. D., Mechanistic Insights into the Hydrolysis of 2-Chloroethyl Ethyl Sulfide: The Expanded Roles of Sulfonium Salts. *The Journal of Organic Chemistry* **2013**, *78*, 6457-6470.

161.Munro, N. B.; Talmage, S. S.; Griffin, G. D.; Waters, L. C.; Watson, A. P.; King, J. F.; Hauschild, V., The Sources, Fate, and Toxicity of Chemical Warfare Agent Degradation Products. *Environmental Health Perspectives* **1999**, *107*, 933-974.

162.Yang, Y. C.; Szafraniec, L. L.; Beaudry, W. T.; Ward, J. R., Kinetics and Mechanism of the Hydrolysis of 2-Chloroethyl Sulfides. *The Journal of Organic Chemistry* **1988**, *53*, 3293-3297.

163.Wagner, G. W.; Yang, Y.-C., Rapid Nucleophilic/Oxidative Decontamination of Chemical Warfare Agents. *Industrial & Engineering Chemistry Research* **2002**, *41*, 1925-1928.

164.Yang, Y. C.; Baker, J. A.; Ward, J. R., Decontamination of Chemical Warfare Agents. *Chemical Reviews* **1992**, *92*, 1729-1743.

165.Yang, Y. C.; Szafraniec, L. L.; Beaudry, W. T.; Davis, F. A., A Comparison of the Oxidative Reactivities of Mustard (2,2'-dichlorodiethyl sulfide) and Bivalent Sulfides. *The Journal of Organic Chemistry* **1990**, *55*, 3664-3666.

166.Nawała, J.; Jóźwik, P.; Popiel, S., Thermal and catalytic methods used for destruction of chemical warfare agents. *International Journal of Environmental Science and Technology* **2019**, *16*, 3899-3912.

167.Minh N. Vo, J. P. R., J. Karl Johnson, Impact of Defects on the Decompostion of Chemical Warfare Agent Simulants in Zr-based Metal Organic Frameworks. *AIChE Journal* **2021**.

168.Arunan, E.; Desiraju, G. R.; Klein, R. A.; Sadlej, J.; Scheiner, S.; Alkorta, I.; Clary, D. C.; Crabtree, R. H.; Dannenberg, J. J.; Hobza, P., et al., Definition of the hydrogen bond (IUPAC Recommendations 2011). *Pure Appl. Chem.* **2011**, *83*, 1637-1641.

169.Hanwell, M. D.; Curtis, D. E.; Lonie, D. C.; Vandermeersch, T.; Zurek, E.; Hutchison, G. R., Avogadro: an Advanced Semantic Chemical Editor, Visualization, and Analysis Platform. *Journal of Cheminformatics* **2012**, *4*.

170.Benschop, H. P.; De Jong, L. P. A., Nerve agent stereoisomers: analysis, isolation and toxicology. *Accounts of Chemical Research* **2002**, *21*, 368-374.

171.Kovarik, Z.; RadiĆ, Z.; Berman, H. A.; Simeon-Rudolf, V.; Reiner, E.; Taylor, P., Acetylcholinesterase active centre and gorge conformations analysed by combinatorial mutations and enantiomeric phosphonates. *Biochemical Journal* **2003**, *373*, 33-40.

172.DH, E., Handbook of chemical and biological warfare agents. CRC Press: Boca Raton, 2007; pp 37-42.

173.Hoenig, S., Compendium of chemical warfare agents. Springer: New York, 2007; p 86.

174.Mirzayanov, V., *State secrets: an insider's chronicle of the Russian chemical weapons program*; Outskirts Press, Inc: Denver, CO, 2009.

175.Bhakhoa, H.; Rhyman, L.; Ramasami, P., Theoretical study of the molecular aspect of the suspected novichok agent A234 of the Skripal poisoning. *Royal Society Open Science* **2019**, *6*.

176.Harvey, S. P.; McMahon, L. R.; Berg, F. J., Hydrolysis and enzymatic degradation of Novichok nerve agents. *Heliyon* **2020**, *6*.

177.M, P., Nerve agent attack used Novichok poison. *Chem. Eng. News.* **2018**, *96*, 3.

178.Liu, Y.; Moon, S.-Y.; Hupp, J. T.; Farha, O. K., Dual-Function Metal–Organic Framework as a Versatile Catalyst for Detoxifying Chemical Warfare Agent Simulants. *ACS Nano* **2015**, *9*, 12358-12364.

179.Plonka, A. M.; Wang, Q.; Gordon, W. O.; Balboa, A.; Troya, D.; Guo, W.; Sharp, C. H.; Senanayake, S. D.; Morris, J. R.; Hill, C. L., et al., In Situ Probes of Capture and Decomposition of Chemical Warfare Agent Simulants by Zr-Based Metal Organic Frameworks. *Journal of the American Chemical Society* **2017**, *139*, 599-602.

180.Moon, S.-Y.; Proussaloglou, E.; Peterson, G. W.; DeCoste, J. B.; Hall, M. G.; Howarth, A. J.; Hupp, J. T.; Farha, O. K., Detoxification of Chemical Warfare Agents Using a Zr6

-Based Metal-Organic Framework/Polymer Mixture. *Chemistry - A European Journal* **2016**, *22*, 14864-14868.

181.Song, L.; Zhao, T.; Yang, D.; Wang, X.; Hao, X.; Liu, Y.; Zhang, S.; Yu, Z.-Z., Photothermal graphene/UiO-66-NH_2 fabrics for ultrafast catalytic degradation of chemical warfare agent simulants. *Journal of Hazardous Materials* **2020**, *393*.

182.Tucker, J. B., *War of nerves : chemical warfare from World War I to al-Qaeda*, 1st ed.; Pantheon Books: New York, 2006, p xi, 479 p.

183.Benschop, H. P.; Konings, C. A. G.; Van Genderen, J.; De Jong, L. P. A., Isolation, anticholinesterase properties, and acute toxicity in mice of the four stereoisomers of the nerve agent soman. *Toxicology and Applied Pharmacology* **1984**, *72*, 61-74.

184.Soares, C. V.; Leitão, A. A.; Maurin, G., Computational evaluation of the chemical warfare agents capture performances of robust MOFs. *Microporous and Mesoporous Materials* **2019**, *280*, 97-104.

185.Peterson, G. W.; Destefano, M. R.; Garibay, S. J.; Ploskonka, A.; McEntee, M.; Hall, M.; Karwacki, C. J.; Hupp, J. T.; Farha, O. K., Optimizing Toxic Chemical Removal through Defect-Induced UiO-66-NH_2 Metal-Organic Framework. *Chemistry - A European Journal* **2017**, *23*, 15913-15916.

186.Gutov, O. V.; Hevia, M. G.; Escudero-Adán, E. C.; Shafir, A., Metal–Organic Framework (MOF) Defects under Control: Insights into the Missing Linker Sites and Their Implication in the Reactivity of Zirconium-Based Frameworks. *Inorganic Chemistry* **2015**, *54*, 8396-8400.

187.Liu, Y.; Klet, R. C.; Hupp, J. T.; Farha, O., Probing the correlations between the defects in metal–organic frameworks and their catalytic activity by an epoxide ring-opening reaction. *Chemical Communications* **2016**, *52*, 7806-7809.

188.Stukowski, A., Visualization and analysis of atomistic simulation data with OVITO–the Open Visualization Tool. *Modell. Simul. Mater. Sci. Eng.* **2010**, *18*.

189.Kresse, G.; Furthmüller, J., Efficient iterative schemes for ab initio total-energy calculations using a plane-wave basis set. *Physical Review B* **1996**, *54*, 11169-11186.

190.Kresse, G.; Furthmüller, J., Efficiency of ab-initio total energy calculations for metals and semiconductors using a plane-wave basis set. *Computational Materials Science* **1996**, *6*, 15-50.

191.Kresse, G.; Hafner, J., Ab initio molecular-dynamics simulation of the liquid-metal--amorphous-semiconductor transition in germanium. *Physical Review B* **1994**, *49*, 14251-14269.

192.Kresse, G.; Hafner, J., Ab initio molecular dynamics for liquid metals. *Physical Review B* **1993**, *47*, 558-561.